DELFT UNIVERSITY OF TECHNOLOGY

MASTER THESIS PROJECT

Local Buckling Analysis of Thin-Wall Shell Structures

Version 4.0(Final)

Supervisors:
Prof.Dr.Ir. J.G. Rots, Faculty CEG
Dr.Ir. P.C.J. Hoogenboom, Faculty CEG
Dr.Ir. F.P. van der Meer, Faculty CEG
Ir. A.Borgart, Faculty Architecture

Author:
FAN YE

October 2, 2015

Contents

Summary

This master thesis presents research into buckling of thin hyperboloid shells structures. This type of structure is typically applied as the large cooling towers at coal fired electricity plants. However, modelling cooling towers is not the objective of this research. The objective of this research is to understand the buckling behaviour of shells with negative Gaussian curvature, which cooling towers have. In previous research it was found that negatively curved shells are not very sensitive to imperfections and that the first buckling mode provides the most critical imperfection. This research starts from the assumption that a design formula can be derived for predicting the ultimate load of negatively curved shells. A step in this direction is understanding how hyperboloid shells buckle and determining what parameters influence the ultimate load.

A finite element model was developed with suitable properties. The influence of the boundary conditions has been studied. The element size and the aspect ratio have been optimised. Various methods of adding imperfections have been considered. The buckling modes have been studied for a large range of curvatures. The influence of the imperfection amplitude on the load displacement curve has been determined by geometrical nonlinear analysis and the arc length method.

A parameter study has been performed of a large range of geometries. Varied are the radii of curvature, the thickness, the height of the hyperboloid. Also varied are Youngs modulus and Poissons ratio. In total 700 geometrical nonlinear analysis have been performed. The results have been stored in a large data base in Matlab. This includes the support reactions, membrane forces, moments and stresses at each load

step.

A series of Matlab scripts were developed to generate various graphs. The graphs were used to form a detailed understanding of the buckling behaviour of negatively curved shells and to identify remarkable features. A two-phased curve fitting method has been used is to obtain a formula for the ultimate buckling load and a formula for the peak membrane force of inward buckles.

The main conclusion is that hyperboloid shells of significant curvature carry load in three ways: the outward buckles, the inward buckles and the material in-between. First the outward buckles fail then the inward buckles fail and finally the material between the buckles fails. A design method is proposed based on the local linear elastic stress state.

CHAPTER 1

Introduction

1.1 Study Background

Shell structures are widely used in engineer applications because of their free form shapes. Thin-wall shells are most practical, for they provide efficient ways to achieve large strength-weight ratios. Compared with other structural types, the critical situation of shell structures is not the material strength, shells often deform in buckling before yielding. Moreover, practical experience and experiments show that shell buckling is not a gradually process [3], it can happen suddenly. It may not provide sufficient deformation as a warning, which is the most serious shortcoming in shell applications, fig 1.1(a) shows the buckling of a cylinder shell in axial compression [14].

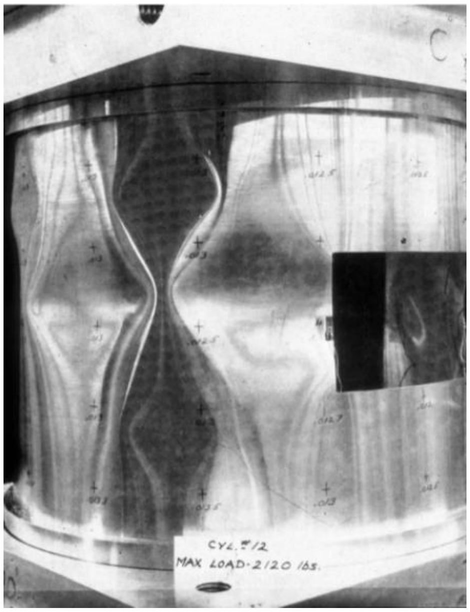

(a) Example of thin-wall shell buckling

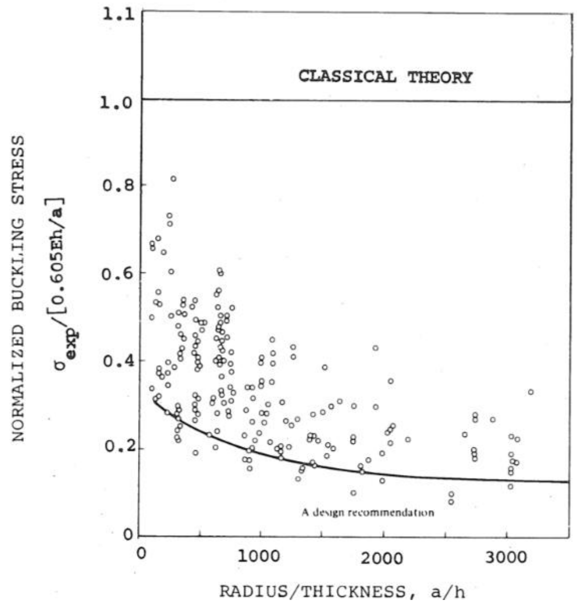

(b) Knock-down factor of cylinders with 1^{st} mode imperfections and varying imperfection

Figure 1.1: Experimental results of the thin-wall cylinder shells [3]

In analysis of thin-wall shell structures, the investigation shows that they are quite sensitive to tiny imperfections and experiments show that the buckling loads have a large standard deviation, in fig 1.1(b). As a result, the code provides a lower bound limitation for engineer application. Such an uniform and conservative limit value greatly restricts the development of thin-wall shells. The geometrical nonlinear buckling analysis in Finite Element Analysis (FEA) is also used in practice. However, nonlinear analysis is not only time consuming, but also sensitive to many analysis parameters.

It is known what exactly happens just before and during buckling and how this is affected by curvature and boundary conditions. An unsolved problem is whether shells buckle locally or globally.

1.2 Objective

The objective of this research is to understand the buckling behaviour of thin-wall shell structures, especially of hyperboloids including geometrical imperfections.

However, this research is restricted to elastic material behaviour, and the formula does not include material non-linearities such as yielding of steel or cracking of concrete. A geometric imperfection in the middle of the specimen is designed to avoid influence of the boundary conditions on the buckling behaviour.

1.3 Procedure

It is assumed that buckling starts locally in a small part of the shell. This part is described by curvatures, thickness, material properties, imperfection, membrane force and loading condition. The shell around this part is very important too. Therefore, the part is extended in all directions with uniform curvature and membrane force as much as possible.

A script has been developed in the FE program ANSYS for generating shells of different curvature and loading. The generated models include hyperboloids, cylinders and spheroids with geometrical imperfections, edge loading and surface loading. The script performs a geometrical nonlinear analysis up to buckling failure. This script has been used to do a parameter study on curvatures, imperfection amplitude and membrane forces.

To develop a suitable model, varying geometric conditions and different test conditions has been tested under geometric nonlinear analysis, which has been stored in a test result database. Analyse on the database has investigated the buckling load carrying system and design formulas on both global buckling reaction force and the internal membrane force in the ultimate buckling state.

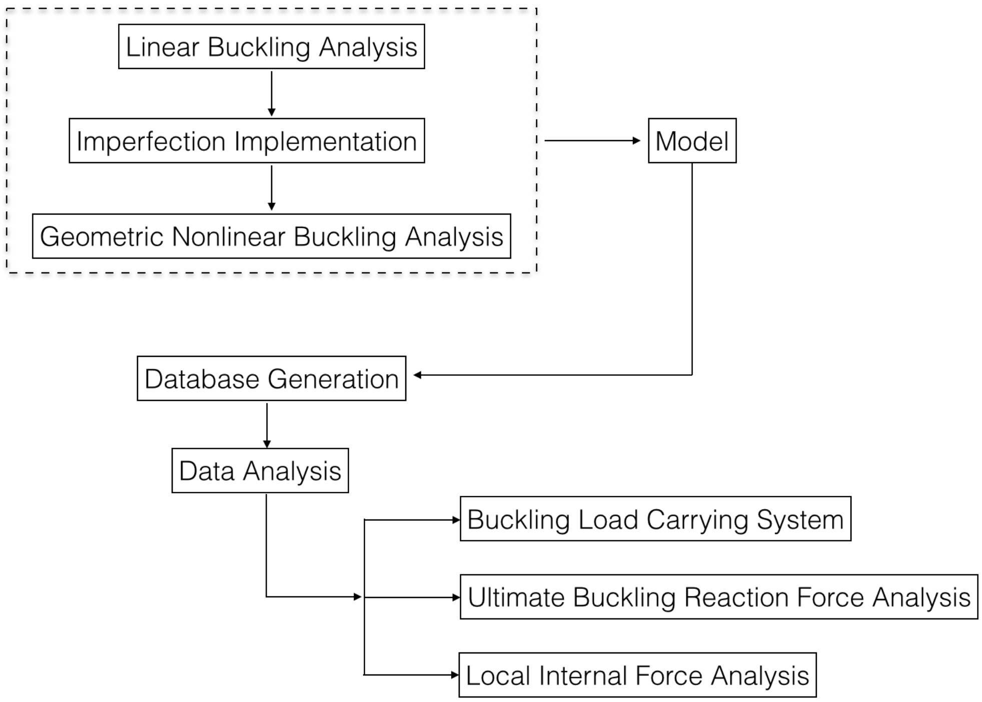

Figure 1.2: Work flow of the research procedure

1.3.1 Procedure Details

- **Step 1** Generate the FE model.

  The FE model is generated by the script with ANSYS Parametric Design Language (APDL). The global geometry and element shape are generated in parametric method, the sensitivity of which are investigated. The different geometries, cylinder, hyperboloid and spheroid are modelled.

- **Step 2** Apply the boundary condition

  The default boundary condition is the hinged constraint. Moreover, the varying restraints are tested, to observe the influence of the boundary condition.

- **Step 3** Linear analysis

  The linear elastic analysis is based on the perfect structure. Compared with the hand calculation, its result is used to check the load condition and the boundary condition.

- **Step 4** Linear buckling analysis

  The linear buckling analysis is to estimate the smallest buckling factor of the structure. Besides, the serious of the buckling shapes are obtained.

- **Step 5** Imperfection implementation

  The first linear buckling modal shape is implemented as the default imperfection, the imperfection shape by higher order modal shapes are tested as well.

- **Step 6** Geometric nonlinear buckling analysis

  In order to get the entire path of the buckling development, the Arc length method is applied. The radius of the load factor is based on the ratio of the first buckling load. In model generation, the GNBLA (Geometric Nonlinear Buckling Analysis) are designed to test the model robust of the different conditions, including the element size and shape, the boundary condition, the imperfection type, the model accuracy and the arc length method options. The results of these are utilized into the generation of the local buckling analysis database. In local buckling analysis, the model in different geometries are operated with GNBLA.

- **Step 8** Post-process analysis

  The preliminary post-process results as the F-D (Force-Displacement) curve and the element internal force behaviour are extracted by macro scripts directly. They are used to analysis the model behaviour, and the adjustments are made, depending on that.

- **Step 9** Database generation

  The geometric parameters are varied to investigate the their influence on the buckling. The specified GNLBA results are exported to a database in Matlab. Two types of results are recorded in database, they are proceeded in Matlab sparse matrix. The database includes results at the ultimate state and the selected results of every load step.

- **Step 10** Data analysis

  The relation between the local buckling force and the global buckling analysis is investigated. The buckling load carrying system has been discussed. Besides, by curve fitting method, the numerical simulation has been finished to estimate capacity of the internal force components. Different independent parameter combinations have been tested.

1.3.2 Thesis Description

In Chapter 2, the background knowledge and the related nonlinear analysis methods are described. The process of the FE model generation and the parametric study on model sensitivity are illustrated in Chapter 3. Based on the model discussion, the Chapter 4 generates a standard model at first, and finishes the GNLBA in 700 models. The database of the nonlinear analysis is created. With the numerical curve fitting, the data analysis is proceeded. Both of the buckling formula in global scope($F_u(\frac{R_m}{R_k}, t)$) and the local scope($n_{yy}(\frac{k_{xx}}{k_{yy}}, t)$) are simulated in numerically.

CHAPTER 2

Preceding Knowledge Study

2.1 Method of Buckling Analysis

The fig 2.1, shows different paths of the buckling behaviour.

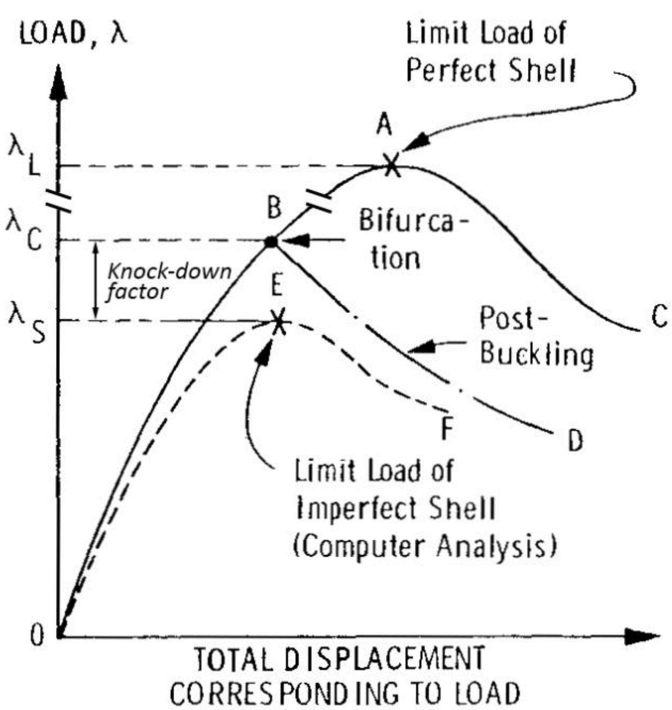

Figure 2.1: Different buckling path [3]

2.1.0.1 Linear Buckling Analysis

The linear buckling analysis on the perfect structure is the directest method. Before the buckling occurs, there is no deformation observed. The buckling happens suddenly and when the bifurcation point is reached, the deformation increases dramatically, path(BD). To estimate perfect shell buckling, the linear buckling analysis is the most efficient method.

The linear buckling analysis is a kind of eigenvalue analysis [11], based on the linear equation eq 2.1. The $\boldsymbol{K_G}$ is the geometric stiffness for a unit load. The critical linear load factor(λ) is solved, when it makes the structure stiffness matrix ($\boldsymbol{K}$) unstable.

$$(K - \lambda \cdot K_G) \cdot x = 0 \tag{2.1}$$

In reality imperfections are inevitable, and the actual load follows the path (OEF). The perfect model is always an upper boundary of the estimation. In practice, engineers are able to estimate a imperfect model capacity by the reduction factor. This approach is acceptable by AISC [5]. There are different ways to evaluate the buckling capacity. The numerical method to solve the estimated perfect capacity is called linear buckling analysis.

$$\lambda_a \leq C \cdot \frac{\lambda_{cr}}{\gamma_m} \tag{2.2}$$

where λ_a is the allowable applied load factor, the λ_{cr} is the critical linear buckling load factor, C is the empirical knockdown factor, γ_m is a safety partial factor.

2.1.1 Geometric Nonlinear Buckling Analysis

With imperfections, there is no bifurcation point, and the model behaviour is influenced by the initial imperfection, in path (OED). Different with the linear estimation, it is able to take the imperfection directly, the finite element method provides an approach to track the entire path of the F-D path. The geometric nonlinear calculation is operated to solve the equilibrium state at each step. There are several methods are optioned in the nonlinear analysis.

2.1.1.1 Newton-Raphson Method

In Newton-Raphson Method [11], the load is applied by linear increments. In each step, the stiffness matrix is calculated and the equilibrium state is determined with several iterations. One approach is called standard Newton-Raphson, the slope of the load increments changes on each load steps. Hence, the the stiffness matrix is calculated at every step and every iteration. The other approach, modified Newton-Rahpson, increases the load in fixed increment slope. It does not changes the stiffness matrix at every iteration and saves a lot of computational load, but the cost is more iteartion is needed. However, both approaches could only control the load with positive load increment. For buckling analysis, it is not able to track the unloading state.

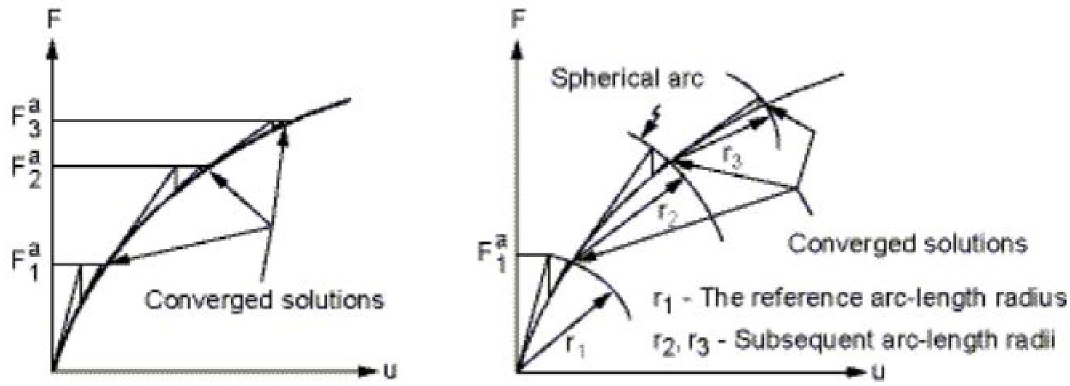

Figure 2.2: Comparison between the Newton-Raphson (left) and Arc length (right) [11]

2.1.1.2 Arc length Method

To follow the post-buckling path, the arc length method [11] is required. Different from the Newton-Raphon Method, the load control in arc length method is applied with load factor radius. The equilibrium state is searched along the specified radius, which is capable to achieve not only positive load increments but also negative load increments. Because there is not always one equilibrium path and the paths may be very close to each other, the most difficult in arc length is to set the range of the radius. The arc length radius as the key parameters has its maximum and minimum limitation. An extremely small arc length radius may cause the unrealized unloading path, and too large arc length radius may fail find out the equilibrium state.

2.1.1.3 Normal Flow Method

Different from the previous two method, the normal flow method [14] is a less well-known algorithm. A family of Davidenko curves is generated by the small variation δ to the nonlinear equation system, in eq 2.3.

$$f(\lambda, d) = \delta \tag{2.3}$$

For the one-dimension problem, the Davidenko curves are in dash line in fig 2.3. After the first tangential trial approaches the point B, the successive iterations return the convergent solution at point F along the path normal the Davidenko curves family.

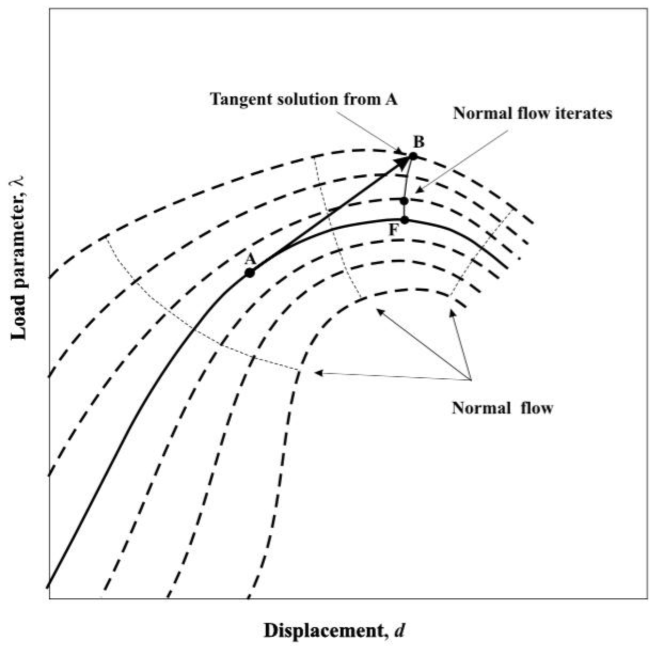

Figure 2.3: Normal flow algorithm for one-dimension problem [14]

2.1.2 Koiter Asymptotic Theory

Different with proceeding methods to achieve the ultimate load and the entire load path, the asymptotic theory focus the post-buckling behaviour. It describes the load behaviour in eq 2.4.

$$\frac{\lambda}{\lambda_c} = 1 + a_s \cdot \xi + b_s \cdot \xi^2 + \cdots \tag{2.4}$$

The Koiter theory [12] is an asymptotic method to describe the nearby behaviour with the intrinsic modal information and the imperfection through potential energy.

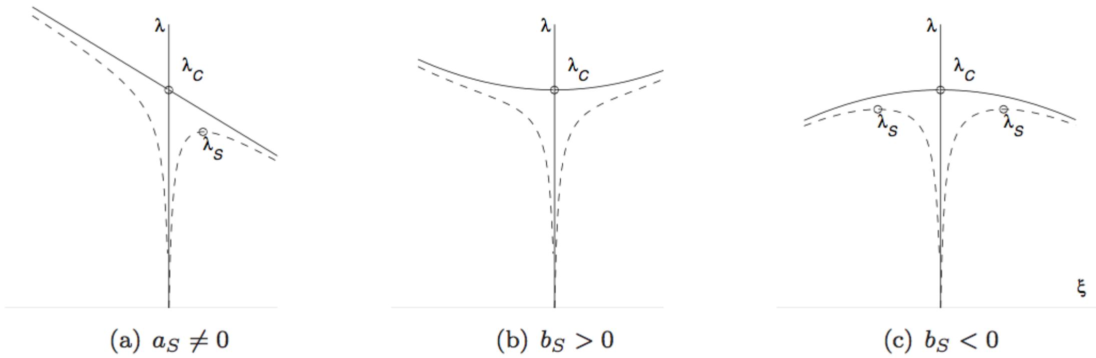

Figure 2.4: Koiter analysis: load-deflection curves [12]

Because engineers are only concerned about post-buckling is stable (fig 2.4.b) or unstable (fig 2.4.c), which is imperfection insensitivity or imperfection sensitivity. With the limit items ξ, it provides sufficient accuracy around the range of the buckling occurrence. However, the expression of the potential energy needs to be derives at first, it restrains the application of the theory within simple geometries.

2.2 Column Behaviour Assumption

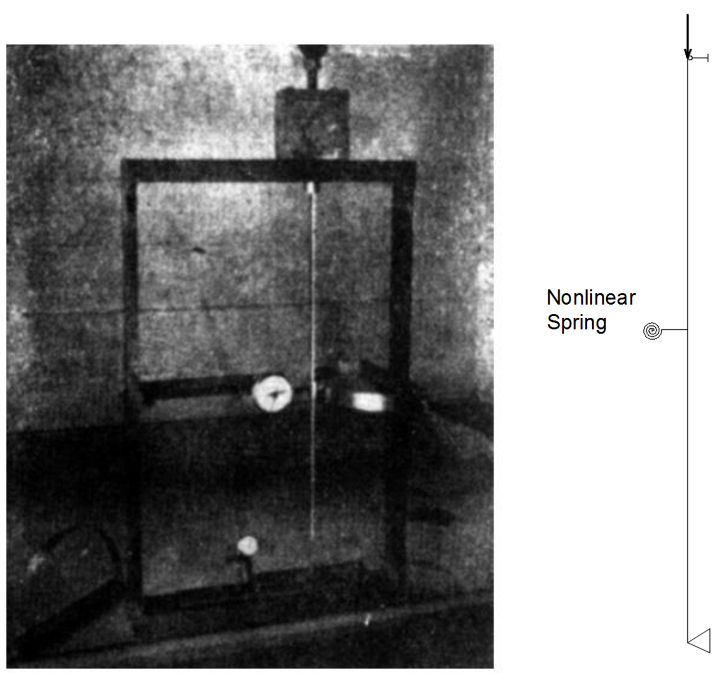

Figure 2.5: Test apparatus for columns supported by a semi circular ring support [16]

In 1940, Von Karman [16] has pointed out the inward buckle is the critical zone. He also proposed to simulate cylinder buckling as a longitudinal strip with the nonlinear elastic support. The radial deflection is restrained partially. The nonlinear elastic supported column buckling behaviour is an interesting assumption, and it supposes column-like behaviour in the local buckle as well.

2.3 Local Buckling Study

For local buckling analysis, the E.L.Axelrad [8] has tried to solve the behaviour of tube bending with the asymptotic theory. It was hypothesised that: the buckling instability is determined by the stress state and the shape of the shell inside the zone of the initial buckles. An analytical function to describe the shape of the local imperfection is generated. In this case, with the simplified assumption on the local site stress, the Talyor expansion is applied and the asymptotic result is solved analytically. Finally, the relation between the internal force and the geometric parameters are derived. This research was restrained to cylinders, and in the present study its approach to describe the ultimate stress state is applied in this thesis on negative double curvature as well.

2.4 Dimension Analysis

The dimension analysis is a method to find out the relation between the physical parameters. The basic idea is to obtain the relation in units, and extend it to the correspondent parameters, especially to those problem with a lot of parameters and the physical relation is unknown.

In recent years, R.K.Annabattula and P.R.Onck [1] apply this method into the study of the nano channel buckling effect. The dimension analysis combined with the derivation of the potential energy provides them a perfect geometric independent parameters to describe the buckling process. The series of test results are generalized into a general curves successfully.

In the shell buckling formula study, the same dilemma exists. The combination of the geometric independent parameters are under selected. The dimension analysis is applied. However, It is supposed to derive the correspondent potential energy to find out a more clear physical relation between the geometric parameters in the future research.

CHAPTER 3

Model Development

3.1 Model Generation

3.1.1 Finite Element Model

The perfect models are strictly defined by the mathematics expression, and three kinds of geometry are used, in eq 3.1, eq 3.2 and eq 3.3. To evaluate the curvature influence directly, the models have the same top and bottom radius value. The similar volume specimen makes the models comparable. Changing combinations of radius generate different curvatures in the middle area of the models, in which location the elements are focused on their buckling behaviours in results. The default thickness is defined as the 1/500 ratio to the height at first, and this ratio was investigated in the latter analysis. Considering the models are axisymmetric and horizontally symmetric as well, the half model has been used in the calculations, which save 3/4 of the computation load. The accuracy and symmetric boundary conditions of half structure model have been investigated.

$$\begin{cases} x^2 + z^2 = R_b^2 \\ 0 < y < h_t \end{cases} \tag{3.1}$$

$$\begin{cases} (\sqrt[2]{x^2 + z^2} - (R_b + a))^2 + (y + \frac{h_0}{2})^2 = R_b^2 \\ 0 < y < h_t \end{cases} \tag{3.2}$$

$$\begin{cases} (\sqrt[2]{x^2+z^2}-(R_b-a))^2+(y+\dfrac{h_0}{2})^2=R_b^2 \\ 0<y<h_t \end{cases} \tag{3.3}$$

,in which $a = \sqrt[2]{R_k^2 - \frac{h_0}{2}^2}$

3.1.2 Mesh Generation

3.1.2.1 Indirect Method

In the indirect method, the FE model is generated in two steps, the surface geometry and the FE model. For axis-symmetrical model, the Ansys has provided the command to rotate a planar curve into a surface geometry. The rotated curve is relied on the analytic formula of the curve, which is been divided into vertical segments. The rotation is also required to set the perimeter segments as well. It is obvious that the smaller segments are, the more the accurate surface geometry can be fitted. In the mesh procedure, the element size is decided, and the mesh is based on the lattice of the surface.

In indirect method, the numbers of the segments in the vertical direction and the perimeters are chosen, and the element size is also specified.

3.1.2.2 Direct Method

The direct method generates the FE model with the node coordination directly. The node information is calculated by the analytic formula before, the node distance in both directions are defined. According to the node sequence, the mesh is determined by linking the elements counter-clockwise, such sequence is defined by element property and has an influence on the normal vector direction of the surface. Shell Element 281 is applied. The mid-side nodes provide sufficient accuracy to fit the curvature of the geometry shape, especially for the double curvature geometry.

In the direct method, both of the distance in the vertical and the perimeters are specified.

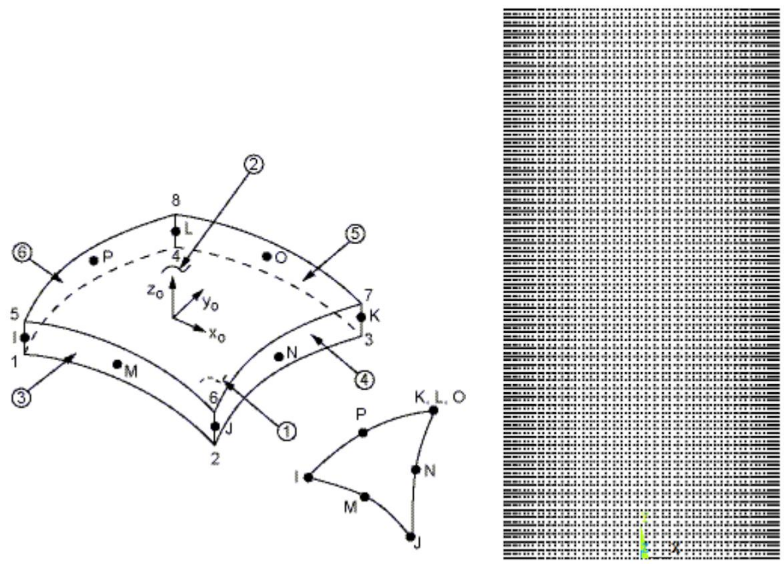

Figure 3.1: Shell element and the nodes of a cylindrical shell (ANSYS, Shell281 [15])

In this method, the geometric accuracy relies on the number of segments in both the height and the perimeter because the ANSYS simulates the curve in segments. The element size is tailored, and the square shape elements are possible, whose aspect ratios are exact by 1. In the direct method, the element size and shape are controlled by the distance of the nodes. There are only two parameters needed, the distance in height and the distance in perimeter, which are equivalent to the distance in height and the aspect ratio.

Compared with the indirect method, the direct method has one key parameter less, which gives an explicit control on element size and shape.

Moreover, the hinge restraints are applied to the model. Hence there are no displacement in the bottom ring and for the top ring the horizontal displacement in both direction are restrained. In order to reduce the edge influence, all the rotation displacement are released.

3.2 Buckling Analysis Process

3.2.1 Pre-processing

The pre-process generates the perfect FE model with the direct method, which has already been described in section 3.1.2.2.

3.2.2 Linear Buckling Analysis

Linear buckling analysis (LBA) is used to estimate the limit of the structural performance. In this research, three kinds of load are tested, uniformly distributed compression, imposed displacement and the surface pressure. If, for example, a unit load is applied, the eigenvalue solved by the LBA is the buckling load factor.

For LBA, the 'Block Lanczos Method '[11] is used, which can expand the linear buckling results in sequence. To improve the computation efficiency, the centre shift is set. The program computes the numbers of `BUC_CONT` buckling modes centred besides `BUC_CENT`. A coarse element size is used at first, and an estimated eigenvalue is treated as the centre of the next iteration with smaller size, as 60% element size. The iterations are terminated, when the reducing element size has no influence on the eigenvalue. Moreover, if the iteration step is too large (less than 50%) the eigenvalue cannot be solved successfully.

```
BUCOPT,LANB,BUC_CONT,BUC_CENT
```

3.2.3 Imperfection

Geometric imperfections are added to simulate the real behaviour buckling behaviour of the specimen, and to control the buckling performance. The imperfection is imported by one of two methods, depending on the type of imperfection.

Entire Model

ANSYS provides the command `UPGEOM` to update the entire structure from the specific load step. For the modal shape is expected to be imported, the `NUM_MOD` is defined to select the order of the modal shape, and `IMP_AMP` means the amplitude of the expected imperfection.

```
UPGEOM,IMP_AMP,1,NUM_MOD,LBA,rst
```

Part of Model

With the other type of imperfection, the imperfection import is based on the modification of FE model geometry. For the artificial imperfection, the imperfection on each node are calculated before, and the node modification command is used to modified the node coordination. Similarly, if the imperfection reduction factor and pre-tension method are applied, a modification loop is designed to modify the node or element information of the selected partial model.

3.2.4 Nonlinear Buckling

3.2.4.0.1 two termination options

The 'arc length method 'is used to overcome the buckling point of the structure. In nonlinear buckling analysis, an imposed boundary displacement is applied to the model. In ANSYS, there are two load-step methods. In common, the load is subdivided into several explicit load-step, and in each load step, there are several sub-step. While ANSYS [10] also support to use only one load step, and the sub-step size are controlled by the arc length method. Because we are interested in the ultimate load, the option in the arc length method that is to terminate when it reaches the first peak in order to reduce the computation load.

ARCTRM,L

The command also provides the option to continue the analysis over the post-buckling point. The displacement of a specified node is monitored, when it reaches some limited value after buckling has happened. For instance `Nodes_num` is the monitor with the horizontal direction-UY, and the analysis will be terminated if the displacement beyond `LBT` value.

ARCTRM,U,LBT,Nodes_num,UY

3.2.4.0.2 difference between arc length options

Both two termination conditions are tested, the first buckling modes and the varying imperfection amplitude. The curves are the load path with post-buckling parts, which are solved with the command `ARCTRM,U`, and the compared dots are the peak load of the other option `ARCTRM,L`, which is automatically terminated when the first limit is reached. For the lower imperfections, both methods achieve similar peak load on the vertex. However, with the great imperfections, there are no typical snap-back and the automatically terminated option stays at a lower ultimate state. The relation between these two methods are compared in table 3.1, the automatically terminated results is 12% lower than the other, if the imperfection is larger than $0.5t$.

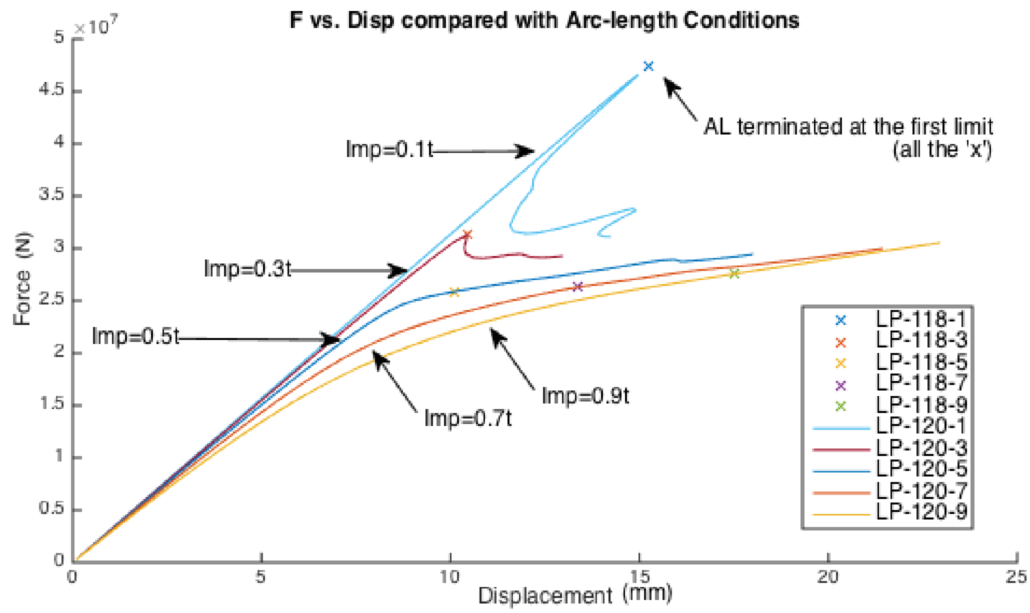

Figure 3.2: Force versus displacement for different Arc length termination options (LP-118/LP-120: Cylinder, R=2500mm, H=10000mm, t=10mm, E=210000MPa, ν=0.3, 1^{st}modal imperfection, δ_{imp}=0.1t-0.9t, different arc-length termination conditions)

Table 3.1: Relative difference between arc length options

δ_{amp}	$\frac{F_l - F_e}{F_e}$
0.1t	+1.88 %
0.3t	+0.01 %
0.5t	-12.27 %
0.7t	-12.24 %
0.9t	-9.64%

,where the F_l - GNLBA is terminated automatically when the first limit reaches F_e - GNLBA is terminated with the specified displacement, and the snap-back is overcome

3.2.5 Post-Processing

The post-process is designed to deal with the nonlinear buckling results, and several parameters are monitored, to describe the specimen behaviour in the test.

Force-Displacement The F-D curve is the most direct graph to show the process of specimen buckling. The vertical displacement of the node, that is loaded, is selected to be plotted versus the total reaction force. For perfect models, with the load development, the displacement increases in a linear part at first, when it reaches the bifurcation point, there are two paths that could happen. However, in this thesis, we induce the imperfection, there is no bifurcation point any more, and we are not interested in the post-buckling behaviour. The peak load at the snap-back is treated as the ultimate load.

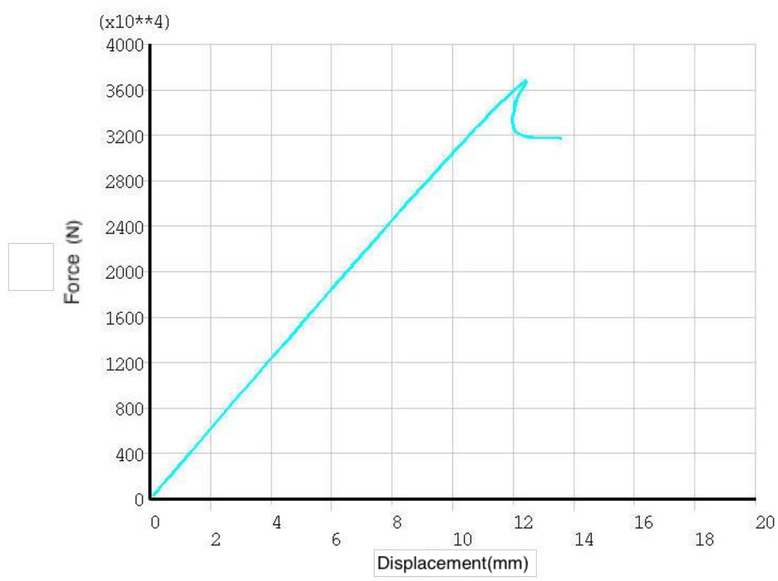

Figure 3.3: Example of a typical force-displacement curve (LP-120: Cylinder, R=2500mm, H=10000mm, t=10mm, E=210000MPa, ν=0.3, 1^{st}modal imperfection, δ_{imp}=0.2t)

Maximum Horizontal Deformation Position To control the most protuberance position of the specimen, the radial deformation of each load step is monitored, and the nodes with the maximum displacement are recorded. The relative height of these nodes is plotted with increasing load. The following graph is used to evaluate whether the specimen buckling dents are stable or not, for some uniform distribution imperfection dents, the protuberance sometimes does not stay in the middle, but they jump a lot; and for some concentrated imperfection, like hyperboloid, the protuberance are stable exactly at the $h_r = 0.5$, which is the equator, fig 3.5 .

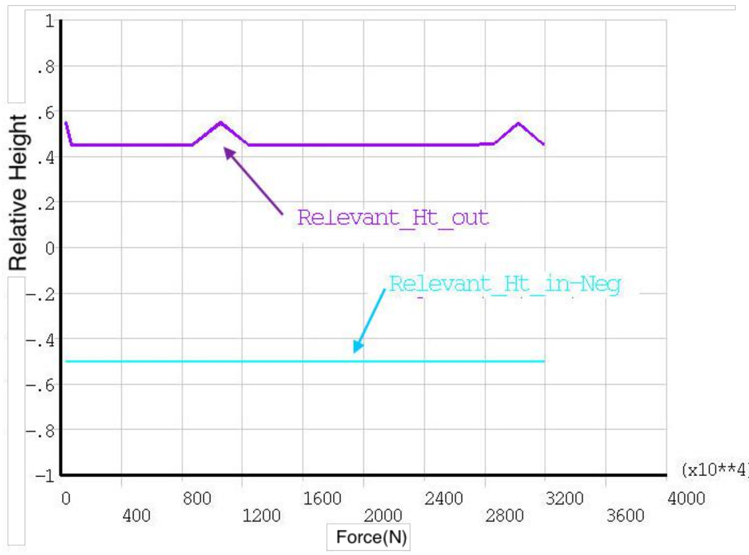

Figure 3.4: Example of a load - relative height of max radial deformation (inward & outward) (LP-120: Cylinder, R=2500mm, H=10000mm, t=10mm, E=210000MPa, ν=0.3, 1stmodal imperfection, δ_{imp}=0.2t)

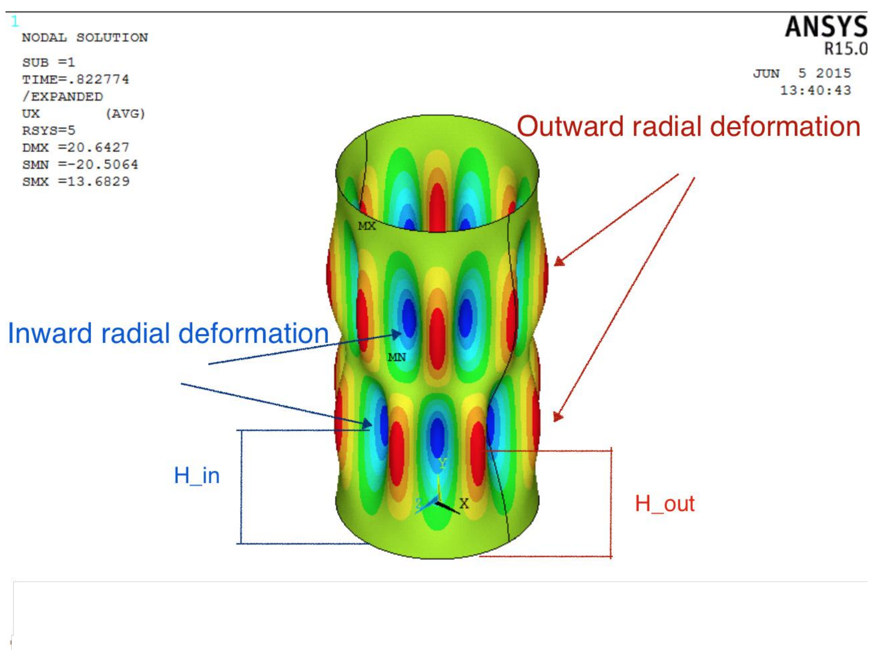

Figure 3.5: Indication for radial deformation and its relative height (LP-120: Cylinder, R=2500mm, H=10000mm, t=10mm, E=210000MPa, ν=0.3, 1stmodal imperfection, δ_{imp}=0.2t)

Force-Radial Deformation

At the buckling step, the maximum radial deformation is plotted with the load. It is designed to monitor the imperfection development. On the other hand, for some stiff specimen, whose F-D curve is hard to overcome the snap-back, the F-P curve is a good alternative to evaluate the structure behaviour.

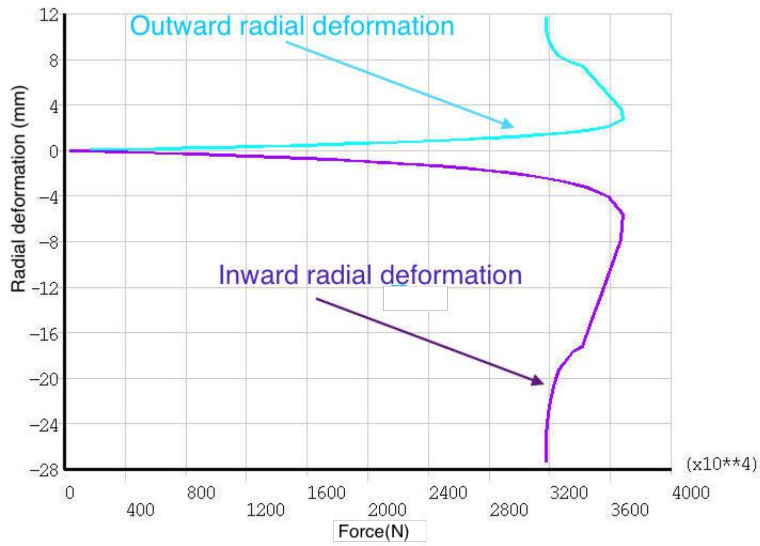

Figure 3.6: Example of a force-radial deformation curve (LP-120: Cylinder, R=2500mm, H=10000mm, t=10mm, E=210000MPa, ν=0.3, 1^{st}modal imperfection, δ_{imp}=0.2t)

Element Result

The element results of the buckling zone is a direct graph to show what happens in buckling. As the buckling theory describes, the buckling is the sudden energy transfer, from the membrane deformation to the bending deformation [2]. The membrane force increases linearly, until the buckling point, and the bending moment increases dramatically. However, it depends on the extent of the imperfection, the bending has already appeared in the specimen, and its relation with the amplitude is investigated.

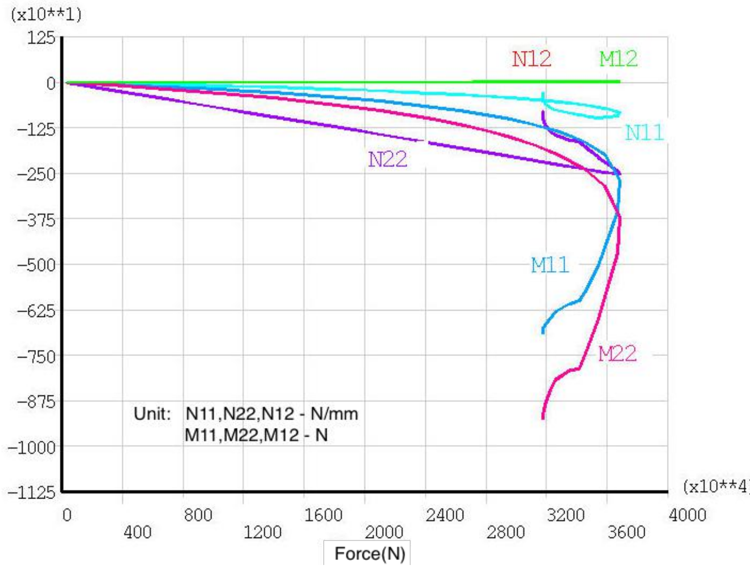

Figure 3.7: Example of element internal force result (LP-120: Cylinder, R=2500mm, H=10000mm, t=10mm, E=210000MPa, ν=0.3, 1^{st}modal imperfection, δ_{imp}=0.2t)

3.3 Boundary Conditions

3.3.1 Half Model Boundary

Regarding the axial-symmetrical specimen, it is observed that the analysis results are symmetry also. To reduce the computation load, the half model is supposed, and the boundary condition is followed with symmetrical deformation, in which one out-of-plane translational deformation and two in-plane rotation deformation are constrained, and the others three DOFs are released. For instance, the xoy is the symmetrical plane, UZ, RotX and RotY is constrained. In this subsection, the results between the entire model and the half model are compared.

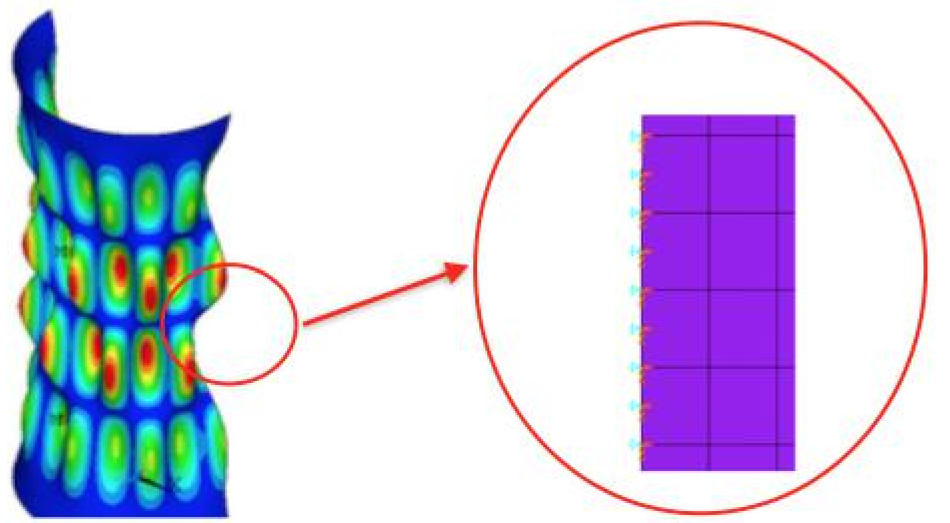

Figure 3.8: Symmetrical simplification boundary condition

The cylinder specimens are tested in both methods, and the first order of buckling modal shapes are used as imperfection with $\delta = 0.1t$. The following table shows the model information comparison. The GNLBA results are compared with the inward radial deformation.

Table 3.2: Comparison between the entire model and the half simplification

	Entire Model	**Half Model**	**difference %**
Node amount	109004	54807	49%
Fc	72076445 N	72076445 N	0%
Fu(GNLBA)	47466188 N	47471759 N	0.0117%
Calculation time(GNLBA)	102mins	41 mins	59.8 %

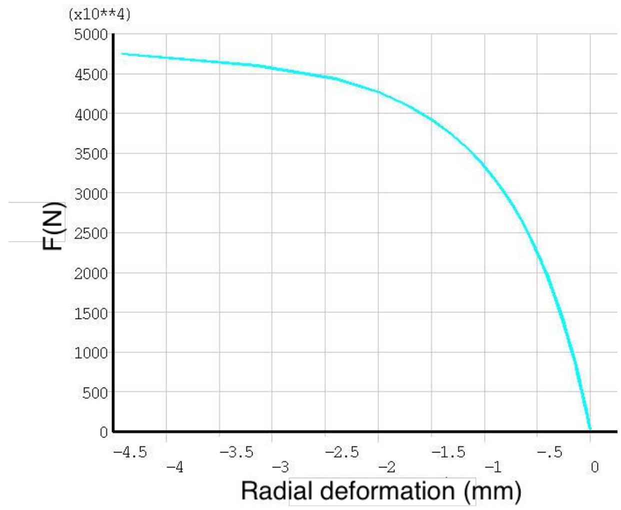

(a) Entire model

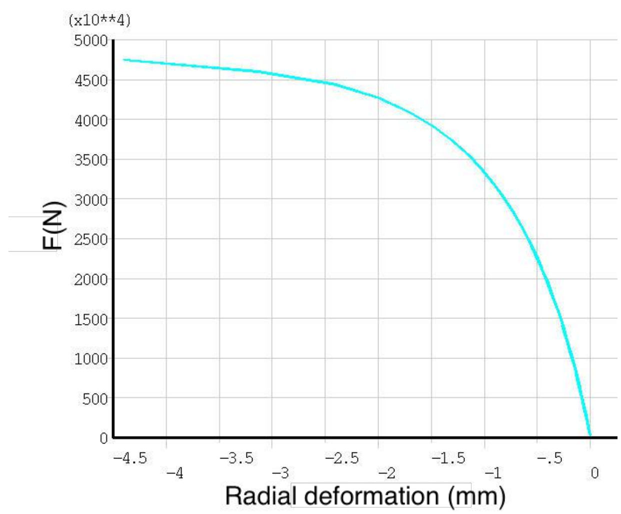

(b) Half model

Figure 3.9: Curve about F-inward radial deformation between the half model and entire model (LP-118/LP-210: Hyperboloid, Rd=2500mm, Rk=20000mm, H=10000mm, t=10mm, E=210000MPa, ν=0.3, 1^{st}modal imperfection, δ_{imp}=0.5t, entire model and half model)

It is evident that the half-model simplification has stimulated the identical behaviour with the entire model successfully, and it saves almost 60% computation load. Note that the half model simplification assumes the deformation are symmetric, including the linear buckling results, which means only the even numbers of the buckling wave will appear. The influence on the buckling wavelength should not be neglected, unless there are sufficient buckles in the horizontal direction. For the test models in this research, the number of the horizontal waves are beyond 16, whose accuracy are sufficient enough.

3.3.2 Boundary Conditions Variation

3.3.2.1 Experiment Introduction

According experiments carried out by Lundquist [13] and Donnell [6], axial-compressed cylinders are loaded with two thick steel plate. The thick steel plates are assumed stiff enough to transfer the uniform distribution load. All the test specimens are produced carefully, to avoid any small wrinkle, which makes them nearly perfect models.

They applied different methods to initiate buckling in the middle area. For Lundquist's experiments, to stiffen the ends of specimens, a light metal ring was soldered at each end of the cylinder. Because the sheet is wrapped about a mandrel and soldered at the seam and the weld against the plate of the loading machine is critical. From Donnell's, the ends of the specimens are fixed or clamped in the loading machine. The strong restraints prevent the buckling patterns from appearing near the ends.

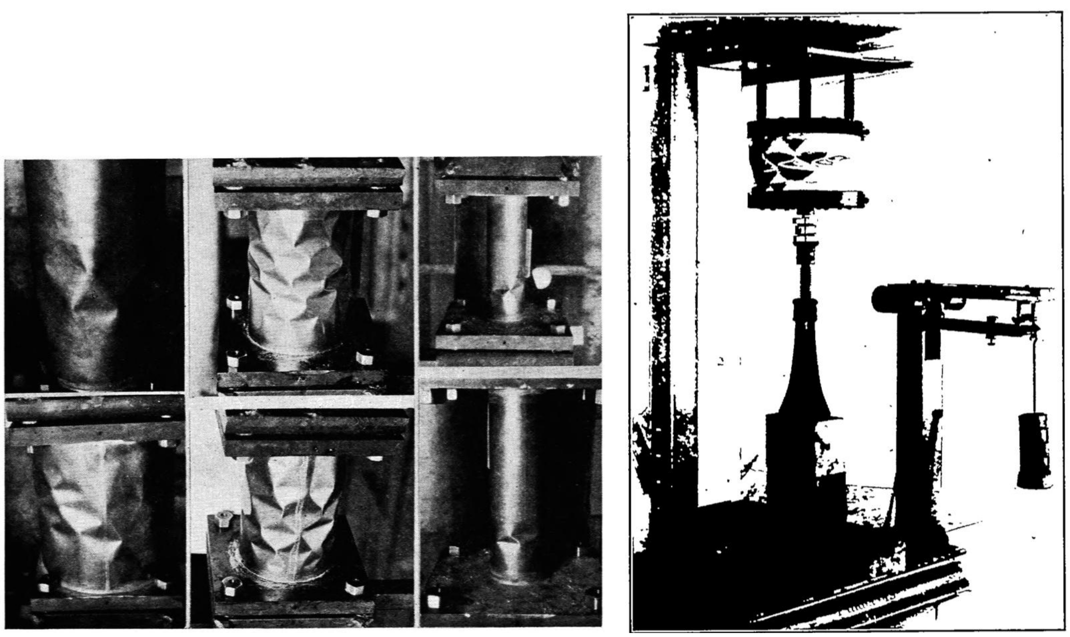

(a) Donnell's clamped specimen [6] (b) Lundquist's hinged specimen [13]

Figure 3.10: Test set-up in with previous research

Regarding the test conditions, the fixed end provides the strongest boundary, it is expected to prevent the edge buckling pattern. In practice, the pure clamped (Fixed-Fixed) end may induce local in-extensional deformation at the edge. The hinge boundary (Hinged-Hinged) is suggested to avoid the edge bending, and both ends are constrained by the translational degrees of freedom. Moreover, the hinge boundary is neglected the friction between the contact. Hence, there is a variation of only the tangential direction (Tan-Tan) is constrained, to release the friction of the expansion. Besides, the restraints in the radial direction (Radi-Radi) only and the top free (Free-Hinged) is also tested as comparisons.

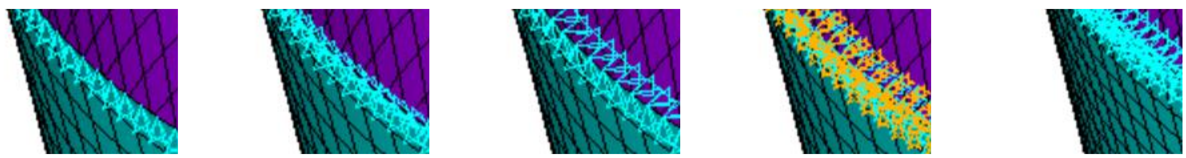

(a) Free-Hinged (b) Tan-Tan (c) Radi-Radi (d) Fixed (e) Hinged

Figure 3.11: Five kinds of boundary conditions

3.3.2.2 Different Boundary Conditions

The LBA as an estimation trial, is applied to assess the structural behaviour under different boundary conditions.

For the cylinder and the spheroid model, the insufficient end constraints will induce the buckling pattern just near the edge. And only if the end is fixed or hinged, the buckling could take place in the middle.

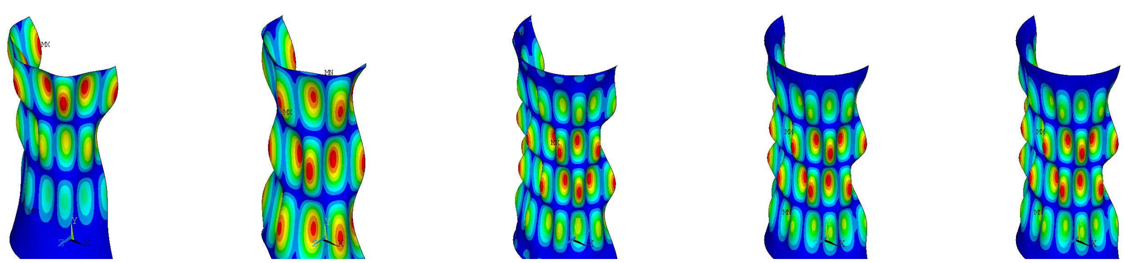

(a) Top free & bottom hinged (b) Tangential (c) Radial (d) Fixed (e) Hinged

Figure 3.12: 1^{st} modal in hyperboloid buckling of different boundary (LP-200: Hyperboloid, Rd=2500mm, Rk=20000mm, H=10000mm, t=10mm, E=210000MPa, ν=0.3, 1^{st}modal imperfection, δ_{imp}=0.5t, different boundary conditions)

In hyperboloid, the relation between the extent of the edge restraint and the linear buckling pattern is much more clear. In the free edge model, the buckling dents inevitably take place in the less restraint side, and the edge buckling dents appears. With the increase of With the assistant of hoop force, the restrained deformation is sufficient to prevent the edge buckling. The difference between the hinged constraints and the fixed constraints are limited. Moreover, the model with the only radial constraints has the similar behaviour of the hinged constraints. From the F-D curve of different boundaries, the radial restraints provide the similar stiffness of the structure. The stable edge shape provides the identical structural behaviour with the hinged model in the start stage, but the stress concentration at the edge damage the specimen in 20% load comparing with the hinged boundary. However, such phenomenon does not exist in the cylinder, and the lack of hoop force makes the load be an eccentricity in cylinder end and the cantilever behaviour damage the specimen in much earlier load stage. The tangential boundary is designed to release the edge expansion in friction, but it is insufficient to provide the edge constraint, and the model fails very early.

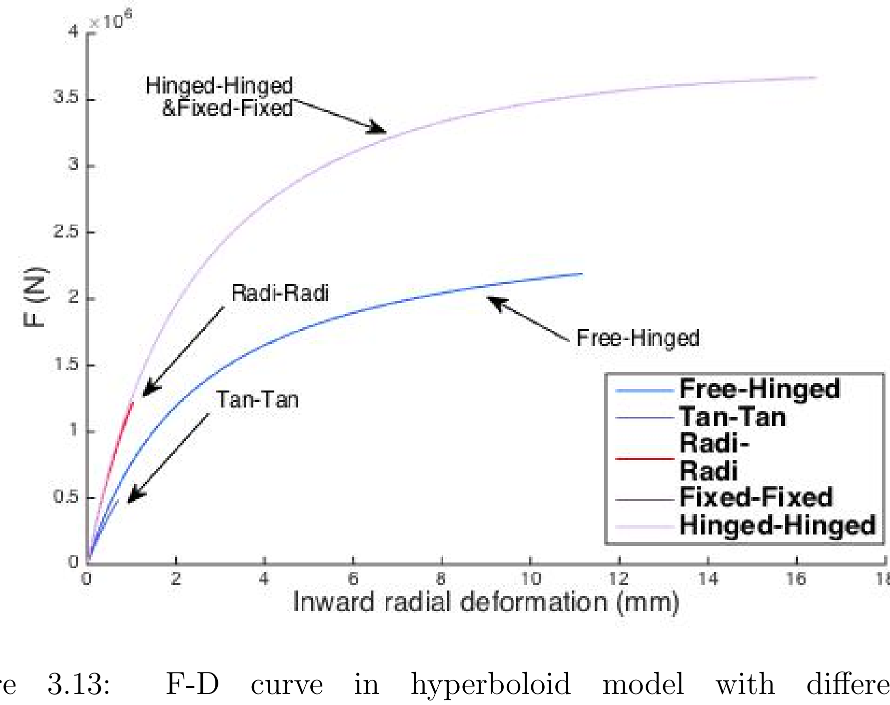

Figure 3.13: F-D curve in hyperboloid model with different boundary conditions(LP-200: Hyperboloid, Rd=2500mm, Rk=20000mm, H=10000mm, t=10mm, E=210000MPa, ν=0.3, 1^{st}modal imperfection, δ_{imp}=0.5t, different boundary conditions)

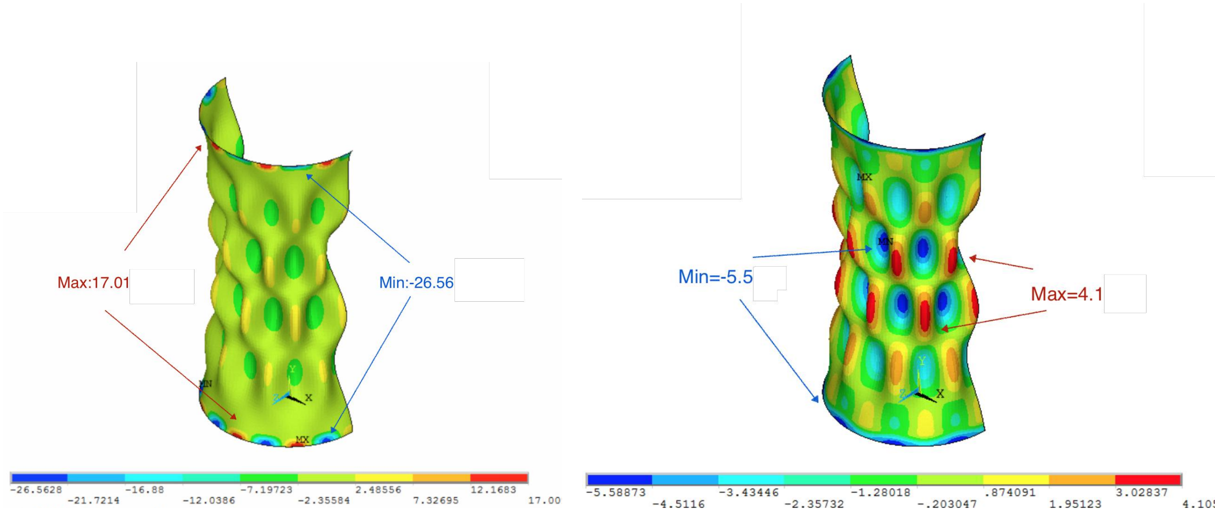

(a) Radial (b) Hinged

Figure 3.14: m_{yy-in} moment internal force (LP-200-5/LP-200-6: Hyperboloid, Rd=2500mm, Rk=20000mm, H=10000mm, t=10mm, E=210000MPa, ν=0.3, 1^{st}modal imperfection, δ_{imp}=0.5t, boundary conditions in radial restraints and hinge restraints)

It is concluded that the end restraints have an influence on the buckle distribution, and the strong restraint is beneficial to stabilize the dents away from the edge. To simulate the friction to release part of the radial expansion, the interface elements are supposed to used on the edge.

3.4 Imperfection Generation

3.4.1 Imperfection Introduction

Following the report of Chen [4] on the shell imperfection analysis, there are four basic imperfection model in shell nonlinear buckling analysis, which are the modal shape, the combination of modal shapes, the periodical function shape and the random imperfection generation. Moreover, the combination method offers the lowest result, but the accuracy is traded from the iterations on the combination factors; and the random imperfection method relies on the mesh result too much, hence its not stable enough. Neither of these two methods is a suitable alternative to generate the imperfection in batch through the script.

On the other hand, the first modal shape imperfection provides the enough accuracy, and the clear physical meaning of the periodical function shape is suitable for the parameter sensitivity analysis. Hence, in this test, both the first order modal shape and the periodical function shape are used as imperfection.

The amplitude of the imperfection shape from the first order of modal shape is adjusted by parameter of ratio to the thickness, which is designed to adjust model imperfection extents. Besides, with the help of the periodical function, the dents distribution and extent are simulated with the parameters in wavelength m/n and the amplitude as well.

In the latter analysis, because the distribution of dents in the modal shape depends on the model instinctive shape and the buckling locations are not able to be stabilised at the middle area. If the elements buckle near the boundary, the influence of the edge disturbance can not be neglected. Besides, the buckles distributed in the edge area have a great influence on the force path, and the compression strips appears rather than the uniform distribution compression appears, section 3.4.3. To eliminate the edge influence caused by the unexpected modal shapes, the imperfection reduction factor is supposed. This factor is designed to concentrate the imperfections in the middle of the area, and reduce the imperfections near the edge. The imperfection reduction factor is described through the piecewise function, the function keeps the unit value in the middle range, to generate the imperfection shape; and the decreasing function value is defined in reaching the boundary. Moreover, the type of the decreasing function is investigated, and the sensitivity study is required.

3.4.2 Imperfection Type

The discussion on initial imperfection is based on deterministic imperfection and stochastic imperfection [7]. The applied deterministic imperfection method is based on imperfection shape and extent. Although Koiter's comment that only qualitatively the degree is sensitive on buckling behaviour. The other study shows imperfection shape influences the buckle as well. The imperfection shape is always able to be expanded to series of linear buckling modal shapes. Considering the computation capacity and the difficult of the analysis, the first buckling modal shape is treated as almost the critical imperfection shape in practice. For practical view, the first linear buckling shape is applied in finite element analysis.

3.4.2.1 Modal Shape Imperfection

The modal shape is generated from the linear buckling analysis. In previous research [4], the single modal imperfection and the combination of modal shape have been investigated. In fig 3.15, different modal shapes have different reduction effects, but the first modal is the most practical method to generate the imperfection.

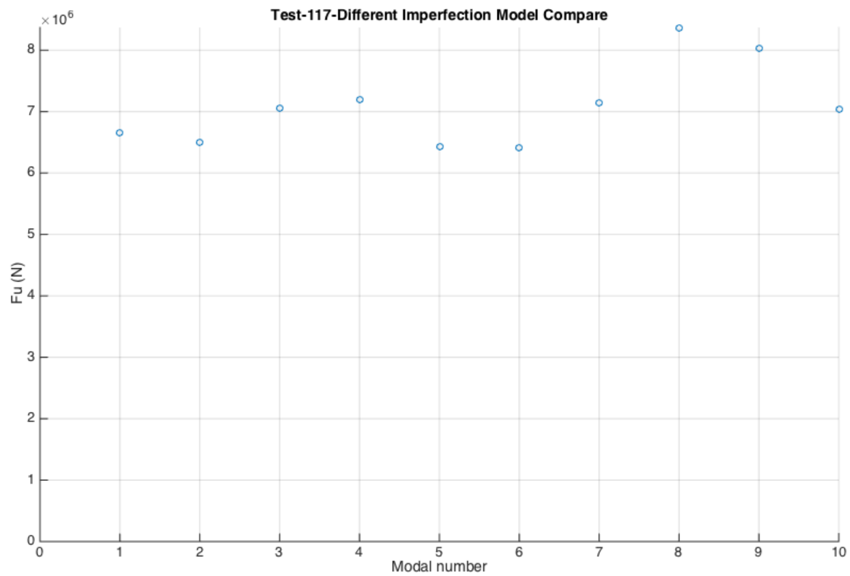

Figure 3.15: Ultimate with different modal shape imperfection (LP-117: Cylinder, Rd=2500mm, H=10000mm, t=10mm, E=210000MPa, ν=0.3, different modal shape imperfections, δ_{imp}=0.5t)

The combination of several models is possible to reach the lower boundary of the buckling load. However, the random combination does not produce a conservative result, and it is necessary to enumerate the combination as much as possible, which will cost much calculation load. His report also suggests that the use of first buckling modal shape as the imperfection pattern is a balanced choice, and the knocked down factor is validated.

In modal imperfection method, the key parameter is focused on the selection of modal shape and the amplitude of imperfection.

3.4.2.2 Artificial Imperfection

Because of the location of the modal shape imperfection depends on the different modal shapes, the edge protuberance imperfection will induce the buckling dents develop nearby the boundary. In order to investigate the free element buckling behaviour, the edge disturbance should be avoided. It is supposed to localize the maxim imperfection dent in the middle. Besides, to simulate the linear buckling shape, the periodical wave is used to generated serial dents, whose extents reduces from middle to edge.

The analytic Artificial Imperfection is provided by Dr.Ir. P.C.J. Hoogenboom.

$$U_{imp} = -\{Imp_h \cdot \cos(n_{wh} \cdot \pi \cdot h_r) + Imp_r \cdot \cos(n_{wr} \cdot \pi * r_r)\} \cdot \cos^2(h_r * \pi) \tag{3.4}$$

$$h_r = \frac{0.5 \cdot h0 - h}{h0}$$
$$r_r = \frac{r}{2 \cdot \pi}$$

$Imp_h; Imp_r$	imperfection amplitude in height direction and in radial direction
$n_{wh}; n_{wr}$	the number of imperfection in both directions
h	height of the centre of the specified element
r	height of the centre of the specified element
$h0$	height of the specimen

The last part of the eq 3.4, $\cos^2(h_r * \pi)$, is applied to decay the extent of the dents from the equator to the edge.

The parameter in the periodical function is used to control the number of imperfection wave in both directions. From the point of describing wave development, the wavelength, which is h_0/n_w should be large enough to contain at least six elements. Besides, the number of waves is restrained by the influence length and the correspondent critical buckling pattern. Hence, the critical wavelength is also discussed later.

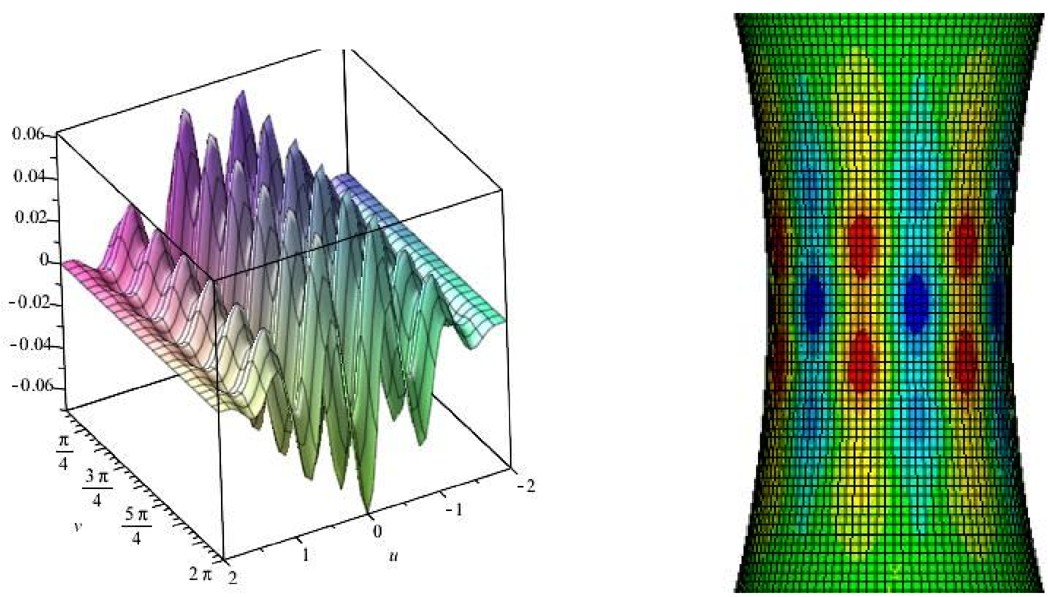

(a) Mathematical expanded surface plot

(b) Example of the artificial imperfection on the hyperboloid

Figure 3.16: Artificial imperfection and its application

However, the character of the artificial imperfection expression makes the peaks concentrate in the middle of the model, which is only suitable to be applied to the cylinder and the hyperboloid model. The critical buckling pattern of the spheroid model is distributed at the boundary part, and hence the middle concentrated pattern is not a safe solution. The trial has been done, with a comparison between the first modal shape and the artificial imperfection. The artificial imperfection does not stimulate the buckling, but it even postpones the buckling happen. For this reason, the application of the artificial imperfection model on spheroid is limited.

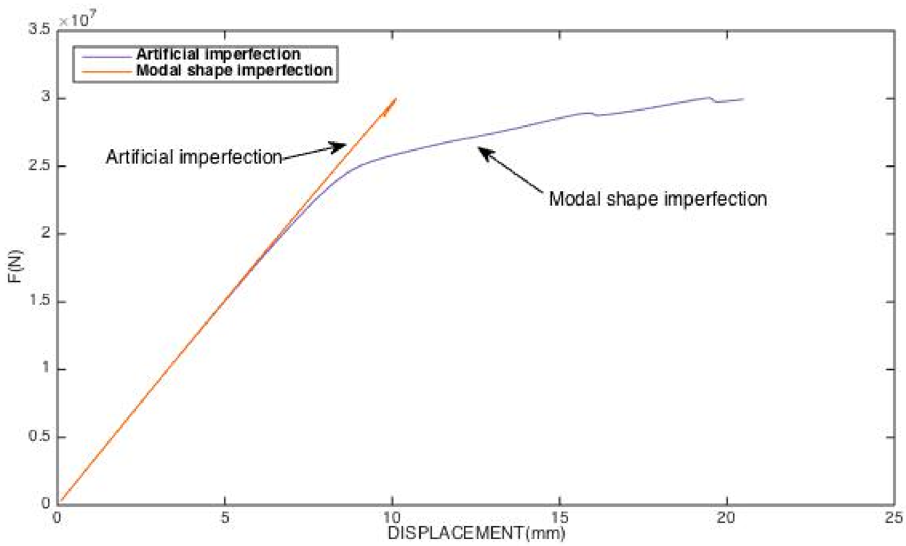

Figure 3.17: F-D comparison between the imperfection and the first modal imperfection (LP-122-10/LP-128-3: Hyperboloid, Rd=2500mm, Rk=20000mm, H=10000mm, t=10mm, E=210000MPa, ν=0.3, 1^{st}modal imperfection and artificial imperfection, δ_{imp}=0.5t)

In artificial imperfection formula, three key parameters are mentioned: amplitude and the wave length in both direction.

3.4.3 Reduction Factor Modification

Both of the previous imperfection methods are based on the global geometry, it can not deal with the edge distributed imperfection, which appears in some cylinders and most of spheroid. Such buckling phenomenon is quite different with the middle concentrated pattern. Because the edge disturbance is precluded in this research, the author try to make a modification method to prevent the edge buckling dents.

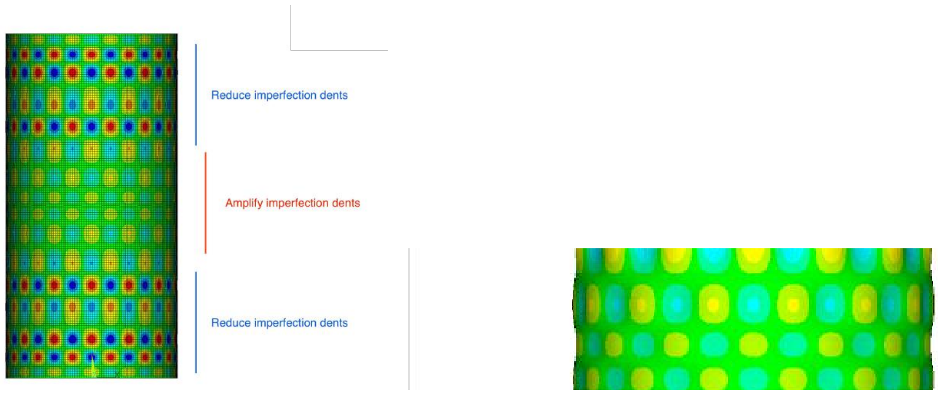

(a) Original model (b) Zoom in to the middle dents

Figure 3.18: Edge distributed imperfection and its middle part

(a) Original model (b) Imperfection reduced model

Figure 3.19: Original modal shape and imperfection reduced shape (LP-125-5/LP-185-1: Cylinder, Rd=2500mm, H=10000mm, t=10mm, E=210000MPa, ν=0.3, 1^{st}modal imperfection and imperfection reduction factor method, δ_{imp}=0.5t)

The reduction factor is supposed to concentrate the imperfection in the middle, and the author try to figure out a method to generate similar critical imperfection dents distribution pattern. The main purpose of reduction factor is to modify the dents extent by their distance to the equator. According to the distance to equator, the piecewise function is separated into two parts: 1). in the middle part, the constant value is used, and the maximum extent is amplified to the expected imperfection amplitude. 2). in the edge part, an exponential function is applied to reduced dents extent, and if the reduced extent is still larger than the maximum in the middle, the reduced process will be executed again.

$$R_d = \begin{cases} r_{amp} = \frac{\delta_{imp}}{\delta_{mid}} & \text{if } \frac{h0}{2} < h_{re} < h_{edge} \\ r_{dec} = e^{1-|\frac{h_r}{0.5}-1|} & \text{if } h < h_{edge} \end{cases} \tag{3.5}$$

in which δ_{mid} is the maximum radial displacement in the middle area; δ_{imp} is the imperfection amplitude.

The main feature of reduction factor is that this method is based on the original buckling model, and the distribution of the dents are preserved.

Moreover, the reduction factor also solves the problem on the non-uniform boundary reaction force. The specimen is designed to loaded under the uniform compression. However, if the boundary reaction is zoomed in, the actual reaction force is the periodical distribution. The protuberance in the edge have an effect on the reaction force distribution, the periodical force distribution will change the axial compression into the axial-symmetrical column compression, the load transfers through discrete area rather than the whole ring part. In detail, the fig 3.20 shows that the edge protuberance make the bypass for force into neighbourhood area. The reduced dents extent will equalize the edge load distribution, and the expected uniform compression load distribution is produced.

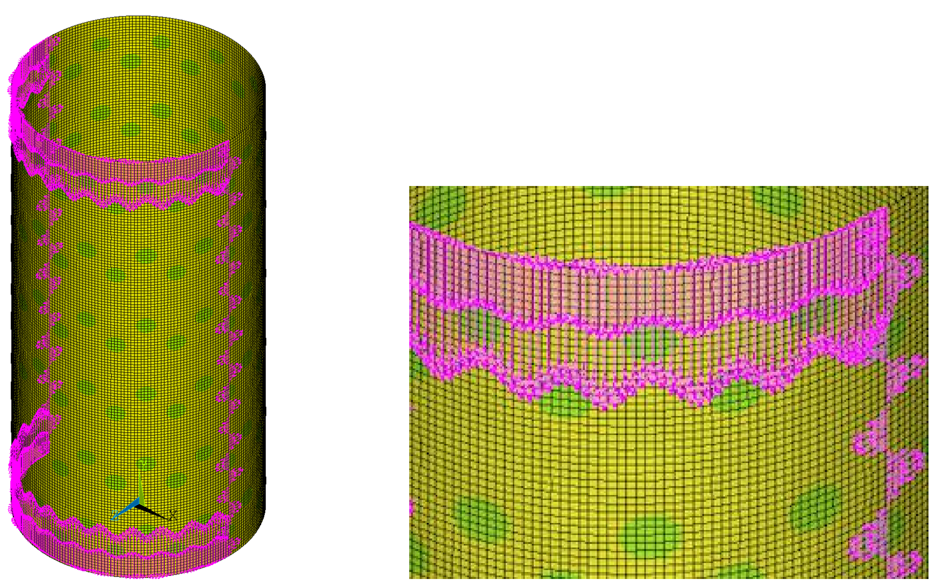

Figure 3.20: Non-uniform boundary reaction force

In the reduction factor modification method, the key parameter is focused on the selection of the basic modal shape and the reduction formula, the default option is the exponential formula, reduction area as well.

3.4.4 Edge Tension Stress

The tension in edge area is a much more straight method to avoid the buckling near the edge. The pretension will neutralize the buckling compression stress increment. The initial condition of the specimen is following.

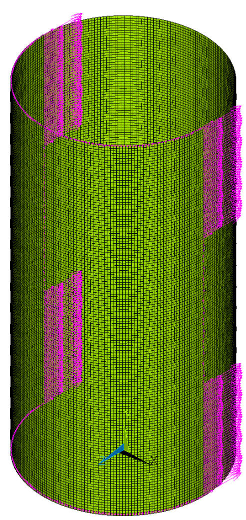

(a) Pretension in the edge zone

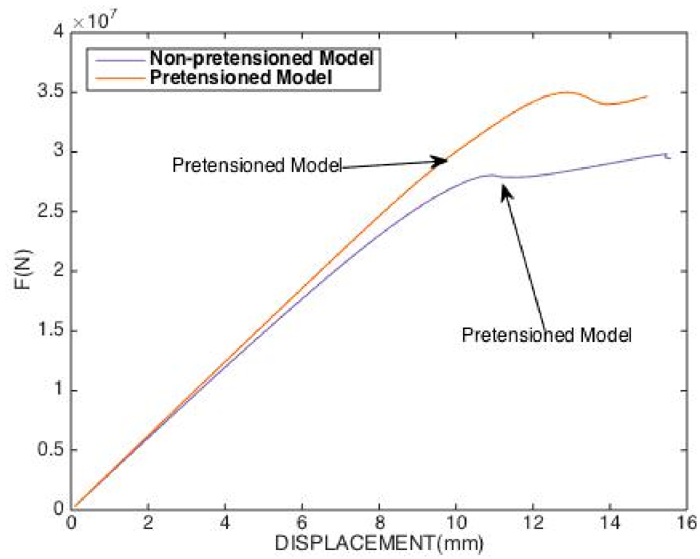

(b) Comparison of the influence of the edge pretension

Figure 3.21: Comparison between the pretension in edge zone (LP-127-1/LP-118-5: Cylinder, R=2500mm, H=10000mm, t=10mm, E=210000MPa, ν=0.3, edge pretensioned and1stmodal imperfection, δ_{imp}=0.5t)

The effect of stabilization and concentration is expected. Moreover, the influence is restrained in the edge local are, and the entire model behaviour, like the stiffness and ultimate load, does not change greatly. It is stated that the initial stress is induced in six degrees, and only the ring stress is modified, the others are not pre-tensioned. Otherwise, the load is not able to transform successfully. The edge tension stress is a direct method to stabilize a middle area buckling, with the uniform distributed.

In edge tension method, the key parameter is height of tension zone, and the tension stress extent.

3.5 Linear Buckling Result

3.5.1 Cylinder

According to the first twelve buckling modal shapes with the $E_{asp} = 1.0$. The buckling modal are classified into three kinds, which are middle concentration, edge concentration, and uniform distribution. Besides there is also one important shape in the higher modal, which is the ring pattern, also called axis-symmetrical shape(fig 3.23).

Table 3.3: First 100 buckling eigenvalue of the cylindrical shell specimen (LP-129: Cylinder, R=2500mm, H=10000mm, t=10mm, E=210000MPa, ν=0.3, LBA)

order	**eigenvalue**	**rel to 1^{st} %**
1	22.9426	
2	22.9431	0.00217935
3	22.9587	0.07017513
4	22.9657	0.10068606
5	22.9917	0.21401236
...		
10	23.0078	0.28418749
20	23.0349	0.40230837
30	23.0539	0.48512374
40	23.0632	0.52565969
50	23.0714	0.56140106
100	23.2308	1.25617846

According to the table 3.3, there are limited difference between the first 100 eigenvalues. It indicates that the estimated buckling load factor are value, with slight imperfection, it is possible to stimulate most of the buckling shape.

In this research, the free edge zone is expected, and the edge disturbance should be avoided, such as the 3^{rd}buckling modal. For this reason, the dents distribution should be checked carefully in latter tests.

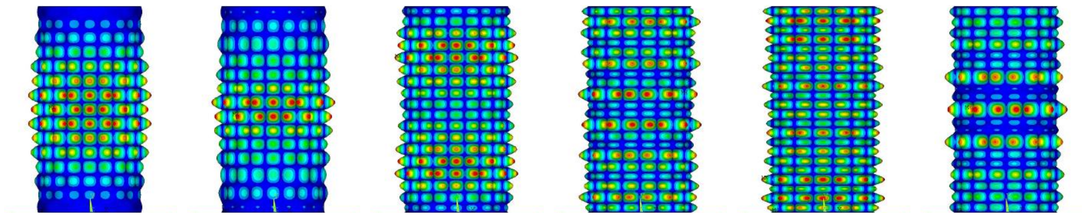

(a) $1^{st} - 6^{th}$Buckling Modes

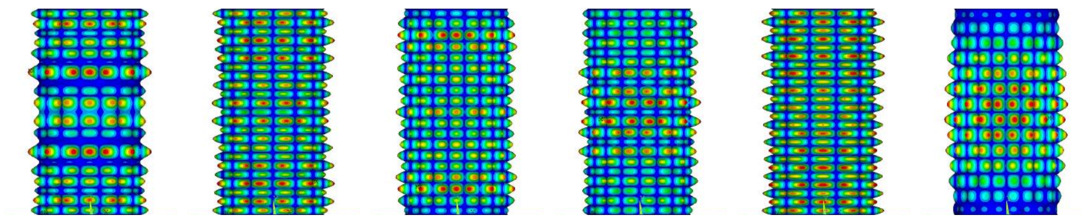

(b) $7^{th} - 12^{th}$Buckling Modes

Figure 3.22: First 12 buckling modes with $E_{asp} = 1.0$ (LP-129: Cylinder, R=2500mm, H=10000mm, t=10mm, E=210000MPa, ν=0.3, LBA)

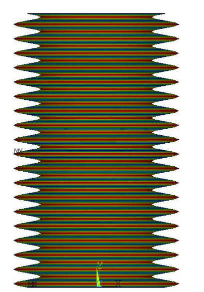

Figure 3.23: Ring pattern buckling in 50^{th}

3.5.2 Double Curvature

The buckling shapes of the hyperboloid and the spheroid are much more stable with the aspect ratio, and the first modal does not change any more with the E_{asp}. Because of the distinct limit between the eigenvalue, the double curvature is insensitive to the FE parameters.

The hyperboloid buckles in the chessboard pattern, and in each wave, there are at least 20 elements. It is sufficient to describe the buckling wave.

However, it is noted that the deformation of spheroid concentrates in the edge area and the wavelength are smaller than the dents,Figure. 3.33. It is assumed that there are not enough element density to generate the buckling wave, and the buckle are restrained. Hence, the element size is reduced to 60%, $msize = 44$to ensure the sufficient element density. The buckling pattern keeps the same, each buckle wave contains sufficient elements to deform.

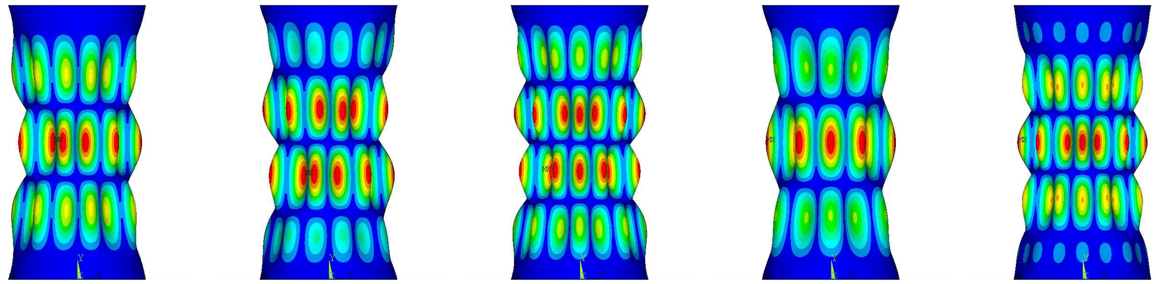

(a) $\lambda = 9.14$ (b) $\lambda = 9.57$ (c) $\lambda = 9.77$ (d) $\lambda = 10.07$ (e) $\lambda = 10.10$

Figure 3.24: $1^{st} - 5^{th}$ Hyperboloid buckling modal and eigenvalue at $E_{asp} = 1.0$ (LP-130: Hyperboloid, Rd=2500mm, Rk=20000mm, H=10000mm, t=10mm, E=210000MPa, ν=0.3,LBA)

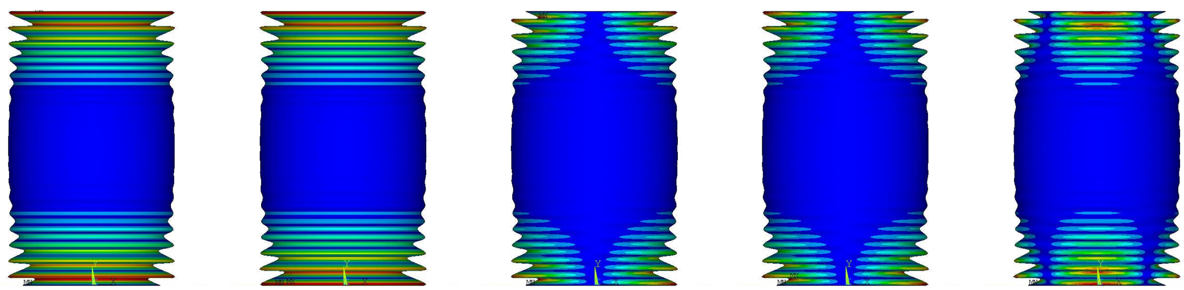

(a) $\lambda = 20.46$ (b) $\lambda = 20.46$ (c) $\lambda = 20.47$ (d) $\lambda = 20.47$ (e) $\lambda = 20.48$

Figure 3.25: $1^{st} - 5^{th}$ Spheroid buckling modal and eigenvalue at $E_{asp} = 1.0$, (LP-131: Spheroid, Rd=2500mm, Rk=20000mm, H=10000mm, t=10mm, E=210000MPa, ν=0.3, LBA)

3.6 Parametric Analysis

3.6.1 Model Parametric Analysis

In this chapter, the further investigation is focused on the mesh parameters in the numerical model generation. The preliminary study has already shown that the model behaviours strongly depends on the element size and the element aspect ratio as well. The aspect ratio is the main variable in following tests, and both the fine and coarse element size are adopted. Besides, in the nonlinear buckling analysis, the imperfection is induced. The influence of the mesh parameters is examined in three different geometry separately.

The element nodes are arranged in vertical sequence, and the rotation of angle between each column is constant. Therefore, the vertical height and rotation angle are used to define the element shape. In order to describe the element, two parameters are used element size and aspect ratio. The element size is defined as vertical size of the element, and the aspect ratio describes the shape, i.e. aspect ratio is by 1, meaning that the square shape.

It is obvious that element size influence the accuracy of the numerical model, and it is preferable to mesh the model as smaller as possible. However, the smaller element size will increase the amount of elements quadratically, and the computation capacity may limit the element size.

The common requirement on the element size is to limit its influence on linear buckling analysis, which means the eigenvalue is stable, even if the smaller mesh is utilized. Besides, the element size should be fine enough to generate protuberance of the shape, too coarse meshes are not able to shape the deformation smoothly. It is estimated that there are 15 buckling waves in vertical. Considering the total height is 10000, and each buckling wave contains ten elements, means the element size is nearly $msize = \frac{10000}{10*15} = 60$. Hence, the coarse is defined to 90, and the fine is 60.

3.6.1.1 Geometry Influence on Model Generation

3.6.1.1.1 geometry influence

The element size and the aspect ratio are two key parameters in the model generation. The smaller mesh is always expected, but how to balance the computation load and the accuracy is discussed here. Besides, considering the node coordination are equivalent distance the vertical, the double curvature geometry does influence the element shape. In this section, their influence is going to investigate.

$$E_{asp} = \frac{m_{height}}{m_{size}}$$

,where the m_{size} is the element size of the element

3.6.1.1.2 aspect ratio

The finite element model is generated through the node coordination direction. According to the definition, the lower E_{asp}, the more slender element shape is; the high E_{asp} means the flat element shape is. In order not to import the ill element shape, the E_{asp} is restrained between 0.8 to 1.2. In the process, the nodes are mapped with equivalent distance and rotation angle in height and perimeter direction. Hence, the cylinder is meshed into congruent size, and the aspect ratio will change slightly in a double curvature model, such as the hyperboloid and the spheroid. It is clear that such aspect ratio variation will change smoothly if the model is meshed in a smaller element, and the contour of the E_{asp} is plotted following.

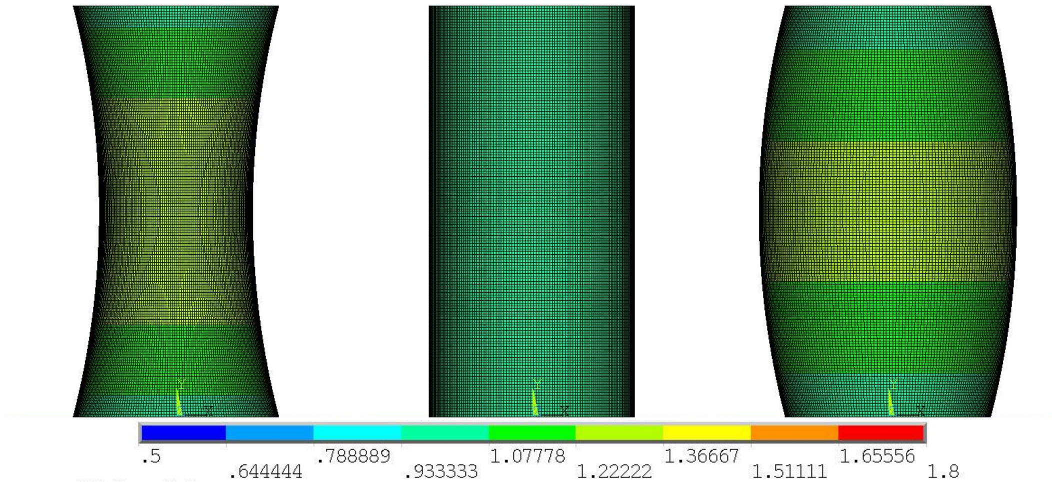

Figure 3.26: Aspect ratio distribution in different geometries

For cylinder specimen, the linear buckling shows the similar shapes for the first modal of the eigenvalue analysis, the peak dents are focus at the middle. The wave number in vertical and horizontal also keep stable with the varying aspect ratio, except for the smallest aspect ratio model there are two wave less than the others. For correspondent eigenvalue of the first modal, the difference is limited in % also. In the view of the general distribution are identical and the slight divergence in eigenvalue, we can conclude that the influence on cylinder linear buckling analysis is negligible.

For hyperboloid and spheroid, the varying aspect ratio almost have no influence on the linear buckling behaviour, neither the buckling dents pattern nor the result of the eigenvalue.

With the artificial imperfection method, the identical defect pattern are implemented on the specimens with varying aspect ratio. From the F-D curve are exactly similar to each model, we can say that the aspect ratio influence on GNLBA with identical imperfection shape is limited.

It is noted that the artificial imperfection is used to eliminate the difference between the imperfection shape, and it does not always simulate the first buckling modal, which is namely the critical imperfection situation. To investigate whether the aspect ratio will influence the critical buckling situation, the test implements the same distribution, which is the first buckling shape. As previously indicated, the changing aspect ratio cause a slightly difference in the first buckling shape, but in the artificial imperfection model, its influence is limited.

We can conclude that the changing aspect ratio does not produce any influence on GNLBA if only the identical geometric imperfection is applied, and with first modal shape imperfection the GNLBA results are not influenced greatly as well.

3.6.1.1.3 element size

The element size also influences on the mesh accuracy greatly. The smaller element size is always beneficial for modal simulation. However, it also increases the computation capacity dramatically. The table **??** shows the linear buckling eigenvalue with the decreasing element size.

Table 3.4: Eigenvalue with decreasing element size

element size	**Eigenvalue**	δ %
500	23.1932	
333	23.1561	0.16
222	23.1694	0.57E-01
148	23.1663	0.13E-01
99	23.1605	0.25E-01
66	23.1600	0.20E-02
44	23.1601	0.40E-03

The aspect ratio and the element size are main mesh parameters in the pre-process.

3.6.2 Imperfection Parametric Analysis

3.6.2.1 Imperfection Propose

The imperfection as a protuberance to the perfect model is used to stimulate the specimen buckle. Many kinds of imperfection type have been studied before, including the 1^{st} modal shape, the combination of modal shapes, the random dents distribution, the artificial imperfection shape, the imperfection shape bank, etc.

Different imperfection shapes with different purposes, in theoretical research, it is always focused on the limit of the influence on the perfect model. For this reason, the various imperfection type are designed to find the lower boundary of the specimen, and also unify the divergence between the experiments and the theoretical results. In practical, the modified shape is used to simulate the real imperfection, which may reduce the structure capacity. In this research, the aim of imperfection is not only to simulate the imperfect specimen, and to generate a free edge buckling zone. The buckling zone is expected to be avoided the influence of the edge disturbance. For this reason, the imperfection are designed to concentrate the buckling zone in the middle of the structure.

3.6.2.2 Imperfection on Different Geometry

For the imperfection generation in this research, there are two alternative methods: the linear buckling modal shape and the artificial imperfection. To make the imperfection concentrate in the middle, the modification is applied. The modified imperfection is based on the result of linear buckling analysis, and is designed to use the reduction factor or tension stress in edge area to avoid the edge buckling.

Based on the previous section investigates the influence of aspect ratio on the linear buckling analysis. The spheroidal model is different from the others, and it shapes an edge-distribution buckling dents, which makes the middle concentrated imperfection in the artificial imperfection meaningless,and even overestimate the nonlinear buckling load. Hence, the modified imperfection method is used.

3.6.2.2.1 imperfection for cylinder

The LBA result shows that the eigenvalue of the cylinder are very closed with each other. For this reason, the imperfection shape of the first 10 LBA is tested in GNLBA.

Considering the dents in a cylinder is distributed uniformly, not only the knock down factor, but the distribution of the buckling dents are investigated. As the specimen is designed to be buckle in the middle, to avoid the edge disturbance, the correspondent dents in modal shape should be excluded.

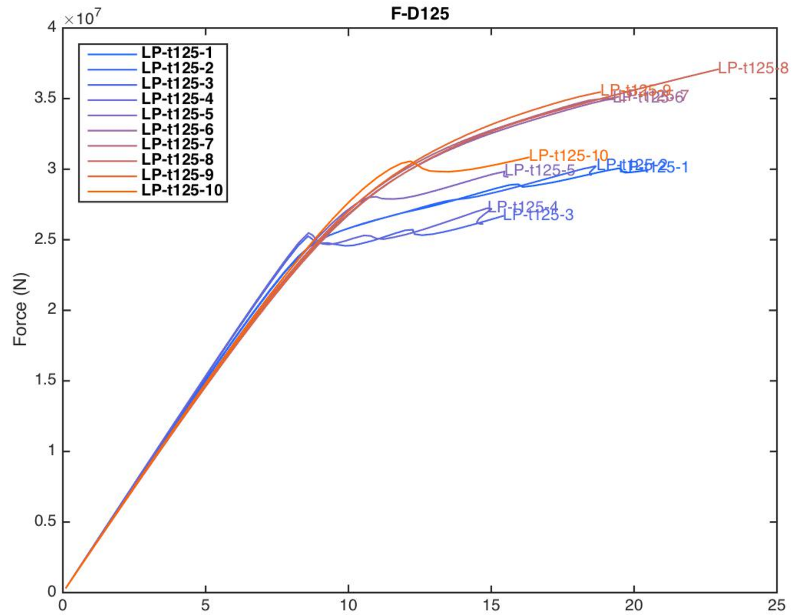

Figure 3.27: F-D curves with different modal imperfections (LP-125: Cylinder, Rd=2500mm, H=10000mm, t=10mm, E=210000MPa, ν=0.3, 1^{st}-5^{th}modal imperfection, δ_{imp}=0.5t)

Note that because of the symmetry of the cylinder, the inward dents and the outward dents positions are almost symmetric with each other.

Just as the prediction, the knock-down factor is slightly influenced by the different modal shape, the amplitude of imperfection keeps constant as $\delta_{imp} = 0.5t$. The relative height of the maximum and minimum radial deformation is monitored during the load procedure. It indicates the position of the outward dents and the inward dents. In the last part of the curve, after the specimen buckling, the relative height curve comes back with the decreasing load. It is compared to the buckling dents position with the imperfection shape ultimate load step when it buckles. The relative height is defined by the eq 3.6. It is written that considering the dents are almost uniformly scattered in chessboard and no main peak dents exists, and the peak displacement may jump between the lattice zone. Besides, the horizontal symmetry causes the peak dents jump a lot, like from $hr_{out} = 0.2$ to $hr_{out} = 0.8$, but there is no instinct change at all.

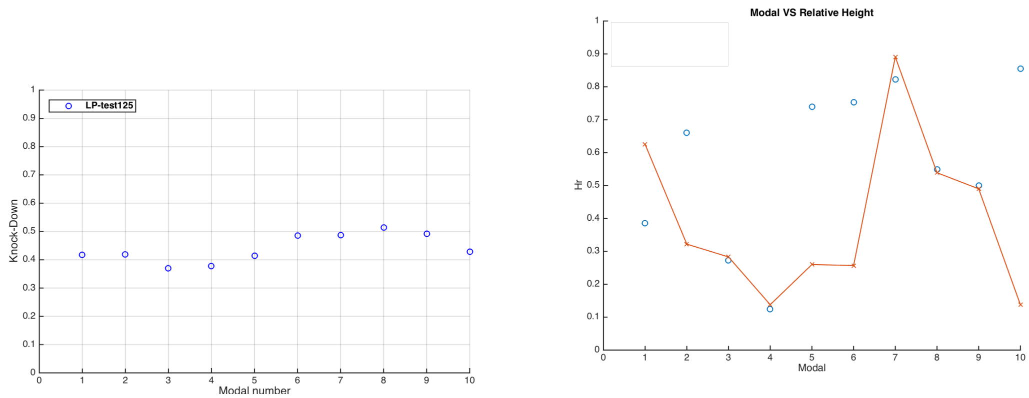

Figure 3.28: Knock down factor and relative heigh of buckling zone with different modal imperfection (LP-125: Cylinder, Rd=2500mm, H=10000mm, t=10mm, E=210000MPa, ν=0.3, 1^{st}-10^{th}modal imperfection, δ_{imp}=0.5t)

$$0 < hr_{in} = -\frac{h_{in}}{h0}; hr_{out} = \frac{h_{out}}{h0} < 1 \tag{3.6}$$

in which, the h_{in} and h_{out} are the absolute height of the position, and $h0$ is the height of the specimen.

The following plot(Figure.3.29) shows the strong relation between the dents in imperfection and those the buckling situation. In other word, the sufficient imperfection just induces the position of buckling it appears. For this reason, the imperfection shape should be carefully selected, or the modification is necessary to apply. About the modification of imperfection is going to be discussed in the latter chapter.

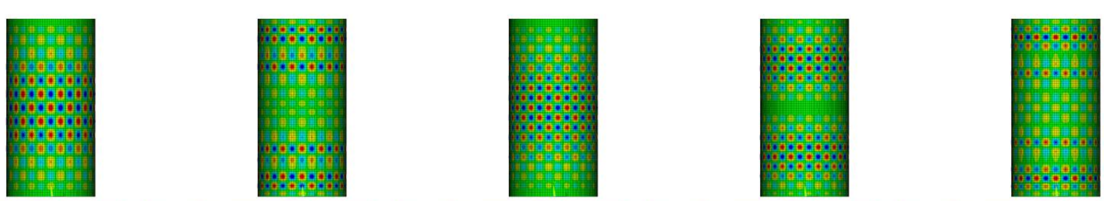

(a) $1^{st}\ \frac{Hr_{in}}{Hr_{out}} = \frac{0.655}{0.734}$ (b) $5^{th}\ \frac{in}{out} = \frac{0.803}{0.194}$ (c) $6^{th}\ \frac{in}{out} = \frac{0.724}{0.273}$ (d) $8^{th}\ \frac{in}{out} = \frac{0.664}{0.405}$ (e) $10^{th}\ \frac{in}{out} = \frac{0.240}{0.763}$

Figure 3.29: Imperfection with pattern with LBA results compared the buckling height of GNLBA for cylinder (LP-125: Cylinder, Rd=2500mm, H=10000mm, t=10mm, E=210000MPa, ν=0.3, 1^{st}-10^{th}modal imperfection, δ_{imp}=0.5t)

3.6.2.2.2 imperfection for hyperboloid

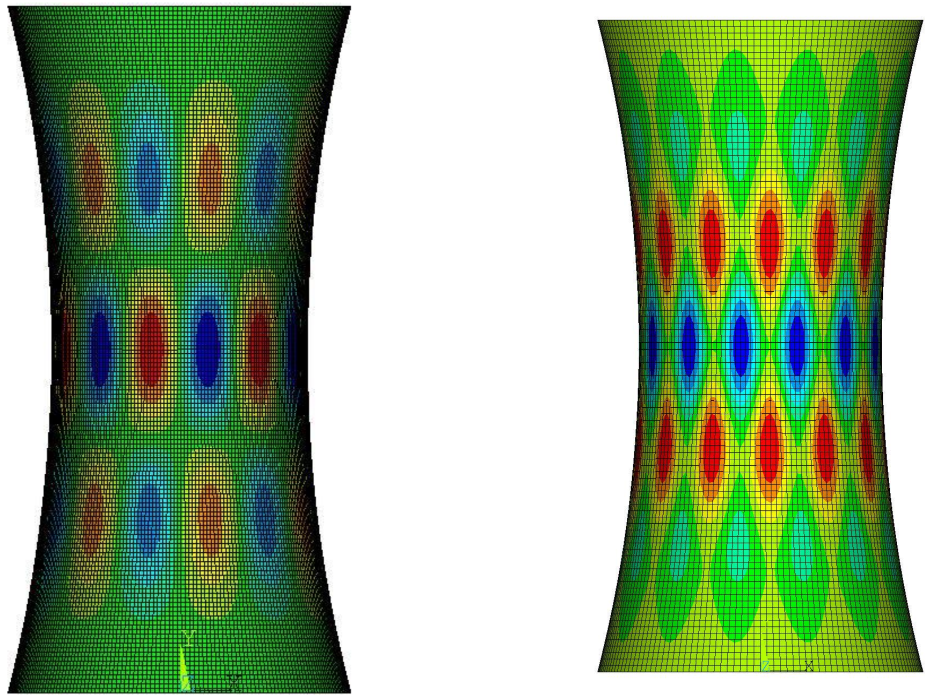

(a) the 1^{st} model shape (b) the artificial imperfection

Figure 3.30: Hyper imperfection with 1^{st} modal shape and the correspondent artificial imperfection with same buckling wave length

Table 3.5: Different wave distribution in artificial imperfection

Model No.	Art1	Art2	Art3	Art4	Art5	Art6	Art7	Art8	Art9	Art10
Vertical wave number	5	4	4	4	6	6	6	3	3	3
Radial wave number	7	5	9	8	5	9	8	5	9	8

The artificial imperfection are applied to simulate the critical imperfections of the hyperboloid specimen. For the trial, the several combinations of the wave number in the radial and the height direction are tested, in table.3.5. The ultimate load of all of these artificial imperfection combinations provide the higher results compared to the first modal shape imperfection. Fig 3.31 shows the discrepancy by different imperfection is between 5% to 30%, and its always higher than the model with 1^{st} mode imperfection. However, the most conservative results the artificial imperfection is comparable to the effect of the 1^{st} modal imperfection shapes (compared win fig 3.30). It is clear that the 1^{st} mode imperfection could be simulated by the similar.

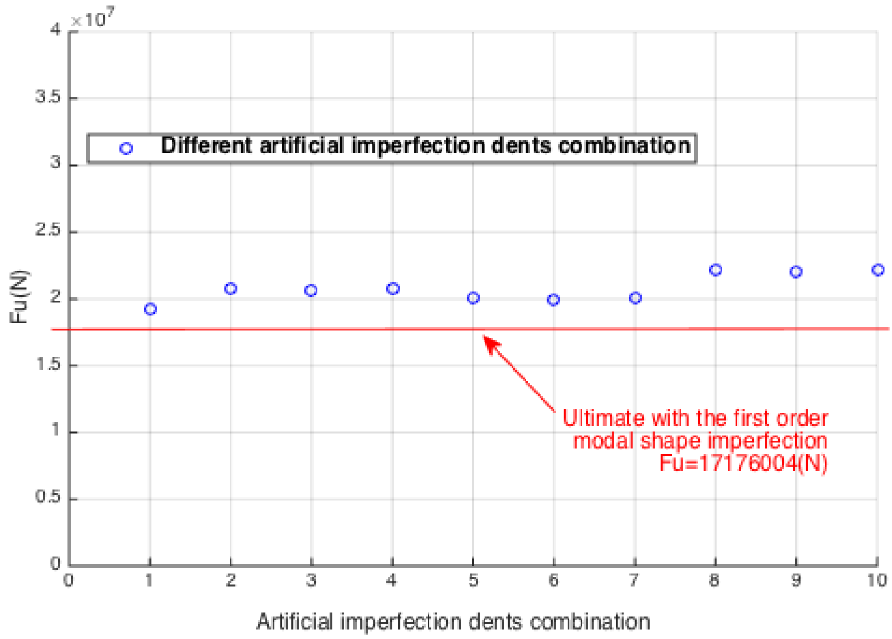

Figure 3.31: Ultimate force of a series of artificial imperfections and an imperfection in the 1^{st} modal shape (LP-128/LP-122-5: Hyperboloid, Rd=2500mm, Rk=20000mm, H=10000mm, t=10mm, E=210000MPa, ν=0.3, 1^{st}modal imperfection and different artificial imperfections, δ_{imp}=0.5t)

Although comparing use the first modal imperfection directly, to generate a conservative imperfection cost much work, the artificial imperfection method can specify the buckling wavelength manually. It is useful in the analysis on specifying the wavelength.

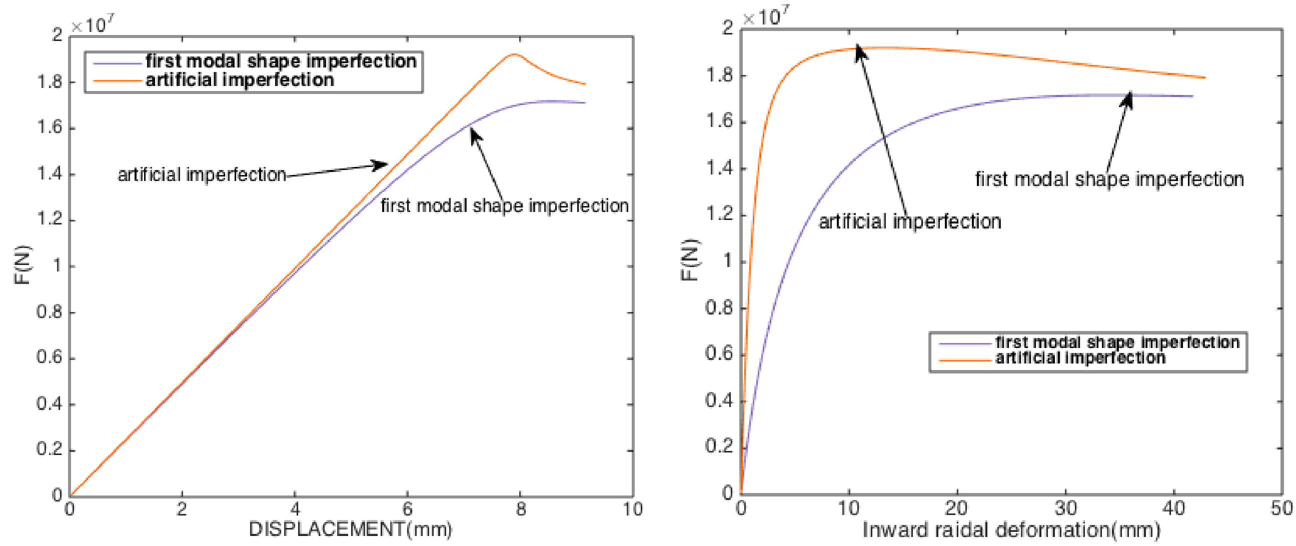

(a) Force versus vertical deflection

(b) Force versus inward radial displacement

Figure 3.32: Load displacement curves for a artificial imperfection and the modal shape imperfection for hyperboloid (LP-128-1/LP-122-5: Hyperboloid, Rd=2500mm, Rk=20000mm, H=10000mm, t=10mm, E=210000MPa, ν=0.3, 1^{st}modal imperfection and different artificial imperfections, δ_{imp}=0.5t)

3.6.2.2.3 imperfection for spheroid

Figure 3.33: Spheroid 1^{st} buckling modal shape

Different from the other shapes, the spheroid buckles near the edge fig.3.33.a. In order to stimulate the buckling in the middle zone, the artificial imperfection and edge pre-tension method are applied. The artificial imperfection(fig.3.34.a) generates the initial imperfection buckle in the middle. The fig.3.34.b shows the nonlinear analysis results between the 1^{st} modal imperfection and the artificial imperfection, the artificial approaches a larger ultimate buckling load than the model with 1^{st} mode imperfection.

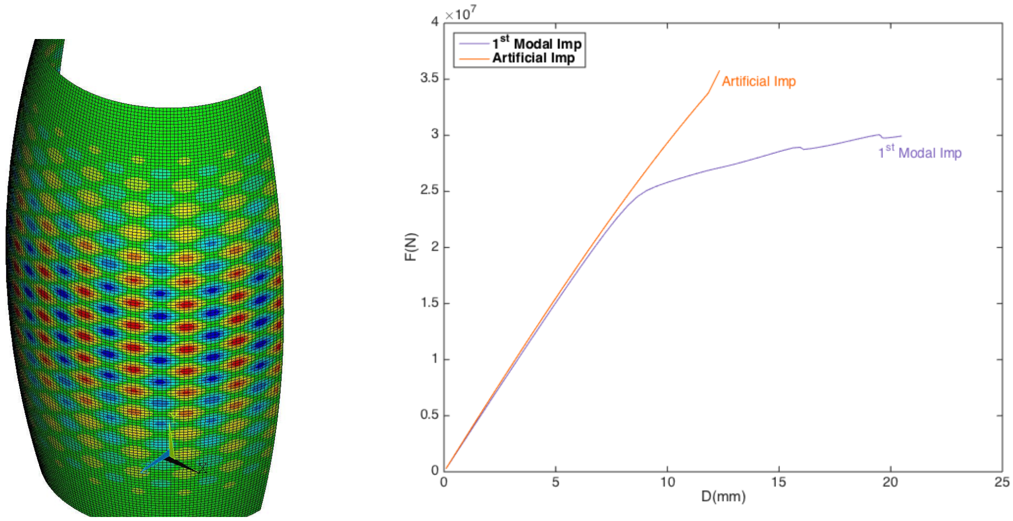

(a) Spheroid with artificial imperfection (b) Spheroid F-D curves in 1^{st} modal imperfection and artificial imperfection

Figure 3.34: Artificial imperfection buckling for spheroid (LP-126-5/LP-142-1: Spheroid, Rd=2500mm, Rk=20000mm, H=10000mm, t=10mm, E=210000MPa, ν=0.3, 1^{st}modal imperfection and artificial imperfection, δ_{imp}=0.5t)

Besides, based on the 1^{st} mode imperfection, the pre-tension method is tried to suppress the edge buckles occurrence. The initial imperfection is implemented by the 1^{st} buckling modal shape, and in addition the radial pressure is applied to implement the pre-tension in edge elements, aimed to suppress the edge deformation. However, the GNLBA shows the effect of the suppression is limited. The radial pressure pushes the edge element outward, but the edge disturbance still remains(fig.3.35).

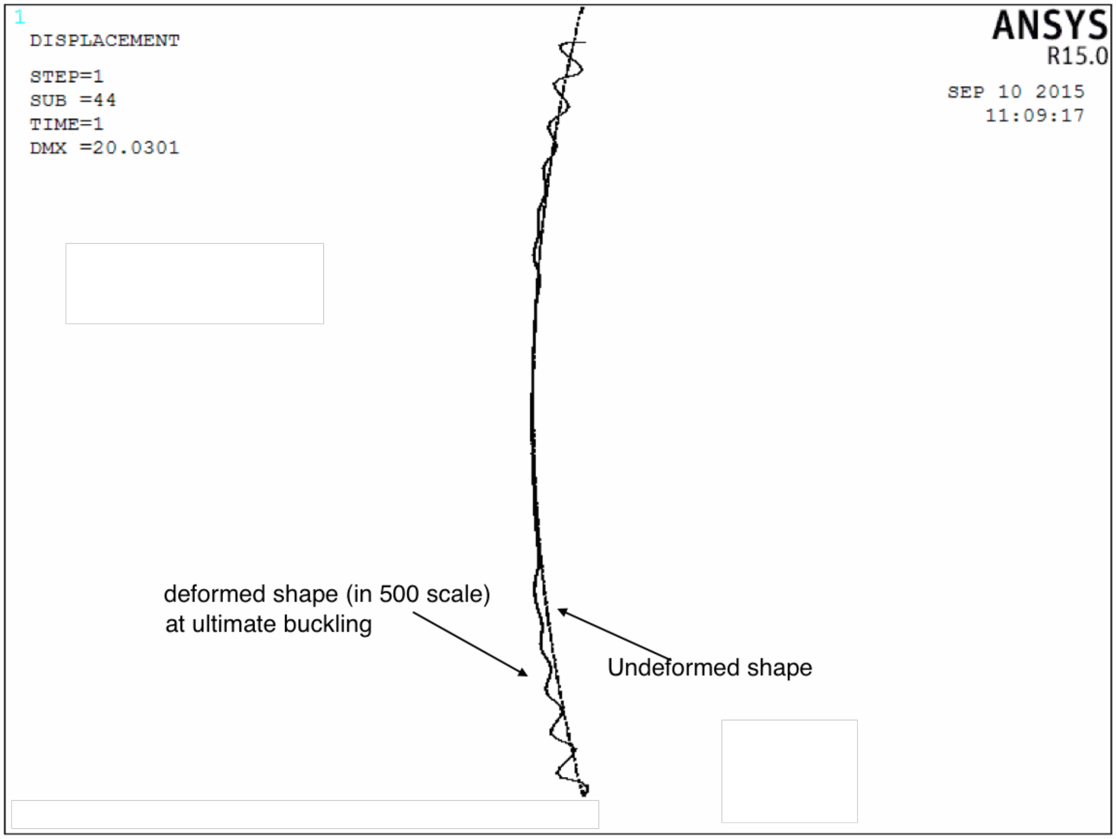

Figure 3.35: Pre-tension method on spheroid(Un-deformed and deformed cross section view) (LP-141-1: Spheroid, Rd=2500mm, Rk=20000mm, H=10000mm, t=10mm, E=210000MPa, ν=0.3, pre-tensioned method, δ_{imp}=0.5t)

3.6.2.3 Imperfection Amplitude

3.6.2.3.1 imperfection amplitude for fundamental buckling mode

The previous experiments [9] has already resulted in a serious of curves that describe the relation between the imperfection amplitude and the knock-down factor for different geometries. The comparison between the numerical results(dots) of this research and the theoretical solution are plotted together. The similar trends are achieved in the low imperfection amplitude; the divergence starts at the imperfection amplitude reaching $0.6t$. Considering the imperfection in this research in restrained in low imperfection, the difference between the FE model and the theoretical curve is not going to be discussed deeply.

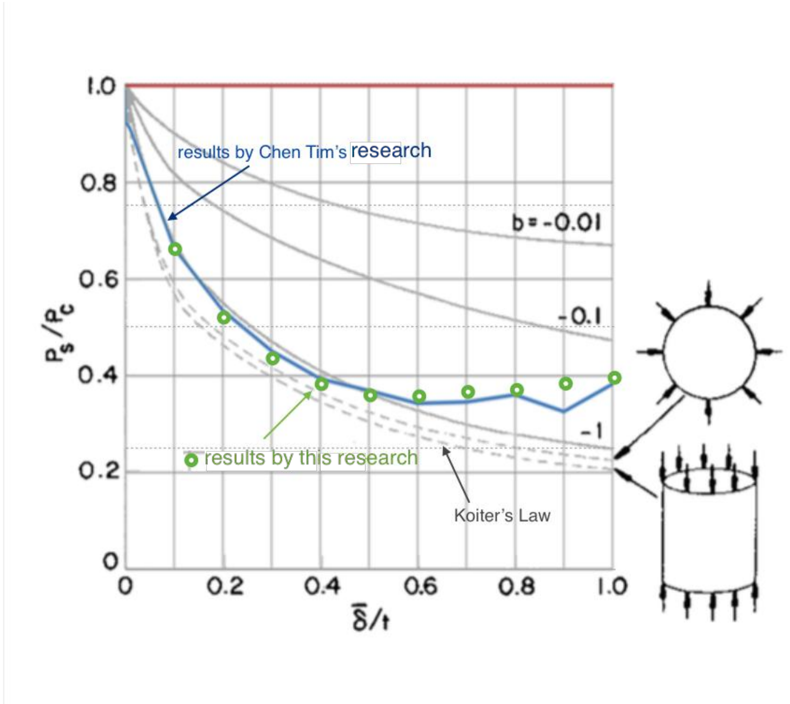

Figure 3.36: Knock-down factors of cylinders with 1^{st} mode imperfection and varying imperfection imperfection amplitudes [4]

Moreover, the load paths of the increasing imperfection amplitude are compared. It is clear that with the same imperfection type, the linear parts of each specimen are identical until reaching the peak points, the F-D curves diverge. For the near perfect model can increase the highest load. After the snap-back happens, the load reduces with the decreasing displacement, and the structure stable in a new stage. The different imperfection extent just changes the peak load of the specimen and do not influence the new stage, all of the specimens deflect in the similar post-buckling load.

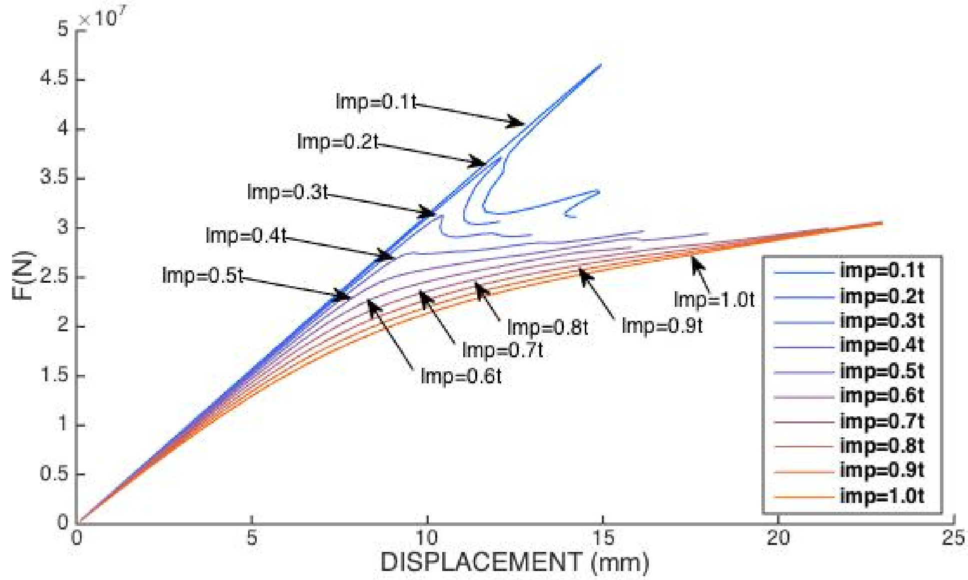

Figure 3.37: Load-displacement curves of cylinders with 1^{st} mode imperfections for several imperfection amplitude (LP-120: Cylinder, Rd=2500mm, H=10000mm, t=10mm, E=210000MPa, ν=0.3, 1^{st}modal imperfection, δ_{imp}=0.1t-1.0t)

From the F-D curves in fig 3.37. We notice that the specimen with low imperfection behaviour in the typical buckling, which reaches the peak load and suddenly the buckling happens with the snap-back. However, in the specimen with significant imperfection, there are not such clear vertex, and the snap-back is diminishing with the imperfection amplitude increase. The interaction between the membrane force and the bending moment are investigated, to expect that the significant imperfection induces the bending moment at an early stage, and the bending interaction influences the structural behaviour.

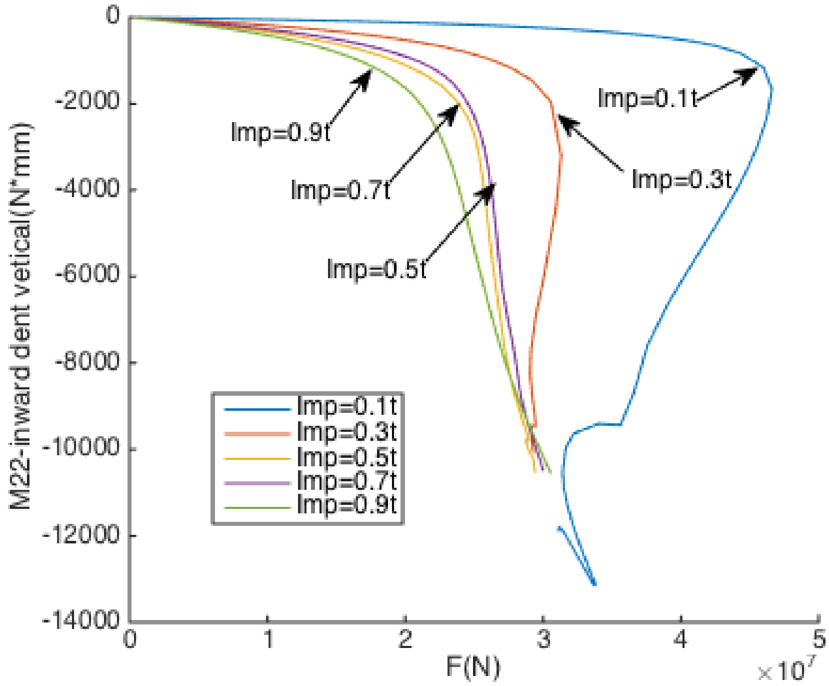

Figure 3.38: Moment in vertical direction versus increasing loading (LP-120: Cylinder, Rd=2500mm, H=10000mm, t=10mm, E=210000MPa, ν=0.3, 1^{st}modal imperfection, δ_{imp}=0.1t-1.0t)

3.6.2.3.2 imperfection amplitude for different imperfection type

In sec.3.6.2, the study about the varying imperfection amplitude with the 1^{st} buckling modal shape has already realised that the large imperfection would induce the bending moment in early stage, and there is no typical buckling behaviour. The investigation is extended to observe how the model behaves with the imperfection shape as the higher order of the modal shape and the artificial buckle distribution, under the varying imperfection extent. Figures in table 3.6 shows the buckle distribution and the amplitude indicate the extent of the imperfection.

To observe the model performance, which is imperfect with the non-first buckling modal shape, the imperfection amplitude is varied from $0.10t - 0.50t$. The ultimate buckling stage of both the 2^{nd} buckling modal shape and the artificial imperfection shape are plotted in table 3.6.

Table 3.6: Buckling Deformation of varying influence amplitude and different imperfection type (LP-294/LP-291/LP-292: Hyperboloid, Rd=2500mm, Rk=35000mm, H=10000mm, t=10mm, E=210000MPa, ν=0.3, 1^{st}modal imperfection, 2^{nd}modal imperfection and artificial imperfection, δ_{imp}=0.1t-0.5t)

δ_{imp}	Imp shape	$0.10t$	$0.20t$	$0.50t$
artificial imperfection	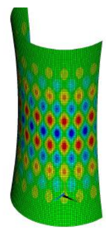	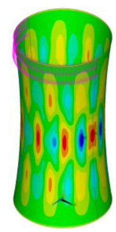	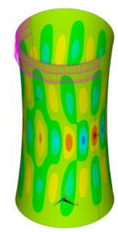	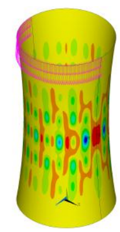
1^{st} buckling modal shape	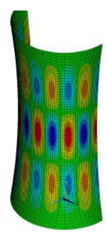			
2^{nd} buckling modal shape	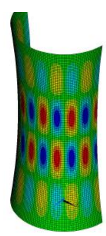	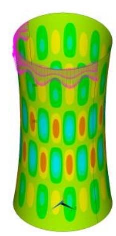	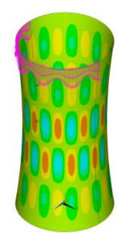	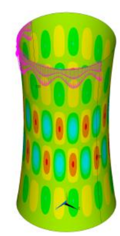

It is noted that each plot is the relative deformation plot at buckling buckling state. Hence, only the buckles distributions are compared, and the colour contours are not compared.

For artificial model, the ultimate deformed shape are distinguished by the varying imperfection amplitudes. When the imperfection is larger than $0.2t$, the buckling deformation just follows the initial imperfection shape. If the imperfection is limited to lower than $0.2t$, the buckling model is slightly divergent from the buckling modal shape and it trends to buckle at the 1^{st} buckling modal shape, which is critical buckling type of the linear buckling result.

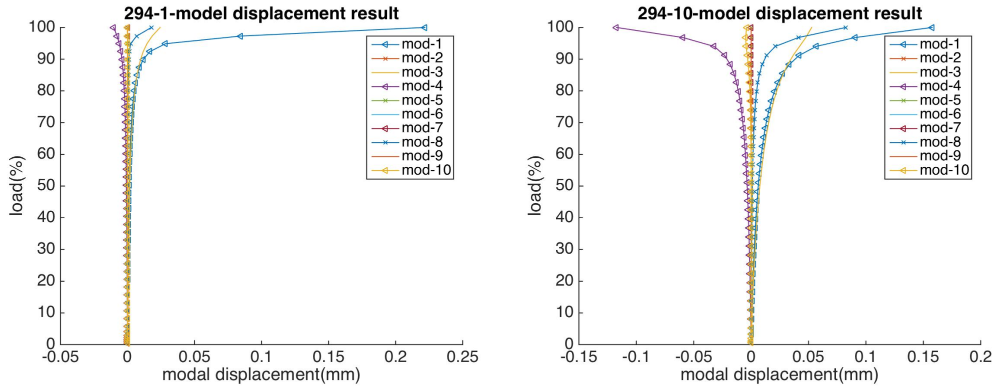

(a) $\delta_{imp} = 0.2t$ (b) $\delta_{imp} = 0.5t$

Figure 3.39: F-Modal Displacement path on the model with different artificial imperfection(table 3.6) amplitude (LP-294-1/10: Hyperboloid, Rd=2500mm, Rk=30000mm, H=10000mm, t=10mm, E=210000MPa, ν=0.3, artificial imperfection, δ_{imp}=0.1t/0.5t)

In fig 3.39, it decomposes the model deformation into its first 10 fundamental buckling modal shapes. The horizontal axis expresses the developing extent of the correspondent modal shape and the vertical axis is the load proportion to the buckling load. The detail the modal decomposition is explained in the appendix example. It is evident that in the lower imperfection amplitude model, only the most critical modal(1^{st}) is activated at buckling occurrence, and the large imperfection amplitude stimulates more higher orders of the modes in the early stage. The modal interaction phenomenon is beyond this thesis topic. To avoid the modal interaction and to stimulate the critical buckling shape, the imperfection amplitude should be limited.

However,in the 2^{nd} modal case, as the imperfection shape itself is a fundamental buckling modal shape, there is no other shape will be stimulated. The deformation is only the aggregation of the 2^{nd} modal shape, no matter with the imperfection amplitude.

Table 3.7: Imperfection influence the buckling distribution($\delta_{imp} = 0.2t$) (LP-294-4/LP-291-4/LP-292-4: Hyperboloid, Rd=2500mm, Rk=20000mm, H=10000mm, t=10mm, E=210000MPa, ν=0.3, artificial imperfection, $1^{s}t$modal imperfection and 2^{nd}modal shape imperfection, δ_{imp}=0.2t)

	A(Imp)	B(97%)	C(99%)	D (Buckling)	$F_u(kN)$ $\lambda = \frac{F_u}{F_c}$
1 (artificial)				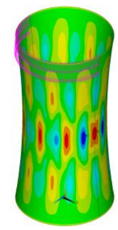	$\frac{5772.3}{0.975}$
2 (1^{st} modal)	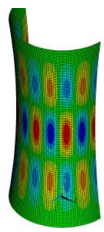				$\frac{5165.4}{0.873}$
3 (2^{nd} modal)	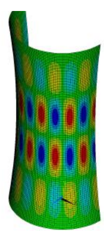	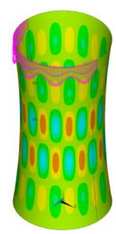	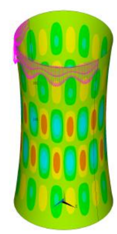	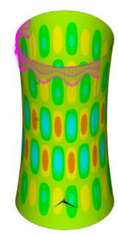	$\frac{5326.8}{0.901}$

To track how the model deformation develops in detail, the deformation process are plotted with different load stage in fig 3.7.

It is clear that even with the limited imperfection extent, the artificial imperfection still deforms with the initial imperfection shape at the load level lower than 97%. When the load reaches 99%, almost buckling, the shape of the 1^{st} buckling modal is activated, and finally it buckles at a close shape of the 1^{st} modal shape. But in 2^{nd} modal shape imperfection, the deformation aggregates continuously, till the model totally failure there is no interaction of the other order of the buckling modal shape.

It is concluded that in the limited imperfection amplitude, the artificial imperfection shape, which is treated as the combination of the series of buckling modal shapes, is able to stimulate the critical buckling modal(1^{st}) independently. However, when the initial imperfection is large enough($\delta_{imp} \geq 0.20t$), the high order of the combined buckling modal shapes are stimulated simultaneously and the moment interaction will be activated as well. In order to stimulate the critical imperfection influence, the 1^{st} buckling modal is implemented as the critical initial situation, and the amplitude is controlled at $0.2t$.

3.6.2.3.3 reasonable imperfection

In preceding discussion, the influence by the imperfection amplitude are concluded, and in this paragraph the applicable imperfection is going to be discussed.

Considering the divergence in large imperfection between FE model and the experimental results, only the small and intermediate imperfection extents is going to study. From the practical view, the common estimation on imperfection in real project is about $\delta = \frac{l}{2000}$. The specimen is $l = 10000mm$, which means $\delta_p = \frac{10000}{2000} = 5 = 1.0t, t = 5$. In order to compare with the preceding research on imperfection, the test imperfection $\delta_t = 0.2t = 1.0$is also investigated.

Moreover, in the nonlinear analysis introduction section, for lower imperfection amplitude, both two analysis captures the peak value. However, for the large imperfection amplitude, because there is no clear sign of the snap-back, the ultimate load of the automatically termination is near 15% than the method with the entire loading path.

3.7 Summary and Conclusion

In this chapter, the generation of FE model has been described, and the nonlinear buckling analysis has operated based on the LBA and the imperfection. Moreover, the post-process results have been summarised.

The key parameters in a model generation are the element size and the element aspect ratio. The influence of the previous one is limited by finding a stable eigenvalue with the reducing size, and there is almost no influence by the latter.

Different boundary conditions are tested, it is concluded that the stiff boundary conditions,hinged-hinged and fixed-fixed, is able to concentrate the buckle away from the edge. Therefore, the hinged-hinged restraints are applied Besides, the symmetry boundary conditions are used, and the accuracy of the simplification on the half of the model is validated.

Considering the imperfections in this research is objective to not only stimulate the buckling happen, but also stabilise the buckling dents in the middle. Two types of the imperfection have been investigated. As a complement, two imperfection modification are proposed. It is suggested for the cylinder and the hyperboloid, the first linear buckling modes are suggested as the imperfection.

The imperfection amplitude is discussed about its influence on the ultimate load. For the large imperfection will stimulate the bending interaction in the early stage, the ultimate buckling load is reduced and there are no typical buckling snap-back when the imperfection amplitude is larger than $0.5t$. The relative difference in the nonlinear termination condition, it is also influenced by the imperfection extents. For the limited imperfection amplitude, the auto-termination method is able to track the peak buckling load in the entire path method; for the large imperfection amplitude, since there is no typical buckling peak, the result of the auto-termination method is not accurate enough.

CHAPTER 4

Parameter Study

FEM is a powerful method to solve practical structural problems. When it comes to curved shape, following the changing of the curvatures, a fine mesh is requested. As a result, the number of dofs is large, because the computational cost is proportional to the square of the number of dofs. The expensive computational cost limits engineers' daily work. However, for thin-wall shell structures, buckling failure is critical and the LBA is not able to provide a safe solution. Hence, GNLBA is inevitable. It is estimated that the time to solve a 100,000 dofs shell model with nonlinear buckling analysis with 30 load steps, on a common desktop, may cost nearly 3-4 hours. For this reason, the author proposes a new method, to estimate shell local buckling analysis with the geometry parameters, relying on linear buckling analysis or just only linear analysis.

There are three steps in this chapter. At first, the difference of local buckling analysis and global buckling analysis are discussed. Secondly, based on the GNLBA results, the buckling mechanism is studied. The numerical relation between the buckling phenomenon and the varying geometry parameters are studied in both the global scope and the local scope. In the third part, the related application is extended with the buckling mechanism study. The ultimate stress state are introduced.

4.1 Previous Study and Model Preparation

4.1.1 Previous Research on Shell Buckling

In previous research, the imperfection influence on shell buckling has been studied by Chen [4]. Several types of defects have been discussed, including the specified linear buckling modal shape, the combination of several buckling modal shapes, the Gaussian random imperfection and the periodical buckling waves. It was concluded that the imperfection shape by first buckling modes is a balanced alternative with conservative results and acceptable calculation cost. Moreover, in that paper, the relation between the global reaction force and the geometry parameters (radial ratio) are investigated, in fig 4.1. However, only the specified thickness is studied, in this research the relation will be extended to varied thickness.

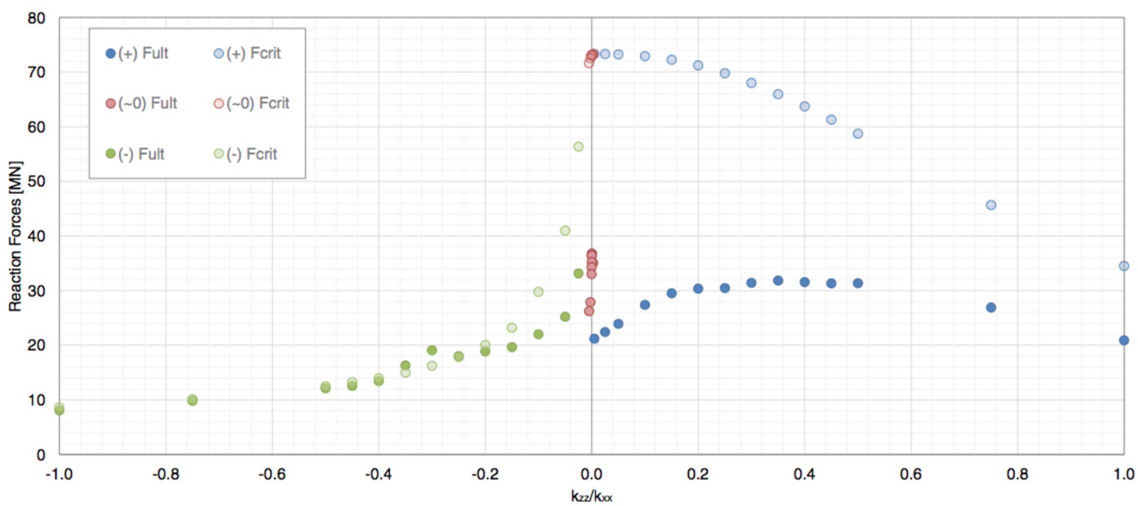

Figure 4.1: Result of the reaction force vs the geometric parameters in Chen's report

The other geometry parameter is the imperfection amplitude δ_{amp}, it has been already studied in Koiter Theory. Koiter Law derives the relation of the imperfection amplitude with the global structure knock-down factor. And the knock-down factor $\frac{\lambda}{\lambda_c}$ depends on the geometry sensitivity parameters,eq 4.1.

$$\lambda = \lambda_c \cdot (1 + a \cdot w + b \cdot w^2 + \cdots) \tag{4.1}$$

Since, the δ_{amp} influence has already been explored, and it will not be a key parameter in this research. Just as a complementary, the variation on δ_{amp} is tested to see the influence of imperfection on the internal force.

It is also an ambition to shape the formula of the internal force with local buckles. For the nearly cylinder hyperbolic shape, there are only two to three buckling buckles in height with slim width, and between the dents there is some low-stress zone as a tie to resist the deformation happen. Based on this, Von Karman has made an assumption that there could be a simulation by the shell buckling with the column buckling with serious nonlinear intermediate supports. Moreover, all the influence of the hoop force is taken into the nonlinear material property of the support. Hence, in this section, the simulated column buckling behaviour is expected.

4.1.2 Standard Model Description

Before the parametric study, it is necessary to decide a standard shape of the specimen, which is used to be compared with the other variations. For it is meaningless to make the comparison with two distinguished model on structural behaviour, the general geometric parameters like the edge radius and the height are kept constant, or only the small range variations are tested. The extreme slender model is avoided, it is expected to perform the Euler column buckling shape. In standard model, Young's modulus is $E = 210,000MPa$ and the Poisson's ratio is $\nu = 0.3$.

The standard specimen is 10000 mm in height, the radius of the edge ring is 2500 mm, the standard vertical radius is 25000 mm, and the initial thickness is 5 mm, in fig 4.2. The hinged boundaries restrain both edges. The basic model shape is generated from the water tower, and the local zone in the middle of the model is studied.

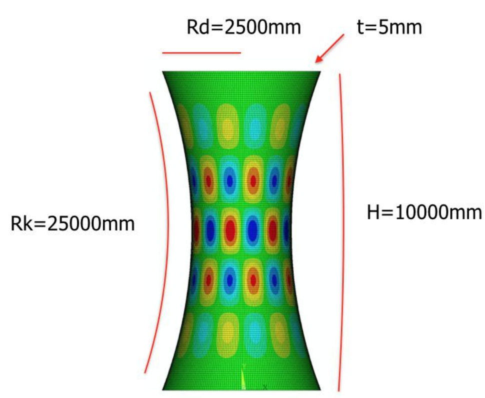

Figure 4.2: Standard model shape

It is written that the variation of the vertical radius is restricted by the physical feasibility. With the specific height and edge radius, the minimum R_k is 8000 mm. For the smaller value, although it is possible to a mathematical graph, the cantilever effect is going to be intensified, and the buckles are concentrated on the edge part. Regarding, the R_k is limited from 8000 mm to 3,500,000 mm. The maximum limitation, which almost reaches the cylinder shape, will be discussed later.

The vertical radius changes the specimens from the hyperboloid to the nearly-cylinder, and the entire range is split to five gradual groups, each group is uniformly divided to 10 models,table 4.1. With different test parameters, there are 14 series, in total 700 models are tested. The Appendix.D lists the geometric conditions of the tested specimens.

Table 4.1: Test group with respective vertical radius (R_k)

Group 1	8,000mm-12,000mm
Group 2	12,000mm-33,000mm
Group 3	33,000mm-60,000mm
Group 4	60,000mm-330,000mm
Group 5	330,000mm-3,500,000mm
note:	each group distributes with 10 model samples

4.2 Database Introduction

The database of the GNLBA result covers over 700 specimens in hyperboloid model with different geometry parameters. The perfect FE model is generated as the previous chapter. Based on the imperfection study, the first buckling modal shape is applied; hence, only the first buckling shape will be activated. The element results of GNLBA is collected into the database.

The database is separated into two parts, about the input parameters part, and the GNLBA results part. The input parameters includes the geometry parameters, like radius of the edge ring(R_b), the vertical radius(R_k), the middle radius(R_m), the thickness(t) and the imperfection amplitude(δ_{amp}).

The selected element output results are based on the radial deformation. Both of the largest radial deformation are monitored. For the outward direction, it is the maximum value in positive and for the inward direction, it is the minimum value in negative. In post-process, the script is able to rank the radial deformation and collects the results of the elements with largest radial deformation. Depending the buckles position in vertical, their radius in horizontal is varying with the height. For this reason, the horizontal radius(R_{in}, R_{out}) is recorded as geometry information. Besides the local geometry of the dents(R_k, R_{in}), the internal force results are also exported, containing the membrane stress in horizontal direction(n_{xx}) and vertical direction(n_{yy}), and the moment stress in moment stress in horizontal direction(m_{xx}) and vertical direction(m_{yy}).

Table 4.2: Database information

	Input data	**Result data**
Geometry	R_k,R_d,R_m,t,δ_{amp}	R_{in},R_{out}
Structural behaviour		D,F,P_{in},P_{out}
Internal force		n_{xx-in},n_{yy-in},m_{xx-in},m_{yy-in} n_{xx-out},n_{yy-out},m_{xx-out},m_{yy-out}

4.3 Buckle Study

To investigate the geometric relation between the buckle dimension, the aspect ratio $\frac{\lambda_{yy}}{\lambda_{xx}}$, with the changing geometry.

To keep the models comparable with each other, the general parameters as the height H and edge radius R_d are kept constant, only the vertical radius R_k is changed. With the geometric restraint, the changing R_k influences the middle radius R_m as well, It changes the model from the hyperboloid to the nearly cylinder shape. In fig **??**, in x-axis, the radius ratio is defined as the ratio of the middle radius to the vertical radius $\frac{R_m}{R_k}$. In y-axis, the aspect ratio of the buckle $\frac{\lambda_{yy}}{\lambda_{xx}}$ is calculated to describe the buckle shape. In fig 4.3, the relation is shown between the $\frac{R_m}{R_k}$ and $\frac{\lambda_{yy}}{\lambda_{xx}}$. To classify the buckle distribution, the abbreviations like $R18 - H4$ are used. It indicates that there are 18 buckles in the radial direction and 4 buckles in the height direction.

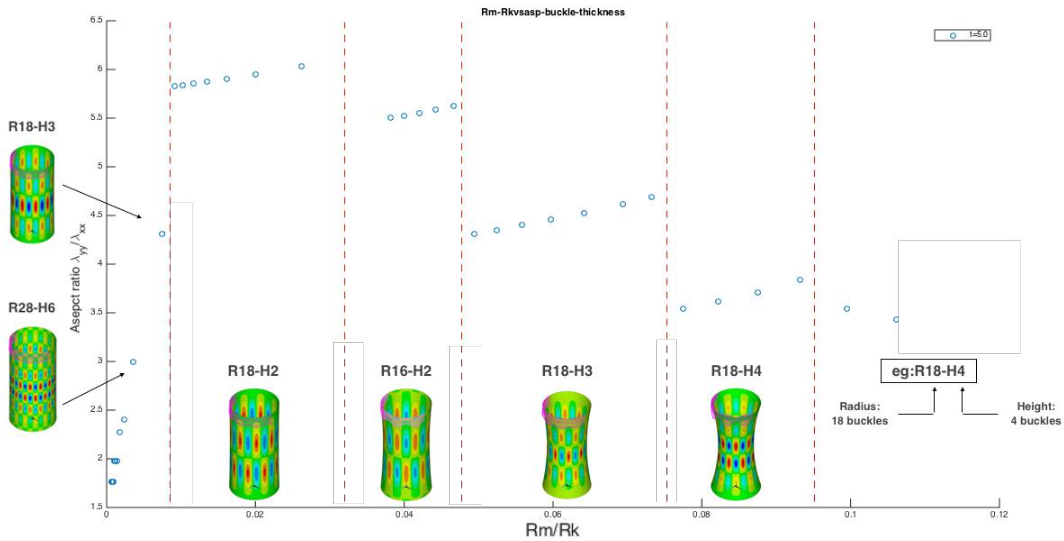

Figure 4.3: Aspect ratio of the buckles with varying geometries

It is clear that the aspect ratio for different geometries is separated by the different buckle distributions. With the same buckle distribution(fig 4.4.b-ii,iii), the geometries influence is continuous; while, there is always a jump on buckle aspect ratio(fig 4.4b-ii,iii), between a change of the buckle distribution. It is because the height of the specimen is constant, from fig 4.4b-iii to fig 4.4b-ii the increasing R_k reduces the surface length in the vertical direction, from solid to dash line, in fig 4.4.a. As a consequence, if the buckle distribution is identical, the decreasing vertical surface length will squeeze the vertical wavelength λ_{yy} as well. Until the double buckles distribution is stimulated(fig 4.4.b-i), the buckling wavelength is increased. In the radial direction, the increment of the equator provides a large distance for the horizontal buckles to develop.

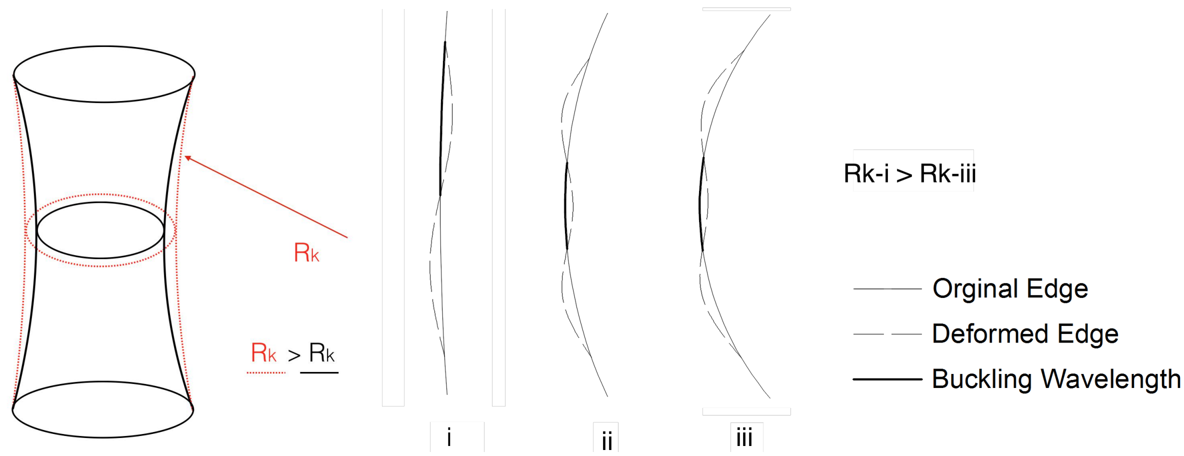

(a) increasing vertical radius (b) edge deformation

Figure 4.4: Model with different vertical radius

It is concluded that for identical buckle distributions, the increasing of R_k decreases the aspect ratio slightly. But in general, changing of buckle distribution, caused by the increasing vertical radius, will make the buckle slender. When the aspect ratio almost reaches between 4-6, strip or column behaviour is expected. The further local study is presented in next section.

4.4 Global Buckling Analysis and Local Buckling Analysis

Cylinders and hyperboloids buckle in different patterns, it causes the internal force performance in different ways. Since the global buckling analysis is influenced by the buckling pattern as well, it is aimed to investigate the relation between the global buckling analysis and the local buckling analysis.

In cylinders, buckles have a square shape, and both of the internal force are stimulated with the increasing loading. In hyperboloid, buckles shape are slenderer, and the vertical membrane force is dominant to the horizontal. In detail, the development of the internal force at the buckling point shows that only the vertical membrane force is increased clearly with the loading process. The critical vertical force and the slender buckle geometry indicate column behaviour. Its behaviour is comparable to a curved strip. To decouple the interaction of the membrane force, only the slender shape dents are investigated.

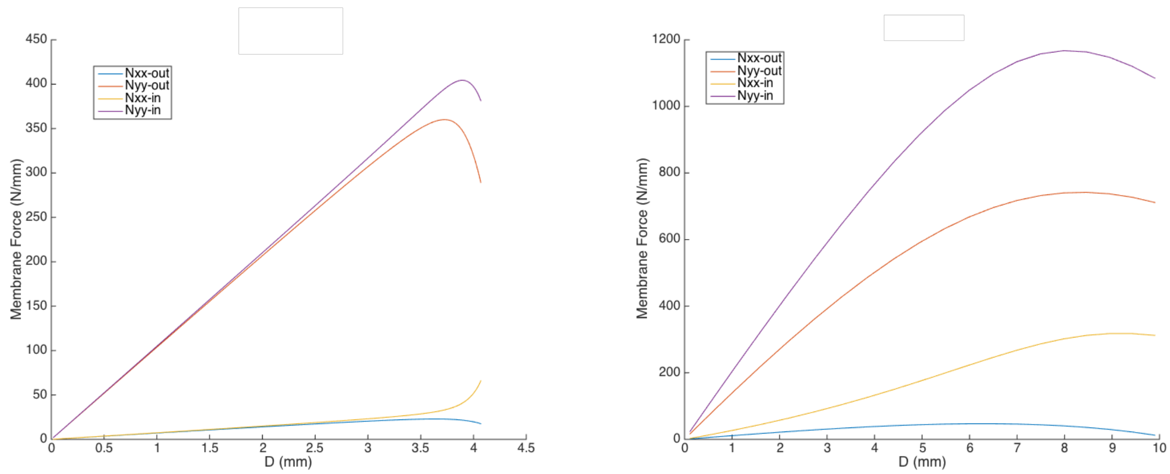

(a) hyperboloid (b) cylinder

Figure 4.5: Membrane force in cylinder and hyperboloid (LP-118-5/LP-207-5: Cylinder and Hyperboloid, Rd=2500mm, Rk=20000mm, H=10000mm, t=5mm, E=210000MPa, ν=0.3, 1^{st}modal imperfection)

In the slender shape distribution, only two to three dents in a vertical direction, we could expect the column behaviour in global analysis as well. The horizontal membrane force, hoop force, plays a role of the restraints, which are assumed as a nonlinear property [16]. When the local dents are buckling, the global structure are stimulated to buckle. In this section, how the local buckles will influence the global analysis is investigated.

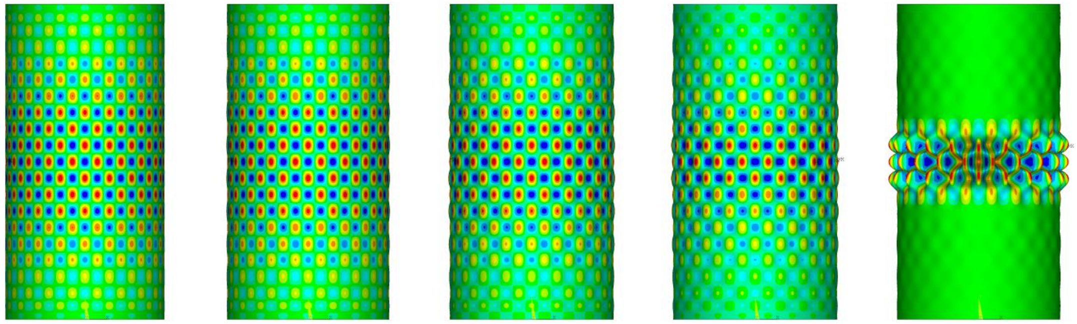

(a) 25% (b) 75% (c) 95% (d) 100% (e) postbuckling

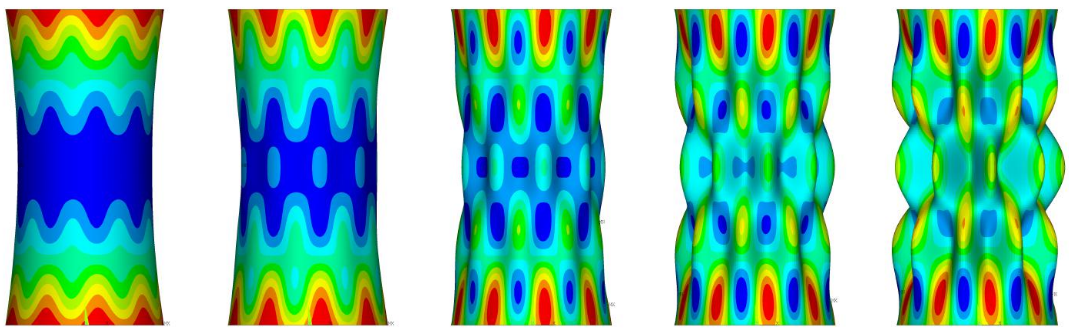

(f) 25% (g) 75% (h) 95% (i) 100% (j) postbuckling

Figure 4.6: n_{yy} distribution in cylinder and hyperboloid (with load status) (LP-118-5/LP-213-5: Cylinder and Hyperboloid, Rd=2500mm, Rk=20000mm, H=10000mm, t=5mm, E=210000MPa, ν=0.3, 1^{st}modal imperfection)

Note: The contour is with relative value of each model.

Fig 4.5 shows the comparison between cylinders and hyperboloids on internal force behaviour under the axial compression condition. For hyperboloid, before the buckling occurrence, the load is carried by the vertical membrane force(n_{yy}). With the imposed deformation increase, the total reaction rises at the same time. Until reaching the buckling point, the reaction force drop in a sudden, which indicate the structure loses its resistance capacity. From the contour plot of the radial deformation, in fig 4.6, we can observe that the local imperfection dents deformation aggregate in concentration.

Moreover, before the global buckling occurs, the deformation in local dents has started to increase dramatically. In fig 4.7(a) and (b), the plot of the relation between both radial deformation and vertical deformation versus vertical reaction force, which describes the buckling occurrence in global and local scope.

Comparing both figures in fig 4.7, the linear part of the radial deformation curve(fig 4.7(b)) is terminated at an earlier stage. It indicates that the radial deformation in local buckling analysis is a more sensitive indication than the global buckling analysis. In practice, the local buckling analysis is defined by the perturbation deformation and including the plastic deformation as well. However, this thesis is focused on the elastic and the membrane forces are investigated, the end of the linear part is defined as the termination of the local buckling analysis.

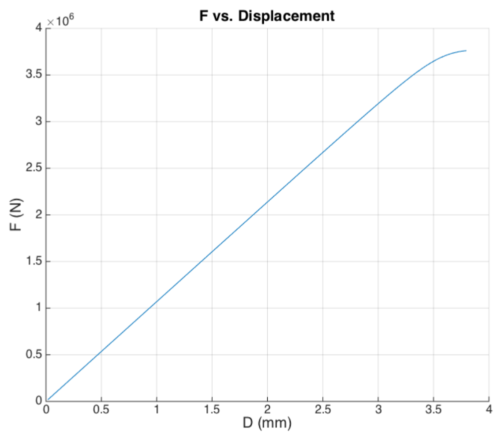

(a) global buckling analysis

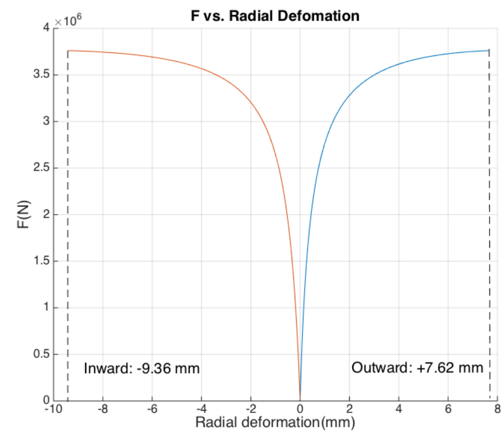

(b) local buckling analysis

Figure 4.7: Global buckling analysis(vertical deformation) and local buckling analysis(local radial deformation) (LP-118-5/LP-213-5: Cylinder and Hyperboloid, Rd=2500mm, Rk=20000mm, H=10000mm, t=5mm, E=210000MPa, ν=0.3, 1^{st}modal imperfection)

To specify the most critical internal force component in global behaviour, all the internal force are discussed together, including the membrane force and the moment force in both of the vertical(y-y) and the horizontal(x-x) directions, at both the inward and the outward dents. The fig 4.8 plots the imposed displacement with the these internal force respectively. To make them comparable, the normalized valued are plotted.

Similar as the F-D curves, after the peak point, there are the degradation parts in some internal force curves, which clearly shows the buckling occurrence and its development in a local site. Notes that, there are two typical trends in the local internal force. (1) With the increasing imposed displacement, some of the internal force, like n_{yy-in} and n_{yy-out}, they start decrease, just after they approach the peak point, which is the indication of the loss of the resistance. These components are classified as the resistance components of the buckling. (2) On the other hand, like

n_{xx-in} and moment internal force, they increase slowly at first, and at some point, the slope increase dramatically. Finally, their trends are toward infinite. From the physical meaning, a small load increment will cause it to infinite results, these components are classified as the consequence components of the buckling.

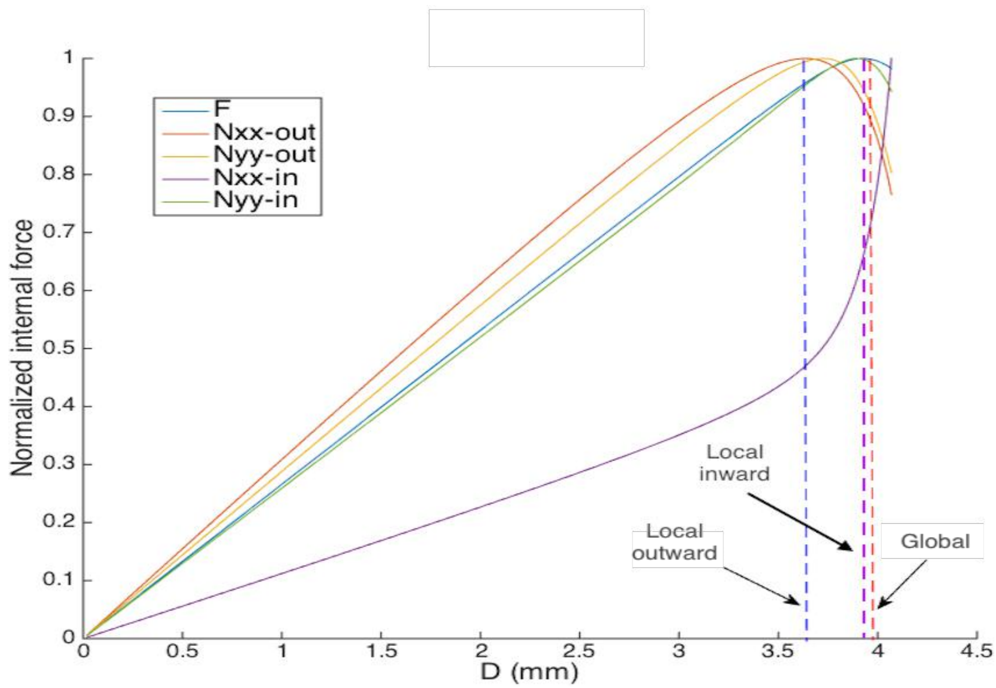

(a) Membrane

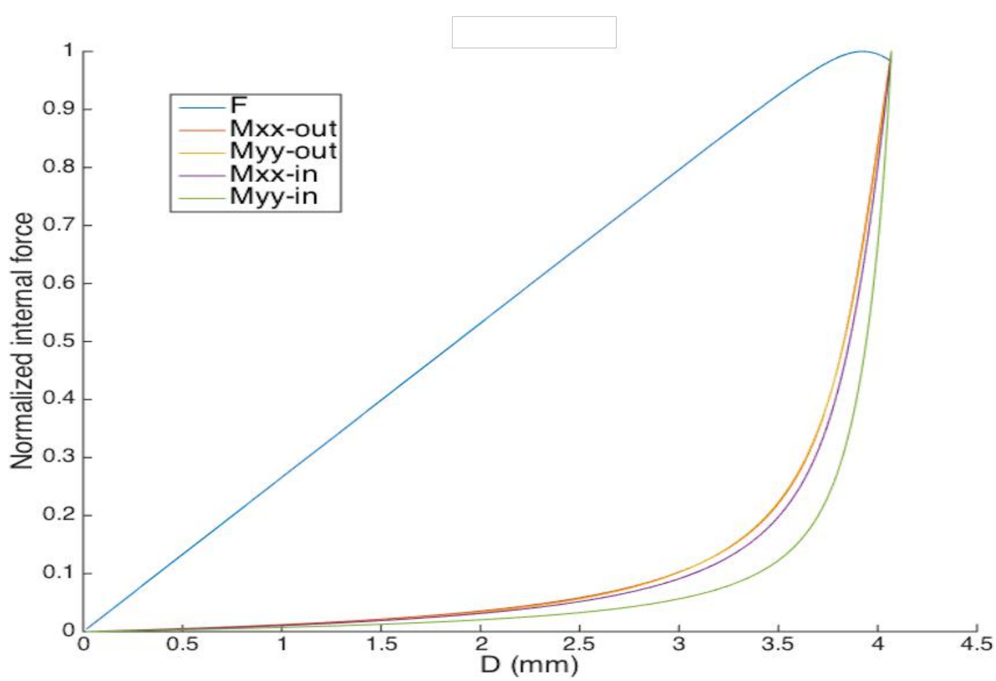

(b) Moment

Figure 4.8: Normalized internal component (LP-213-5: Hyperboloid, Rd=2500mm, Rk=20000mm, H=10000mm, t=5mm, E=210000MPa, ν=0.3, 1^{st}modal imperfection, $\delta_{imp} = 0.2t$)

There are three distinctions between the inward buckle and the outward buckle. Firstly, in fig 4.7, the stiffness of the inwards buckle is larger than the outward buckles. Secondly, the inward buckle deforms much more than the outward buckle. The large stiffness component always resists the more load. Thirdly, the fig 4.8(a) shows the vertical internal force in the inward buckle n_{yy-in} is much closer to global reaction force buckling. Checking the distribution of the third principal stress in fig 4.9, it also indicates the inward buckles resisting the most of the load. Hence, n_{yy-in} is the focus on the latter study.

It is concluded that the inward dents are the critical zones of the hyperboloid under the axial compression load, and the outward dents are trying to escape the load resistance. Besides its early local buckling is also a good alarm of the global buckling occurrence.

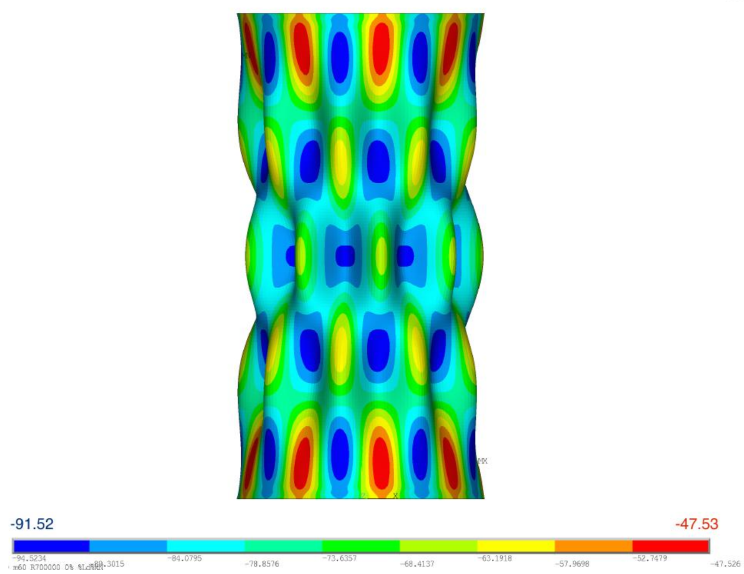

Figure 4.9: Third principal stress distribution in a hyperboloid at the moment of buckling occurrence state (LP-213-5: Hyperboloid, Rd=2500mm, Rk=20000mm, H=10000mm, t=5mm, E=210000MPa, ν=0.3, 1^{st}modal imperfection, $\delta_{imp} = 0.2t$)

We have already observed that the n_{yy-in} is very close to the global reaction force F buckling in specified geometry. To investigate how the n_{yy-in} buckling stimulates F buckling, it is intended to study the difference between the n_{yy-in} and F with different geometries.

Changing the R_k to generate different models, the peak value of the n_{yy-in} and F are captured and their correspondent value of imposed displacement are recorded. The series of imposed displacement at the local buckling points are plotted with model geometric parameters respectively in fig 4.10, getting the trends of the local buckling analysis and the global buckling analysis.

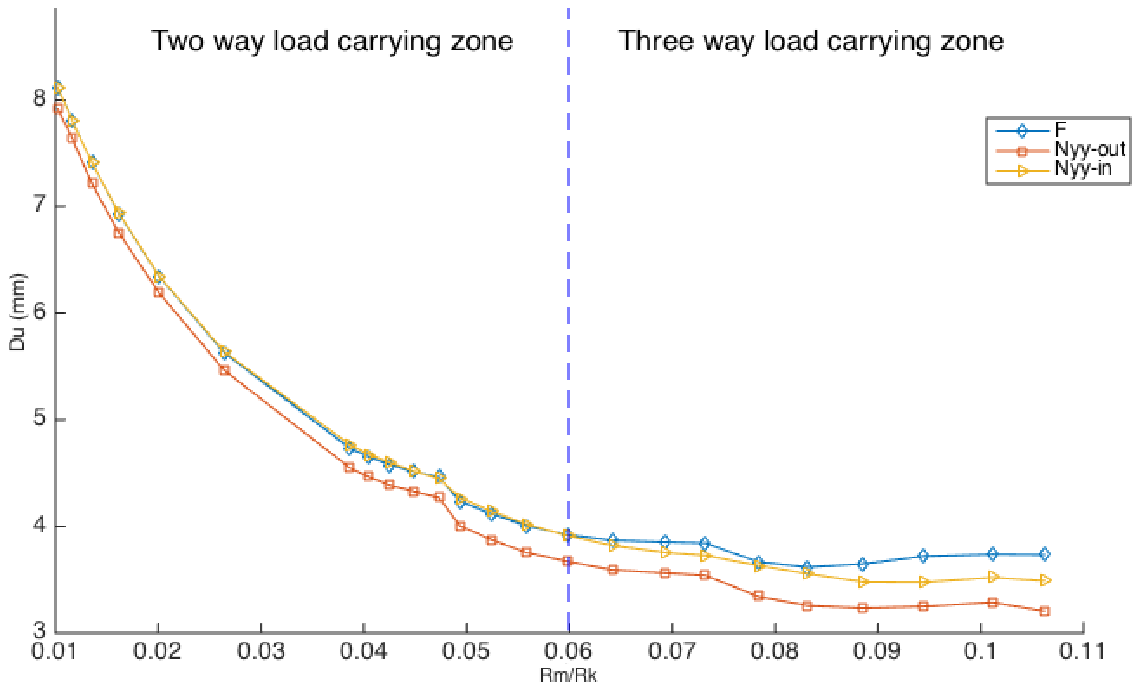

Figure 4.10: Imposed displacement $D_u(mm)$ at the peaks of different internal force component (Test No.1 : Hyperboloid, Rd=2500mm, Rk=8000mm-3,500,000mm, H=10000mm, t=5mm, E=210000MPa, ν=0.3, 1^{st}modal imperfection, $\delta_{imp} = 0.2t$)

For the outward component, the correspondent imposed displacements are always earlier than global buckling occurrence. For the inward buckles behaviour, when the geometry approaches the cylinder, the local n_{yy} at the inward dents buckle almost simultaneously with the global reaction force. With the increasing radius ratio, the geometries are changing into hyperboloid shape, and the divergence happens. The membrane force in a vertical direction n_{yy-in} escapes from resisting the buckling load and starts to buckle before the global reaction force as well.

The divergence separates the geometries into two parts: two-way load carrying zone and three-way load carrying zone. It is clear that in the two-way load carrying zone, the inward buckle and the outward buckle are the only load carrying components, just after the local components failure the total reaction force occur. In the three-way load carrying zone, the other component provides the additional load carrying way to resist the buckling load, and increases the redundant buckling capacity.

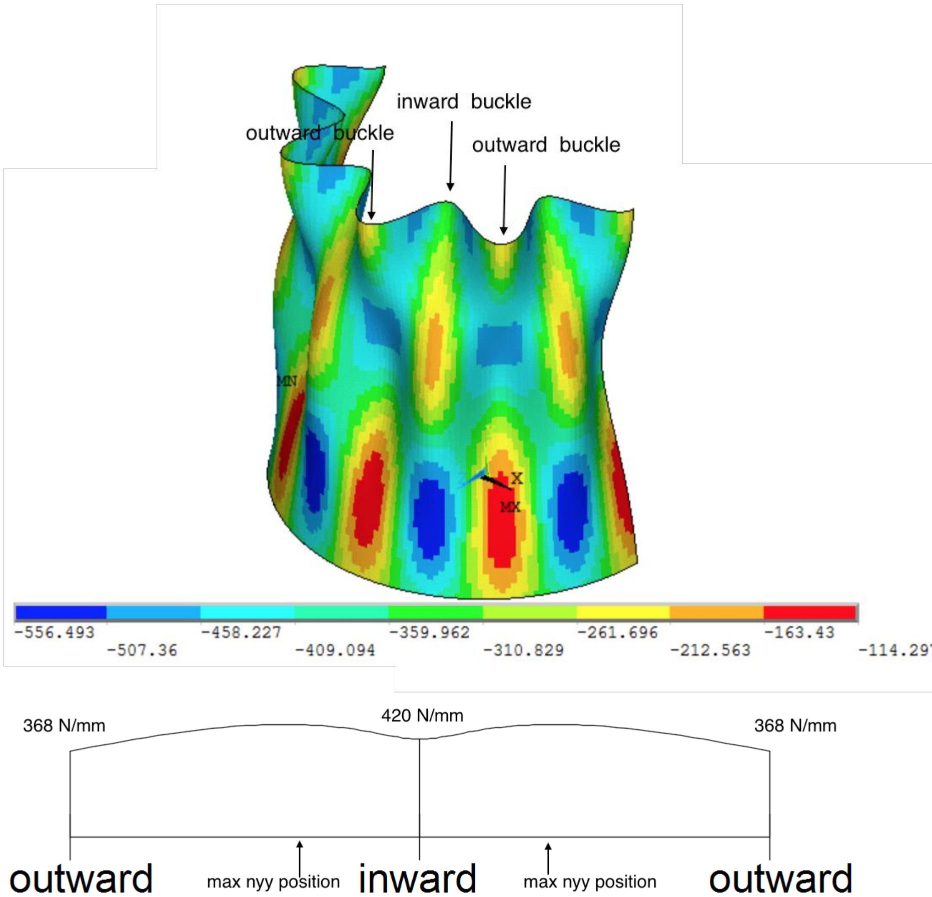

Figure 4.11: Non-averaged element result on vertical membrane force distribution n_{yy} in local scope (LP-214-1: Hyperboloid, Rd=2500mm, Rk=33000mm, H=10000mm, t=5mm, E=210000MPa, ν=0.3, 1^{st}modal imperfection, $\delta_{imp} = 0.2t$)

The observation on vertical membrane distribution (fig 4.11) after the local component failure shows that the peak membrane force moves from the inward buckle to the in-between area. Moreover, with the increasing imposed displacement, the n_{yy} concentrates into the in-between area. Hence, the in-between area provides the additional load carrying way.

4.5 Global Buckling Study

In this section, the relation between ultimate force in global buckling analysis and the geometric parameters are analysed. The vertical radius R_k is selected as the main geometric variable in this chapter, and the influence of the varying thickness are studied as well. To study the geometry influence on the ultimate force, the height and the edge radius of the specimen are kept constant at first, $H_0 = 10000$ and $R_b = 2500$. Based on the imperfection study, the extent of the imperfection is restricted to $\delta_{amp} = 0.2t$.

Firstly, with the specified thickness, the trend of the vertical radius will be discussed. The global buckling behaviour is separated into two parts, and both of them are investigated. Secondly, based on the data of the test results, the numerical regression is proceeded, and the numerical formula reveals the influence of the vertical curvature and the thickness on the ultimate force in global buckling analysis. The relation about the ultimate reaction force $Fu(\frac{Rm}{Rk}, t)$ is generated. At last, the additional test data are used to verify the regression result.

4.5.1 Global Buckling Graph Introduction

The ratio $\frac{R_m}{R_k}$ is selected as the geometric influence parameter and the results of the ultimate reaction force at the global buckling analysis points are collected. The scatters are grouped with varying thickness in fig 4.12.

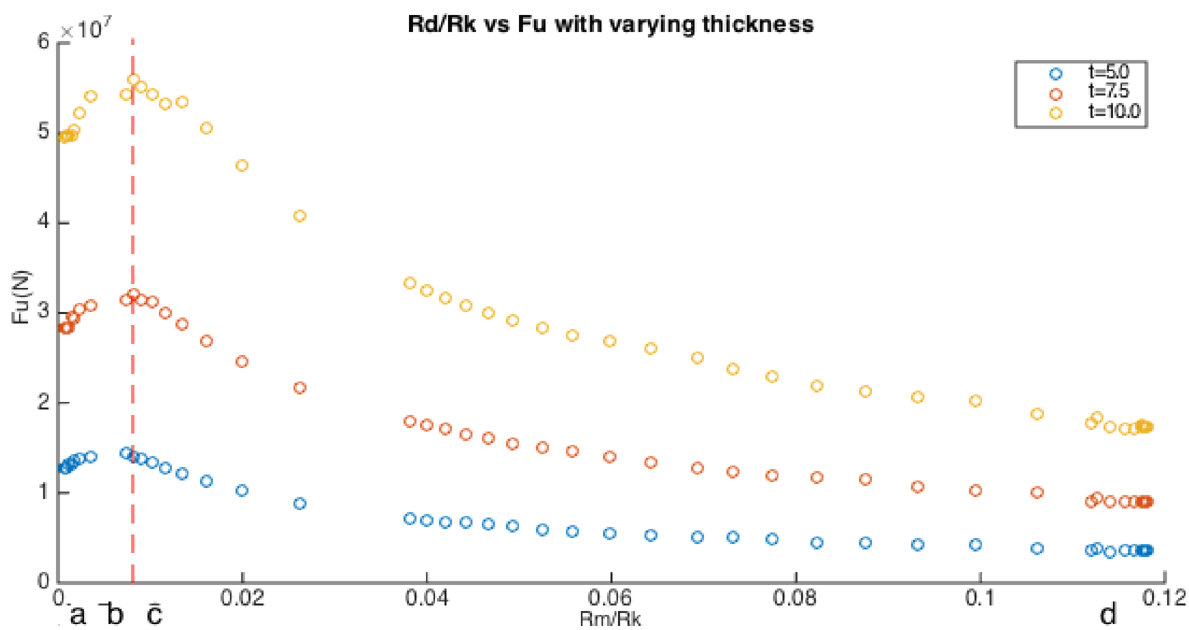

Figure 4.12: Geometric influence on ultimate reaction force (Test No.1,4,6 : Hyperboloid, Rd=2500mm, Rk=8000mm-3,500,000mm, H=10000mm, t=5mm,7.5mm,10mm, E=210000MPa, ν=0.3, 1^{st}modal imperfection, $\delta_{imp} = 0.2t$)

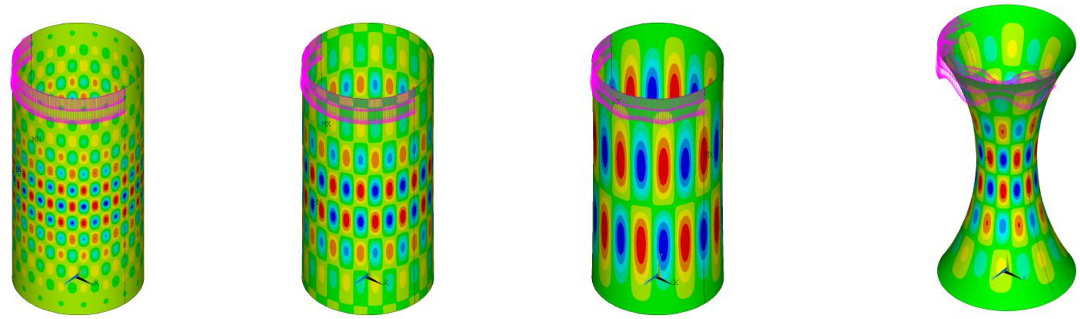

(a) $\frac{R_m}{R_k}$=0.001 (b) $\frac{R_m}{R_k}$=0.005 (c) $\frac{R_m}{R_k}$=0.008 (d) $\frac{R_m}{R_k}$=0.100

Figure 4.13: Curvature indication

It is evident that when the specimen is close to the cylindrical shape, there is a drop in the reaction force. The exact cylinder is not the maximum buckling load capacity shape, but the largest load resistance is just near the exact cylindrical shape. The transition point is extremely close to the cylindrical geometry, which is labelled in red dash line. In the check of the linear buckling pattern, the number of the buckling vertical wave decreases from 6 to 2 (in 4.12), with the decreasing radius ratio; on the other hand, when it overcomes the transition point(fig 4.13(a)(b)), the wave number increases dramatically and is close to the exact cylinder buckling pattern.

To show the relation near the transition point, a logarithmic axes is applied (fig 4.14). Note that the red dash line also presents the correspondent transition points in the logarithmic axes.

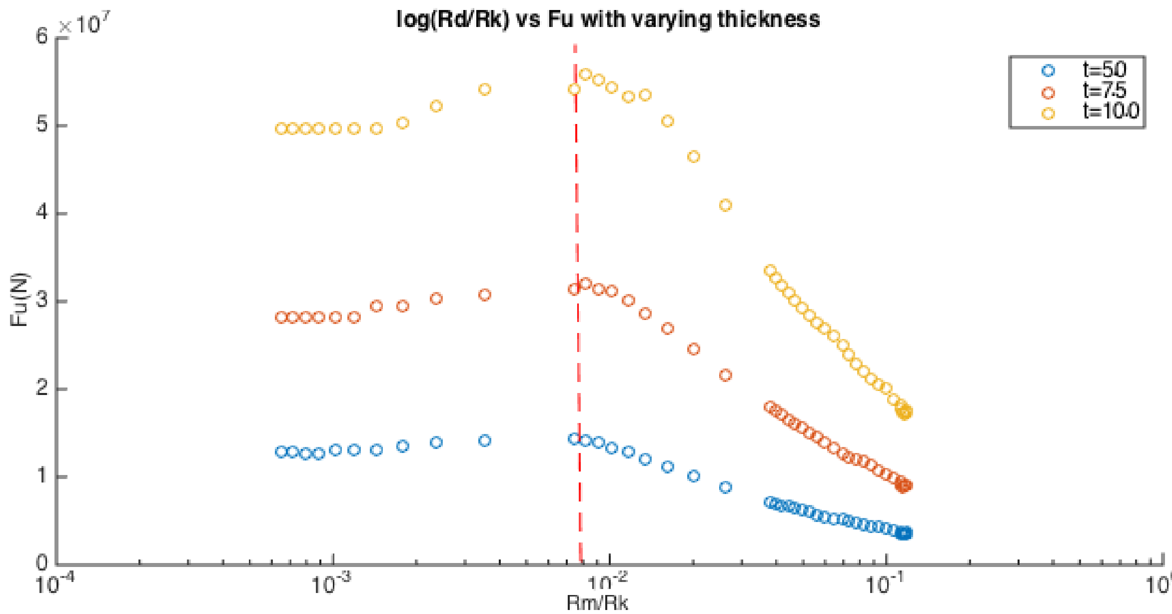

Figure 4.14: Geometric influence on ultimate reaction force (logarithmic scale) (Test No.1,4,6 : Hyperboloid, Rd=2500mm, Rk=8000mm-3,500,000mm, H=10000mm, t=5mm,7.5mm,10mm, E=210000MPa, ν=0.3, 1^{st}modal imperfection, $\delta_{imp} = 0.2t$)

Hyperbolic side In logarithmic axes, the influence by the geometric parameters is much more clear. In the hyperbolic shape side, with the constant thickness, it is the linear relation between the $\log(\frac{R_m}{R_k})$ and the ultimate force.

Nearly Cylindrical side When the $\frac{R_m}{R_k}$ overcomes the transition point, the geometric parameter influence is in stepped form, and the ultimate force reduces with the decreasing curvatures ratio, which means it close to the cylinder. It is notes that because of the logarithmic axes, the distance between the perfect cylinder and the transition point has been zoomed in, in reality it is very close to each other.

Transition point It is evident that the varying thickness does not shift the transition point at all, it keeps stable at $\frac{R_m}{R_k} = 8 * 10^{-3}$. The following section will investigate the robust of transition point with the influence by the other geometric parameters.

All of these three points are discussed following.

4.5.2 Hyperbolic side

As previously discussed, the relation between the curvature ratio and the ultimate force in the hyperbolic side is obeyed the linear relation in the logarithmic axes. The left side of the hyperbolic range is the transition points and the right side is ended with the extremely thin hyperboloid. To avoid the small discrepancy in both ends, the following formula study is focused on the main part of this range($0.01 < \frac{R_m}{R_k} < 0.1$). The results are grouped by the respective thickness. The curve fitting is applied to investigate their relation.

The general workflow between the geometric parameters the reaction is in fig 4.15. Firstly, with the specified thickness t_1 (secondary independent), the relation between the dependent variable(eg:F_u) and the main independent variable(eg:$\frac{R_m}{R_k}$) is solved by the 1^{st} curve fitting trial. Based on the estimated formula shape, the correspondent coefficient $A(t_1)$ and $B(t_1)$ are recorded. Secondly, the data with varying thickness $(t_2, t_3, ...)$ are iterated with the last step. The series coefficients$(A(t_2), A(t_3), ...; B(t_2), B(t_3)...)$ are recorded with respective thickness. The graph of coefficients tables shows the relation between the coefficients(A, B) and the thickness(t). The 2^{nd} curve fitting trial is applied to solve the formula of $A(t)$ and $B(t)$. In these thesis, the coefficient relation$(A(t), B(t))$ is restrained to the linear relation. Finally, combining the solved $A(t)$ and $B(t)$ with the estimated formula, we could generate a general formula, like $F(\frac{R_m}{R_k}, t)$.

There is a detailed numerical analysis example in the Appendix.

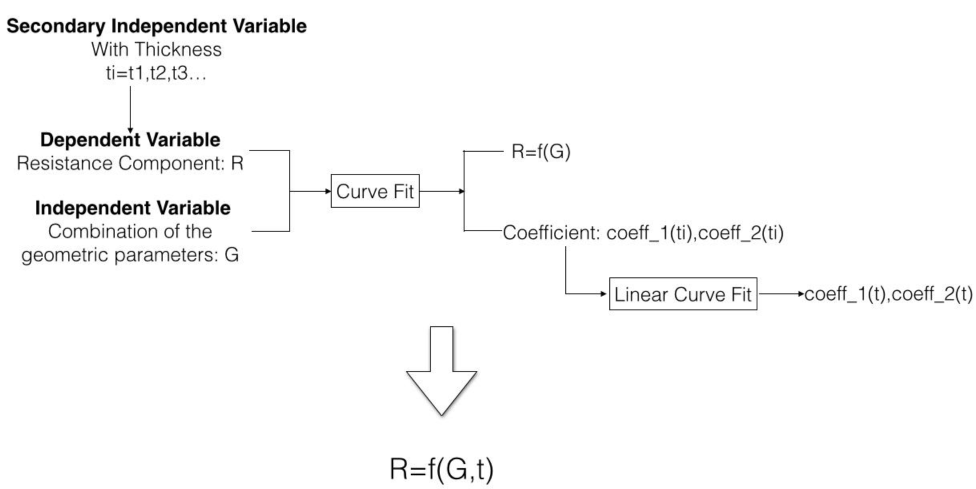

Figure 4.15: Work flow of the curve fitting

In fig 4.14, the varying thickness changes the slope and the intersection. Hence, we could estimate the logarithmic relation between the $\frac{R_m}{R_k}$ and the ultimate force F_u, and the coefficient depends on the thickness t. The formula has the following format eq A.1.

$$F_u = A(t) \times log(\frac{R_m}{R_k}) + B(t) \tag{4.2}$$

Following the curve fitting procedure, with thickness $t_i = 5, 6, 7.5, 10$, the solved correspondent coefficients $A(t_i)$ and $B(t_i)$ are listed in the following table 4.3.

Table 4.3: Coefficients table with thickness

t	**A** $\times 10^6$N	(95% confidence bounds)	**B**$\times 10^6$N	(95% confidence bounds)
5	-4.154	(-4.347, -3.966)	-6.026	(-6.652, -5.401)
6	-6.021	(-6.298, -5.743)	-8.369	(-9.265, -7.473)
7.5	-9.425	(-9.719, -9.131)	-12.33	(-13.281, -11.380)
10	-16.391	(-17.082, -15.701)	-19.212	(-21.424, -16.991)

Based on the solved coefficients, the second linear curve fitting is applied. The relation between A,B with t are calculated.

$$\begin{cases} A(t) = a_1 \cdot t + a_2 \\ B(t) = b_1 \cdot t + b_2 \end{cases} \tag{4.3}$$

Table 4.4: Coefficients $A(t)$ with different thickness

Coff-A	$a_1 \times 10^6$N/mm	(95% confidence bounds)	$a_2 \times 10^6$N	(95% confidence bounds)
	-2.471	(-3.063, -1.879)	8.609	(4.245, 12.971)

Table 4.5: Coefficients $B(t)$ with different thickness

Coff-B	$b_1 \times 10^6$N/mm	(95% confidence bounds)	$b_2 \times 10^6$N	(95% confidence bounds)
	-2.652	(-2.881, -2.423)	7.410	(5.723, 9.096)

For the correspondent coefficients of the varying thickness, the second curve fitting trial is applied. The linear formula is estimated, and the results are plotted in the following, fig 4.16

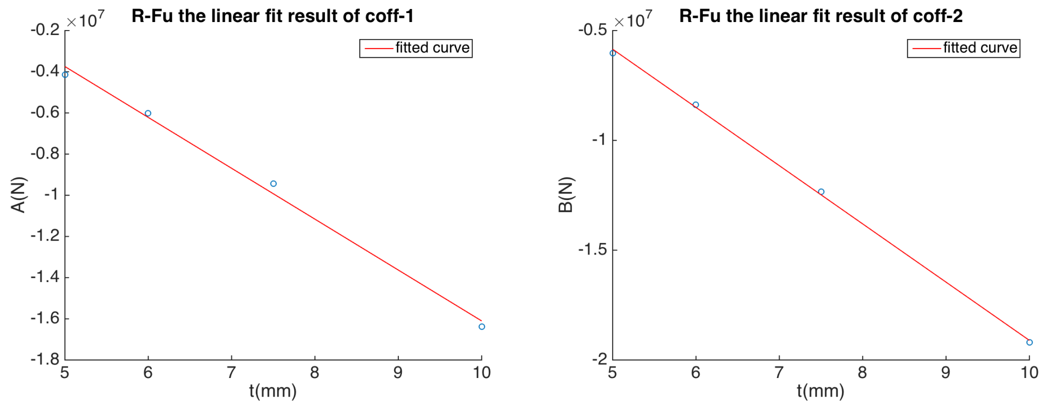

Figure 4.16: Curve fitting results on coefficients $A(t)$ and $B(t)$

The formulas of the coefficients and the thickness are concluded as eq 4.4

$$\begin{cases} A(t) = (-2.471 \cdot t + 8.609) \times 10^6 \\ B(t) = (-2.652 \cdot t + 7.410) \times 10^6 \end{cases} \tag{4.4}$$

Finally, we could conclude the varying thickness into the relation between the ultimate force Fu and the combination of the geometric parameters $\frac{R_m}{R_k}$, into $F_u(\frac{R_m}{R_k}, t)$

$$\begin{aligned} F_u(\frac{R_m}{R_k}, t) &= A(t) \cdot \log(\frac{R_m}{R_k}) + B(t) \\ &= (-2.471 \cdot t + 8.609) \times 10^6 \cdot \log(\frac{R_m}{R_k}) + (-2.652 \cdot t + 7.410) \times 10^6 \end{aligned} \tag{4.5}$$

Moreover, in order to verify the equation, two more group of the result, $t = 5.5$ and $t = 9.0$, are included. The verification groups are not imported in the curve fitting process. Therefore, their results from the nonlinear analysis are able to use to check the accuracy of the curve fitting result. In these groups, only the thickness are changed, and the other conditions are kept same.

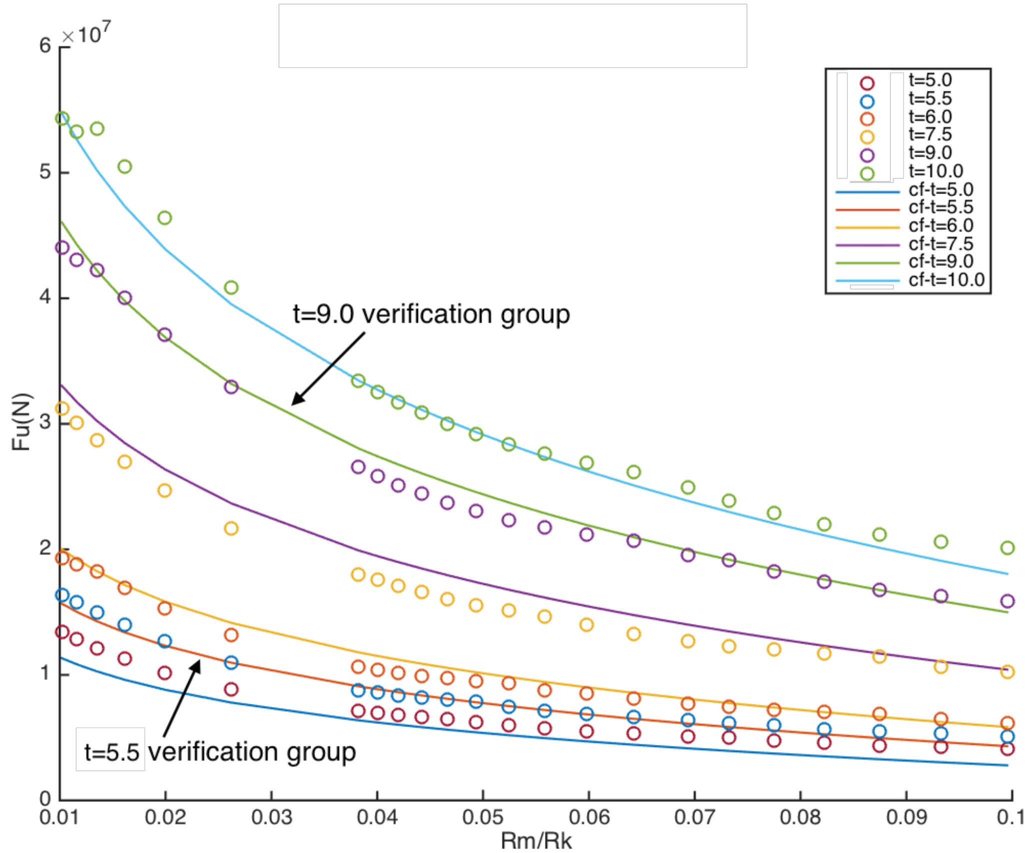

Figure 4.17: Curve fitting results on Fu vs. $\frac{R_m}{R_k}$ (Test No.1-6 : Hyperboloid, Rd=2500mm, Rk=8000mm-3,500,000mm, H=10000mm, t=5mm-10mm, E=210000MPa, ν=0.3, 1^{st}modal imperfection, $\delta_{imp} = 0.2t$)

In fig 4.17, the series of colour curves are the results of the curve fitting, and the scatter dots are the correspondent NLBA results. The curve fitting results have successfully described the NLBA results. However, there are still small discrepancy in the low thickness. If we zoom in detail, it is observed that their curve fitting results share the similar changing trends with the test dots, but just in a lower offset. It is the similar effect of the imperfection amplitude in fig 4.18. In the test assumption, all the test conditions are controlled, except the variable thickness. But considering the imperfection amplitude is defined by the ratio of the thickness,$\delta_{amp} = 0.2t$, actually the relative definition on imperfection description is the suspected discrepancy reason. Besides, the linear assumption on the coefficients is a simplified method, the error could also be induced by the residuals in linear curve fitting.

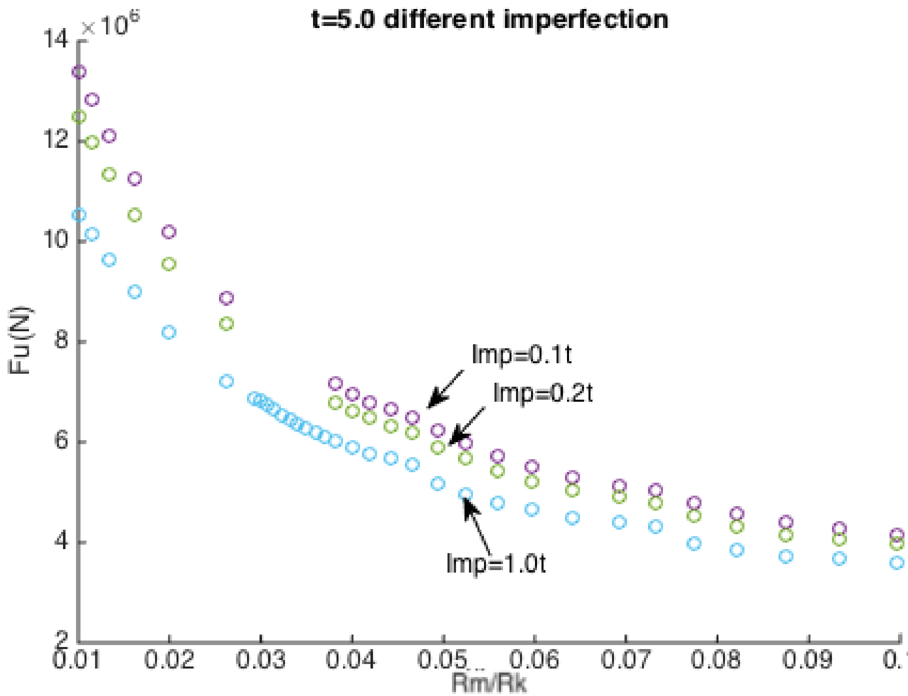

Figure 4.18: Constant thickness with varying imperfection amplitude (Hyperboloid, Rd=2500mm, Rk=8000mm-3,500,000mm, H=10000mm, t=5mm-10mm, E=210000MPa, ν=0.3, 1^{st}modal imperfection, $\delta_{imp} = 0.1t, 0.2t, 1.0t$)

4.5.3 Near cylindrical Side

In fig 4.19, it is the left part of the previous curves(fig 4.14), the geometry are closed to cylindrical shapes. When it has overcome the transition point, The specimens behaviours are totally changed. Different with the hyperboloid shape, the decreasing radius ratio reduces the ultimate reaction force, and the peak buckling load is on the geometry at the transition point. Moreover, with the decreasing radius ratio, the slope of the radius influence is reduced. In the extremely low radius ratio range, the dots develop horizontally with the changing of geometries, it indicates that the geometric influence is eliminated. When it just passes the transition point, the ultimate force is still influenced, but it behaves into steps like later. The changing geometric parameters have no continuous influence on the ultimate loads, but the ultimate loads jumps in some specific value. Since the linear buckling behaviour is closing to the cylinder, the higher order of the cylinder buckling patter is checked.

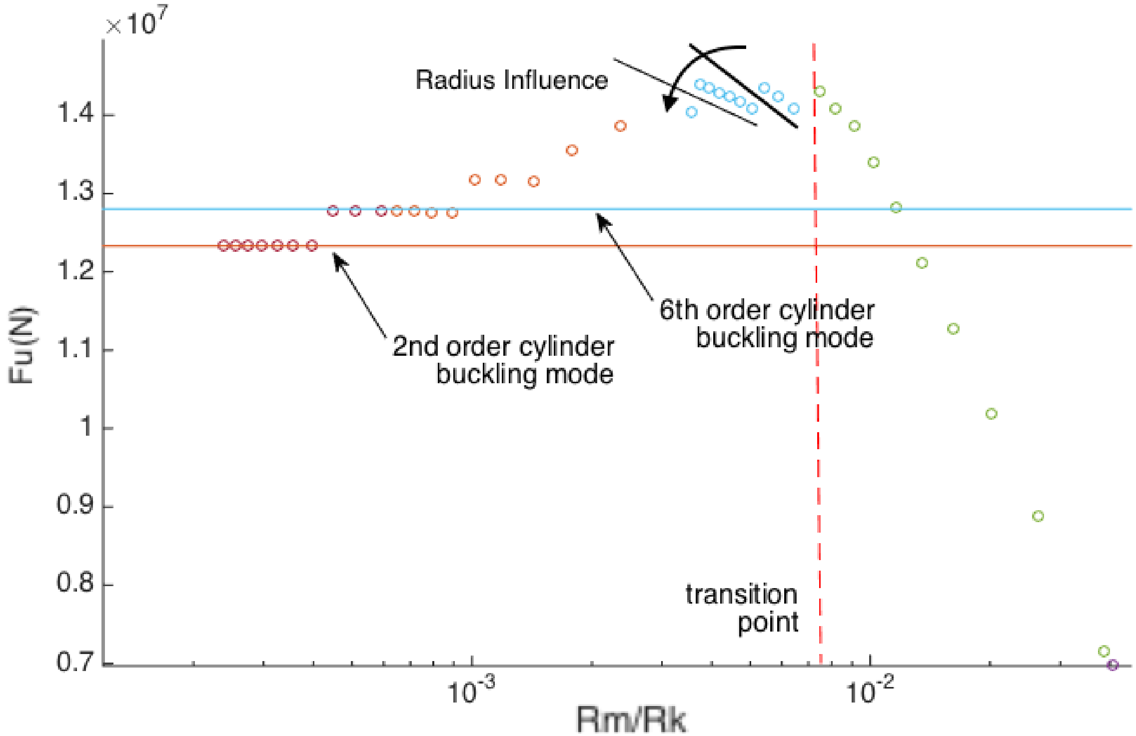

Figure 4.19: Geometric influence on ultimate reaction force,zoomed in nearly-cylinder side (in logarithmic scale) (Test No.1: Hyperboloid, Rd=2500mm, Rk=8000mm-3,500,000mm, H=10000mm, t=5mm, E=210000MPa, ν=0.3, 1^{st}modal imperfection, $\delta_{imp} = 0.2t$)

Furthermore, it is interesting to find out that the ultimate of the step of the nearly-cylinder specimen is close with the different order of the cylinder buckling behaviour. For detail, the linear buckling factor and the nonlinear buckling F-D path are compared in fig 4.20. It is surprised that the series of the nearly-cylinder behaviours are identical to the n^{th} order of the cylinder buckling modal shape. Conclude that the large vertical radial makes the hyperbolic specimens into the nearly-cylinder, and the radius influence just stimulates the first order of the near cylindrical specimen with a higher order of the modal in the exact cylinder. The specimen behaves stable at that stage until the varying radius stimulates it into another cylinder modal shape.

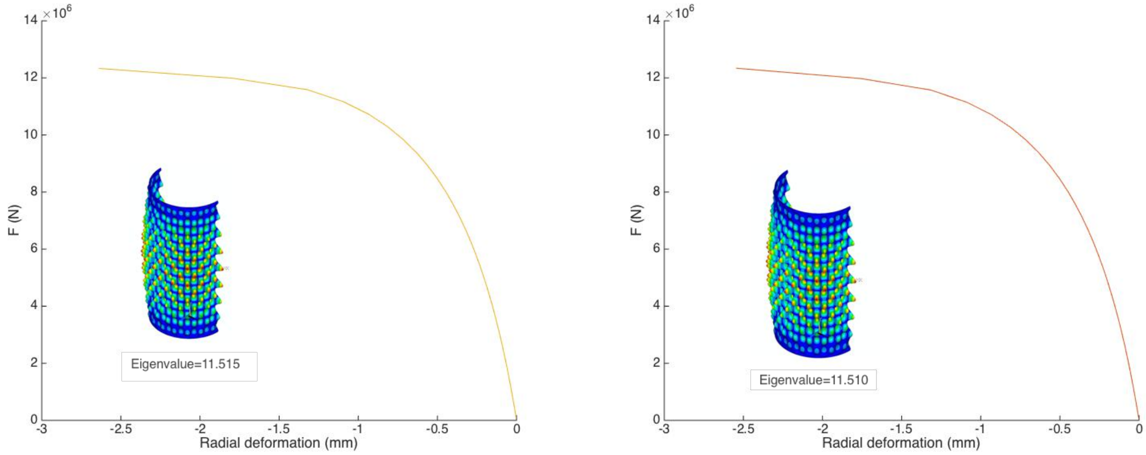

(a) nearly-cylinder (b) cylinder

Figure 4.20: Comparison between nearly-cylinder and cylinder

4.5.4 Geometrical Transition Point

The previous discussion is clearly distinguished by the geometrical transition point. We observe that with the varying thickness, there is no influence on the transition point. In this section, it is planned to find out whether the other parameters will influence the location of the transition point. Apart from the thickness(t) and the vertical radius(R_k), the specimen is defined by the edge radius(R_d), the height(H) and the material property(E,ν). The main variable is still the vertical radius R_k, being varied to change the specimen from the typical hyperboloid to nearly-cylinder and we could observe the influence on the transition point.

- **Edge Radius** R_d

  The edge radius is varied, to achieve the different curvature combination of the local sites. In standard model, the edge radius $Rd = 2500$. In this part, the varying edge radius is ranged from $Rd = 1500, 3000, 4000, 5000$.

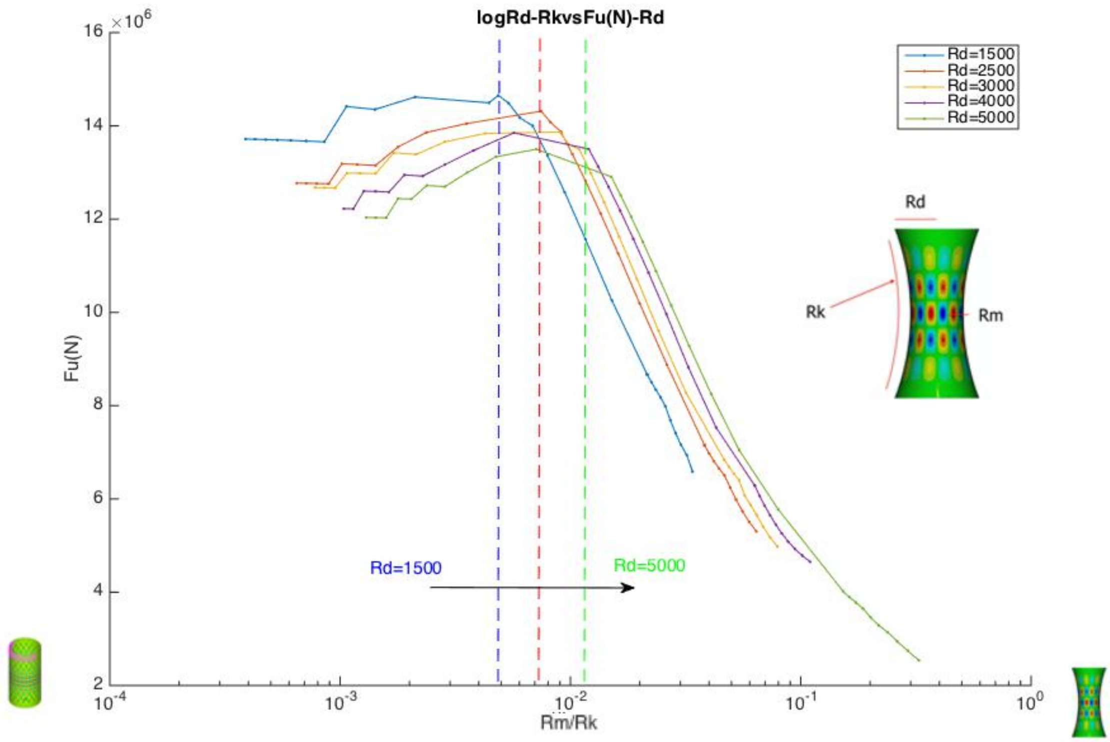

Figure 4.21: Geometric influence on ultimate reaction force with varying edge radius (logarithmic scale) (Test No.1,7,8,9,10: Hyperboloid, Rd=1500mm,2500mm,3000mm,4000mm,5000mm, Rk=8000mm-3,500,000mm, H=10000mm, t=5mm, E=210000MPa, ν=0.3, 1^{st}modal imperfection, $\delta_{imp} = 0.2t$)

It is observed that the increasing edge radius(R_d) moves the transition to the larger radius ratio side($\frac{R_m}{R_k}$). Moreover, there are two points are observed as well. 1)The varying R_d only changes the intersection of the hyperboloid parts, it indicates the R_d just effects the coefficient B. 2)The increasing radius makes the model larger, but the correspondent ultimate load at the transition point still decreases.

It is because, with the constant height, the increasing radius reduces the slenderness of the specimen; and with less curvature, the local site becomes flatter. The flat model needs larger vertical radius to stimulate the cylinder effect. Therefore, the increasing edge radius moves the transition point to the large radius ratio (hyperbolic) side. Moreover, the buckling capacity is reduced for the lack of the curvature stabilization.

- **Height** H

The height is one of the most sensitive parameters in the model. It is estimated the large height value will generate the thin-wall shell model as the pipe shape. The buckling will not occur in the shell surface but the global column buckling will happens. Such behaviour obeys the Euler buckling theory, which is beyond this thesis. Hence, the height range is varied from 7500~12000(nearly 20% from the standard model).

It is because when keeping the edge radius(R_d) constant, the increasing height makes the specimens slender and a relative smaller $\frac{R_m}{R_k}$ could approach a nearly cylinder effect. Therefore, the higher R_d moves the transition point to left side. Similar with the edge radius variation, the different heights share an identical slope and only influence the intersection parameter B.

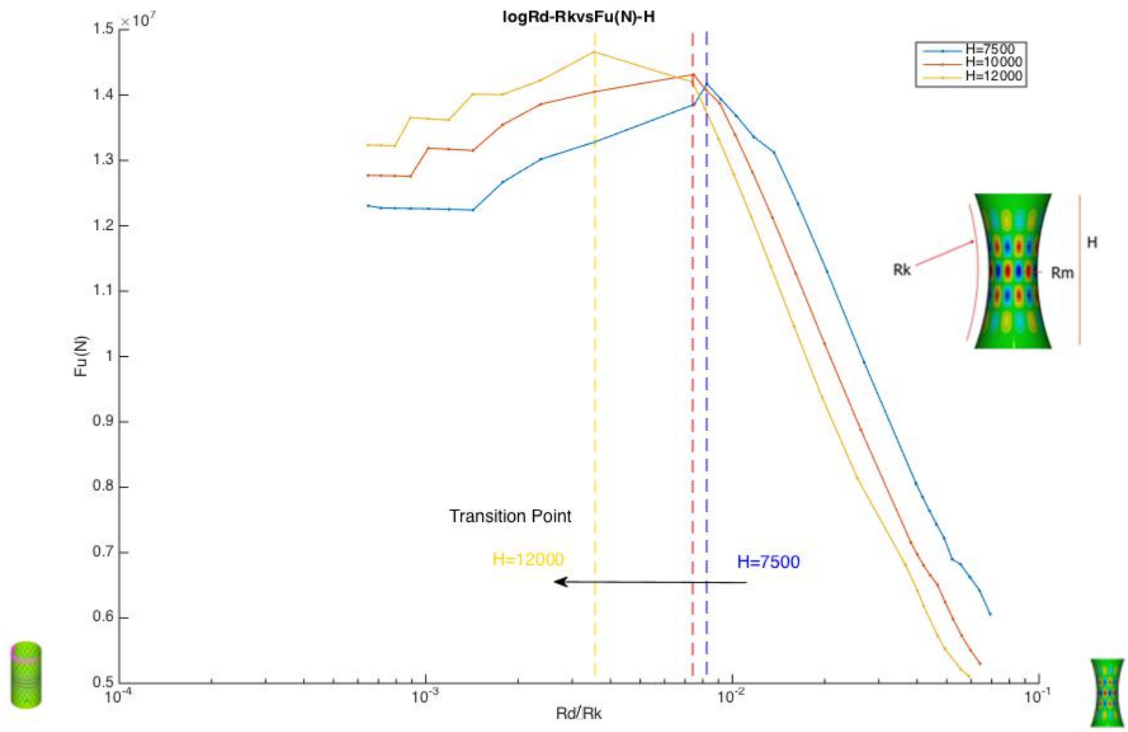

Figure 4.22: Geometric influence on ultimate reaction force with varying height (logarithmic scale) (Test No.1,11,12: Hyperboloid, Rd=2500mm, Rk=8000mm-3,500,000mm, H=7500mm,10000mm,12000mm, t=5mm, E=210000MPa, ν=0.3, 1^{st}modal imperfection, $\delta_{imp} = 0.2t$)

- **Young's Modulus** E

Young's Modulus E as a material property is not the key parameter in this research, but as a comparison of the $E = 210000MPa$ in standard model, the

$E_{new} = \frac{E}{2} = 105000MPa$ is tested. With the varying curvature ratio, the model ultimate reaction force is plotted in fig 4.23

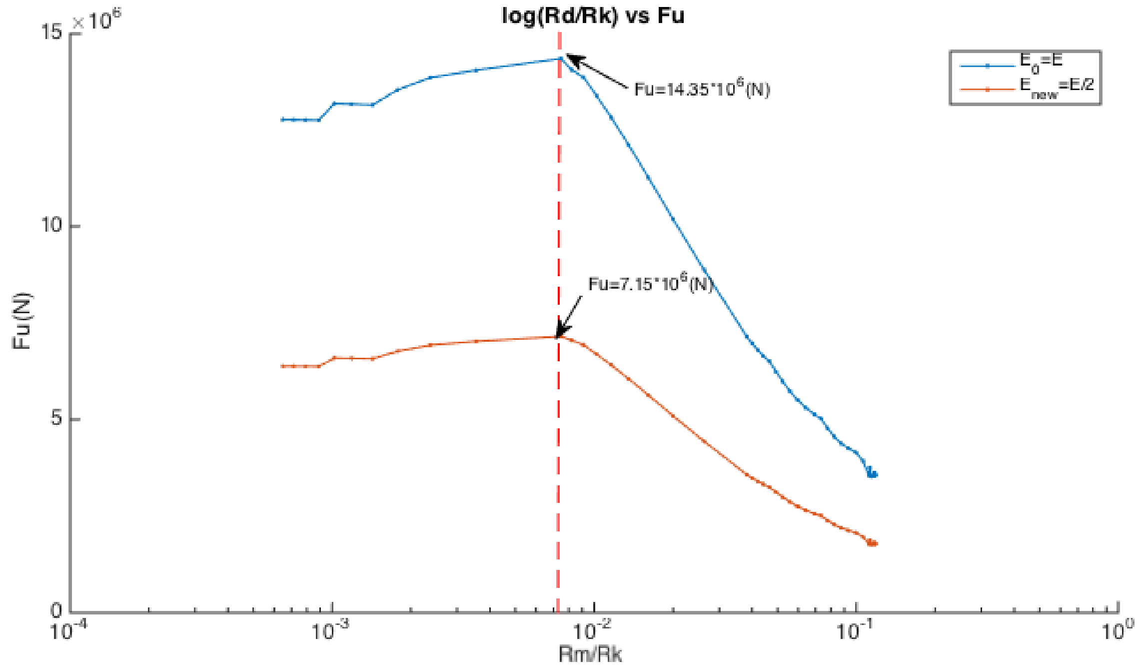

Figure 4.23: Geometric influence on ultimate reaction force with varying Young's Modulus (logarithmic scale) (Test No.1,7,8,9,10: Hyperboloid, Rd=2500mm, Rk=8000mm-3,500,000mm, H=10000mm, t=5mm, E=1050000MPa,210000MPa, ν=0.3, 1^{st}modal imperfection, $\delta_{imp} = 0.2t$)

The transition point is not influenced by the half Young's Modulus. Moreover, with the half E, the ultimate reaction force is in half as well($\frac{7.15\times10^6(N)}{14.35\times10^6(N)} = 50\%$), which is also satisfied that Young's modulus should be in the linear part.

Since the linear relation of the Young's modulus, the eq 4.5 could be rewritten in to eq 4.6.

$$\begin{aligned} F_u(\frac{R_m}{R_k}, t) &= A(t) \cdot \log(\frac{R_m}{R_k}) + B(t) \\ &= (-2.471 \cdot t + 8.609) \times 10^6 \cdot \log(\frac{R_m}{R_k}) + (-2.652 \cdot t + 7.410) \times 10^6 \\ &= 210000 \cdot [(-11.77 \cdot t + 41.95) \cdot \log(\frac{R_m}{R_k}) + (-12.63 \cdot t + 35.29)] \\ &= E \cdot [(-11.77 \cdot t + 41.95) \cdot \log(\frac{R_m}{R_k}) + (-12.63 \cdot t + 35.29)] \end{aligned} \tag{4.6}$$

- **Poisson's Ratio ν**

  Similar tests are operated with the varying Poisson's ratio, the $\nu_{new} = \frac{\nu}{2} = 0.15$ is applied. The transition point is kept constant with the change of ν, and only the slight influence on the hyperboloid side. However, the divergence occurs on the cylindrical side of the transition. Although the step-like behaviour is kept, the buckling resistance decreases greatly. It is because that on the cylinder sides the square shaped dents are stimulated, and the interaction between the perpendicular directions is aggregated. In these two geometric stage, the influence of the ν must be with different.

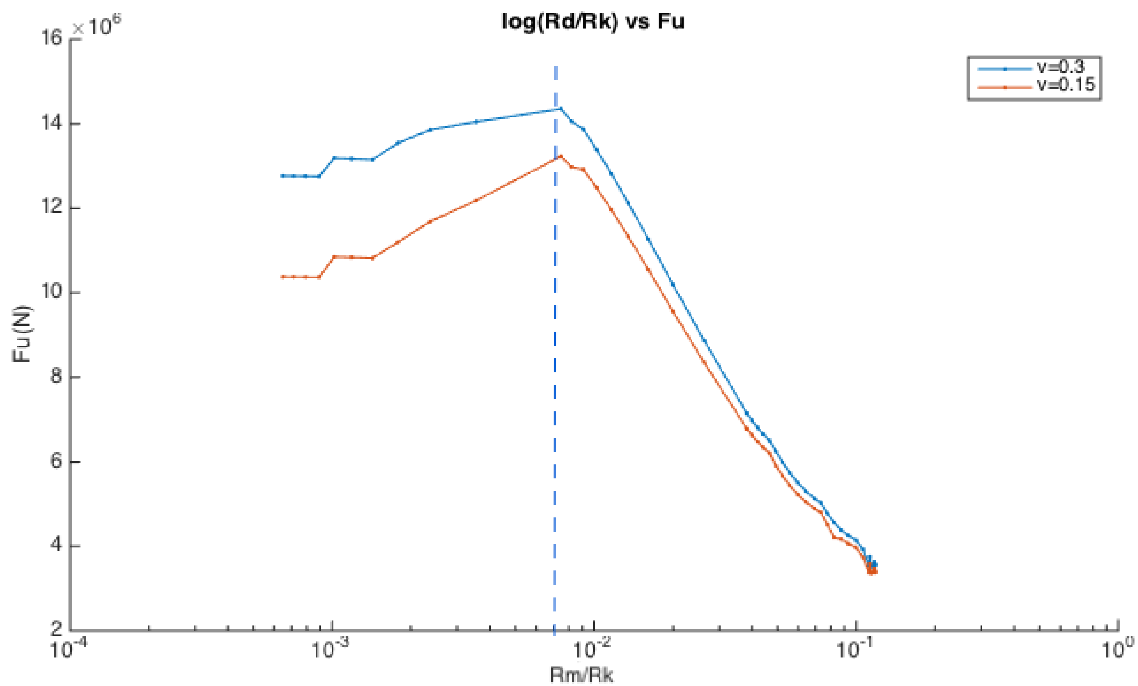

Figure 4.24: Geometric influence on ultimate reaction force with varying Poisson's Ratio (logarithmic scale) (Test No.1,7,8,9,10: Hyperboloid, Rd=2500mm, Rk=8000mm-3,500,000mm, H=10000mm, t=5mm, E=210000MPa, ν=0.15,0.3, 1^{st}modal imperfection, $\delta_{imp} = 0.2t$)

4.5.5 Summary and Conclusion

In this section, the reaction of the ultimate reaction force and the radius geometry is discussed. The vertical radius is the key parameter in the varying specimens. The geometric shape are classified into two part: the hyperboloid and the nearly-cylinder. The transition point is also investigated.

In hyperboloid, the relation between the geometric influence on ultimate reaction force and the radius ratio and varying thickness is expressed by numerical formula and the interpolated verification is used to test its accuracy. The error is induced by the residual in the curve fitting process, and also the relative definition of the imperfection amplitude is suspected.

The nearly-cylinder is recognized as the stimulated the higher order of the cylinder buckling modes. With the increase of the vertical radius, the geometric influence of the curvature is limited, and the specimen behaviours depend on the order of the cylinder model shape which is stimulated. The closer to cylinder, the lower order is activated.

In the investigation on the transition point, the variable is controlled. Both the geometric parameters(t,R_d and H) and the material property (E and ν) are tested. The thickness has no influence on the transition point, but the varying on the edge radius(R_d) and the height(H) could move the transition point position. Besides, it is also observed, that the material properties like Young's Modulus(E) and Poisson's Ratio (ν) have no influence on the transition point position.

It is concluded that the transition point, which distinguishes the hyperboloid and the nearly-cylinder is a geometric consequence. The exact cylinder is not expected as the most largest buckling load. The definition of the transition point helps to describe the specimen behaviour separately.

Table 4.6: relation between the coefficient and geometric parameters

	Coeff-A	**Coeff-B**
thickness(t)	√	√
edge radius(R_d)		√
Height(H)		√
Young's Module(E)	linear	linear
Poisson's Ratio(ν)	√	

Furthermore, the general formula could be concluded to eq 4.7. The formula of the parameter t has been studied in this part, and the other geometric parameters are supposed to be investigated in future.

$$F_u(\frac{R_m}{R_k}, t, R_d, H) = E \cdot [A(t) \cdot log(\frac{R_m}{R_k}) + B(t, H, R_d)] \tag{4.7}$$

Moreover, during the variation of the different parameters in the study of the transition point, their influence on hyperboloid part is also observed. The varying geometric parameters is also satisfied with the estimated formula shape on logarithmic relation because only the intersection and the slop are changed. It is expected the continuous numerical study can reveal the influence of the edge radius(R_d) and the height(H) in the relation of the ultimate reaction force(F_u).

4.6 Local Buckling Dents Study

In this section, the relation between the vertical membrane force(n_{yy-in}) and the local geometric parameters are discussed.The geometric parameters are combined with different trials, including the definition of the slenderness, the modified slenderness factor, the curvature ratio and the Gaussian curvature. The curve fitting is used to solve the numerical formula of the n_{yy-in}.

Table 4.7: Combination of the geometric parameters

	Trial 1	**Trial 2**	**Trial 3**	**Trial 4**
Combination	slenderness	modified slenderness	curvature ratio	Gaussian curvature
factor	$\lambda = \frac{\lambda_{yy}}{\sqrt{\frac{I}{A}}}$	$\lambda' = \lambda \cdot \frac{k_{xx}}{k_{yy}}$	$\frac{k_{xx}}{k_{yy}}$	$k_g = k_{xx} \cdot k_{yy}$

The following test results are based on the Test No.1,3,5,6 : Hyperboloid, Rd=2500mm, Rk=8000mm-3,500,000mm, H=10000mm, t=5mm,6mm,9mm,10mm, E=210000MPa, ν=0.3, 1^{st}modal imperfection, $\delta_{imp} = 0.2t$. The vertical internal force n_{yy-in} and the local curvature k_{xx}, k_{yy} are exported.

4.6.1 Combination-1: Slenderness and Modified Slenderness

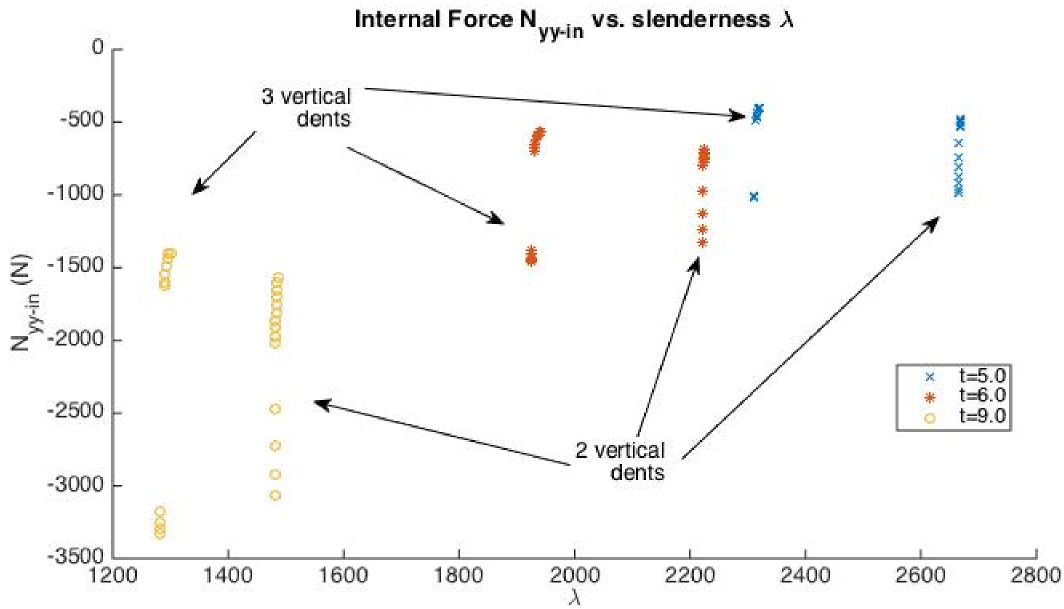

Figure 4.25: Ultimate internal force n_{yy-in} vs. λ

$$\begin{cases} \lambda = \dfrac{\lambda_{yy}}{\sqrt{\frac{I}{A}}} \\ I = \dfrac{1}{12}\lambda_{xx}t^3, A = \lambda_{xx}t \end{cases} \tag{4.8}$$

As previous discussion, the slender dents shape are estimated as the column behaviour. The buckling dents is described as a strip with the rectangular cross section, and the curvature influence is taken into the buckling wave length calculation. It is straight forward to generate the parameters as the definition of the slenderness eq 4.8. Unfortunately, the fig 4.25 shows, that with the varying of the slenderness, its influence on the ultimate internal force is limited. The slenderness is not an ideal independent variable to describe the local dents behaviour. Further, the influence of the radius is taken into consideration.

The curvature factor is applied as a modifier. It is obvious that the horizontal curvature(k_{xx}) is able to stabilize the buckling occurrence, and the vertical curvature(k_{yy}) could reduce the buckling capacity. Hence, the curvature factor is defined as $\frac{k_{xx}}{k_{yy}}$. And the combination of the geometric parameters is defined as modified slenderness in eq 4.10. Notes that the curvature is a definition on the buckling local site, and radius ratio previously used is describe a general model. For the buckling position is not fixed, there is no direct relation between the $\frac{k_{xx}}{k_{yy}}$ and $\frac{R_m}{R_k}$, except the buckle occur in the exact middle and that the $\frac{k_{xx}}{k_{yy}}$ is equal to $1/\frac{R_m}{R_k}$.

$$\lambda' = \lambda \cdot \frac{k_{xx}}{k_{yy}} \tag{4.9}$$

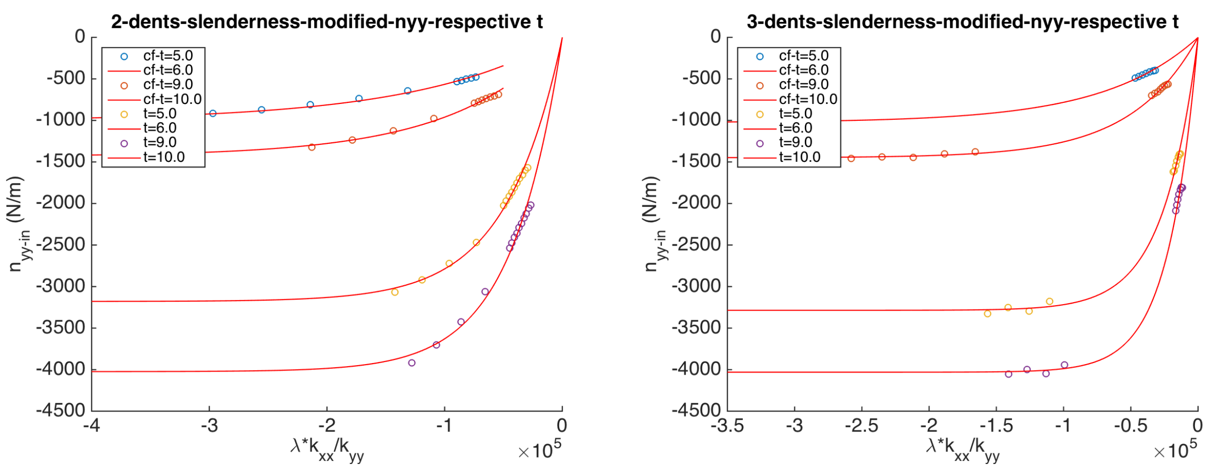

(a) 2 buckles (b) 3 buckles

Figure 4.26: Ultimate internal force versus modified slenderness (scatter & 1^{st}curve fitting result)

$$n_{yy} = A(t) \cdot (1 - e^{B(t) \cdot \lambda' \times 10^{-6}}) \tag{4.10}$$

The dots are scattered with the modified slenderness (λ') and the vertical membrane force at inward dents (n_{yy-in}). Because the different dent amounts in vertical direction, the internal force is discontinuous. The data is grouped by the vertical dents distribution. According to the plot, it is estimated that the dots with constant thickness obeys the exponential relation in shape eq 4.10. The coefficients A,B depend on the varying thickness. Similarly as the previous curve fitting process, the first curve fitting trial is based on the estimated exponential shape. According to the result of two buckles in vertical direction, the coefficients A,B are solved with correspondent thickness, and the related results are in table 4.8.

Table 4.8: Coefficients table with thickness(modified slenderness with 2 buckles)

t-mm	**A**-$\frac{N}{mm}$	(95% confidence bounds)	**B**	(95% confidence bounds)
5	-1007	(-1037, -976.1)	8.25	(7.67, 8.34)
6	-1433	(-1496, -1370)	11.09	(10.17, 12.02)
9	-3179	(-3271, -3087)	20.94	(21.22, 25.02)
10	-4024	(-4196, -3852)	23.21	(19.72, 22.16)

From the plot of the coefficients A,B, both of the coefficients are in a linear relation with the varying thickness, in fig 4.27. Hence, let the second curve fitting trial based on the data in table 4.8, to solve the A(t) and B(t).

The same process is applied on data of the 3 buckles results, and the coefficient relations are plotted in following. and the correspondent equation.

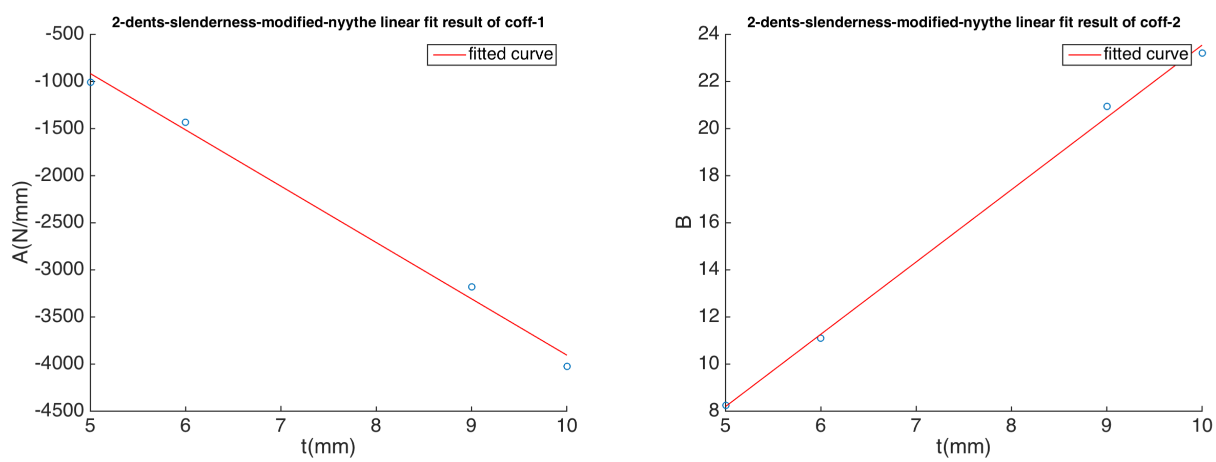

(a) Coefficient A(t)

(b) Coefficient B(t)

Figure 4.27: Coefficients with varying thickness (modified slenderness with 2 buckles)

$$\begin{cases} A(t) = -597.7 \cdot t + 2072 \\ B(t) = 3.069 \cdot t - 7.141 \end{cases} \tag{4.11}$$

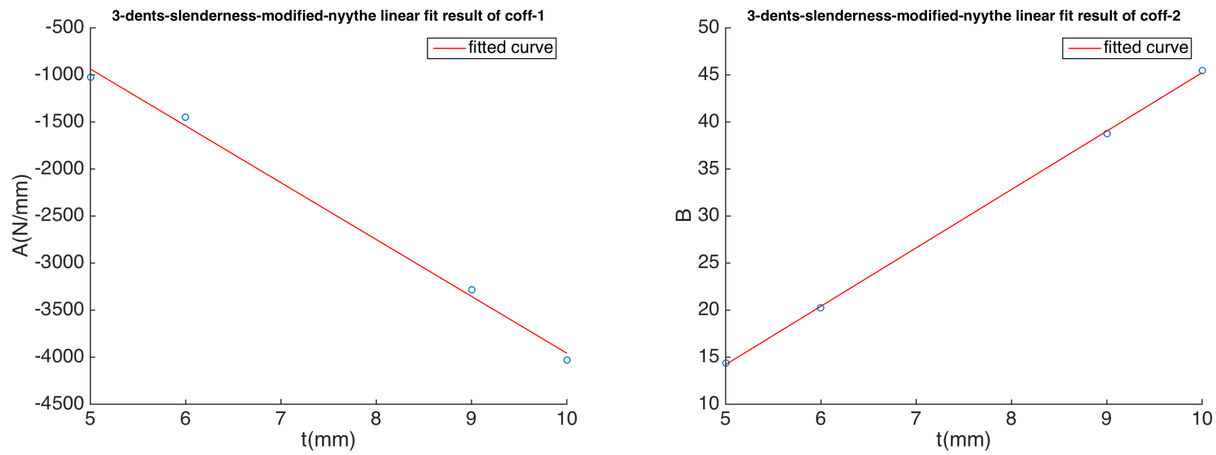

(a) Coefficient A(t)

(b) Coefficient B(t)

Figure 4.28: Coefficients with varying thickness (modified slenderness with 3 buckles)

$$\begin{cases} A(t) = -604 \cdot t + 2082 \\ B(t) = 6.204 \cdot t - 16.81 \end{cases} \tag{4.12}$$

Comparing the coefficient equations(eq 4.11 and eq 4.12), we observe that the in different dents distribution, the relation between the coefficient A and the thickness is comparable. In the estimated formula shape(eq 4.10) the identical coefficient A(t) keeps the reduction degree influence. On the other hand, the coefficient B(t) has a different formula between the different vertical dents distribution. It indicates that the decay speeds of the ultimate buckling internal force n_{yy-in} is influenced by the dents distribution.

4.6.2 Combination-2: Curvature Ratio

In order to study the curvature influence, the previous definition of the curvature ratio is inherited and investigated separately. The $\frac{k_{xx}}{k_{yy}}$ is set as the horizontal axis. The scatters are separated by double buckles distribution and the triple buckles distribution in fig 4.29.

$$n_{yy} = A(t) \cdot (1 - e^{B(t) \cdot \frac{k_{xx}}{k_{yy}} \times 10^{-6}}) \tag{4.13}$$

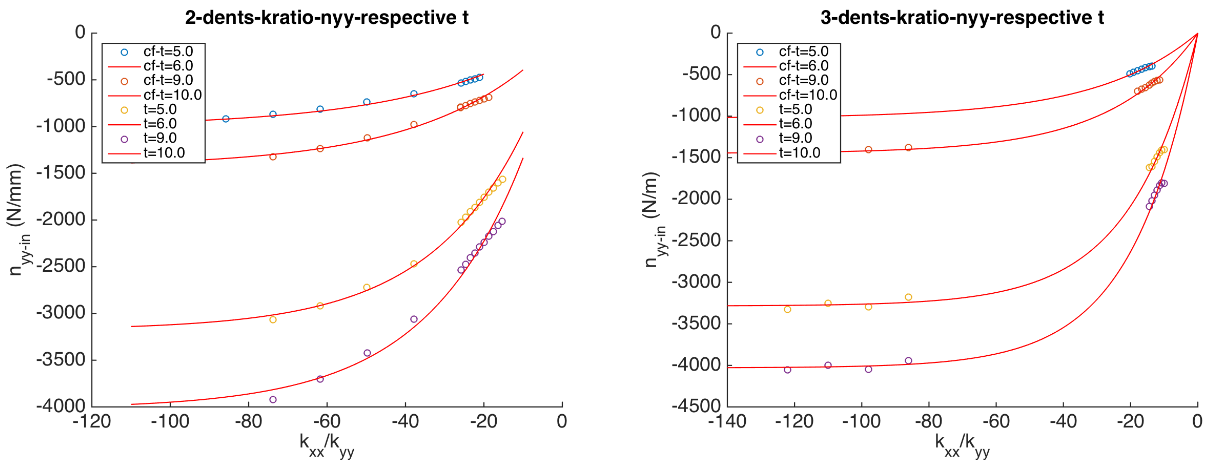

(a) 2 buckles

(b) 3 buckles

Figure 4.29: Ultimate internal force vs. curvature ratio(scatter & 1^{st} curve fitting result)

For the trends are very similar with the combination of the modified slenderness, the same exponential relation is tried as well. The only difference of the horizontal distribution of the dots are caused by the nearly constant slenderness value(λ). Hence, the same formula shape in eq 4.10 is applied. The 1^{st} curve fitting trial generates the coefficients. The correspondent coefficients with the varying thickness are collected in the table 4.9

Table 4.9: Coefficients table with varying thickness (curvature ratio with 2 buckles)

t-mm	**A**-$\frac{N}{mm}$	(95% confidence bounds)	**B**$\times 10^4$	(95% confidence bounds)
5	-1006	(-1037, -975.5)	2.863	(2.659, 3.067)
6	-1432	(-1496, -1369)	3.211	(2.94, 3.482)
9	-3177	(-3270, -3083)	4.042	(3.803, 4.282)
10	-4020	(-4194, -3847)	4.034	(3.684, 4.384)

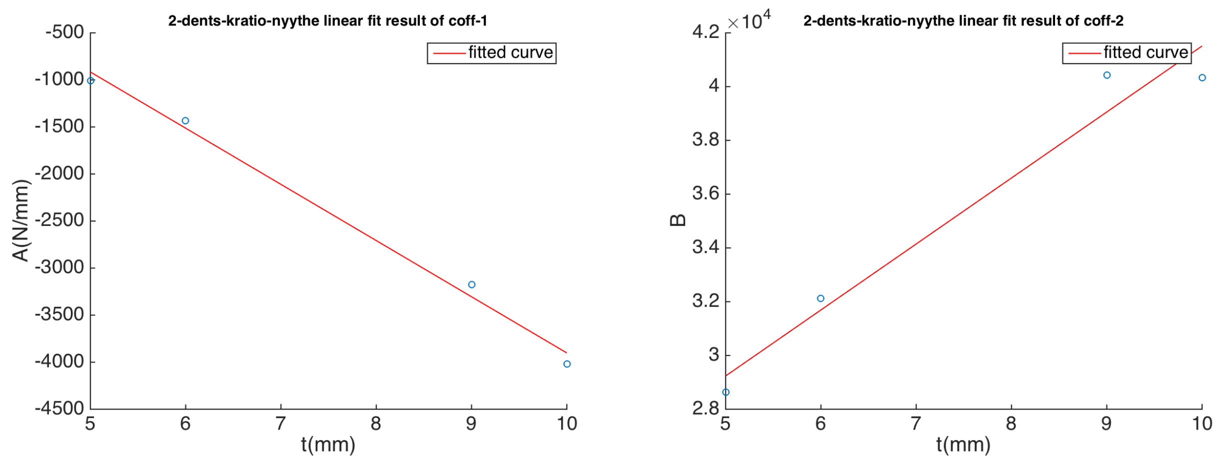

(a) Coefficient A(t)

(b) Coefficient B(t)

Figure 4.30: Coefficients with varying thickness (curvature ratio with 2 buckles)

As the previous trial, the obvious linear relation is observed in fig 4.30, the coefficient equation is solved as well.

For 2 buckles The previous results are combined, and the equation of the local buckling formula is derived in eq 4.14.

$$\begin{cases} n_{yy-in} = A(t) \cdot (1 - e^{B(t) \cdot \frac{k_{yy}}{k_{xx}} \times 10^{-6}}) \\ A(t) = -597.2 \cdot t + 2070 \\ B(t) = 2455 \cdot t + 1.697 \times 10^4 \end{cases} \tag{4.14}$$

For 3 buckles The similar numerical analysis process is done, and the derived equation is in eq 4.15.

$$\begin{cases} n_{yy-in} = A(t) \cdot (1 - e^{B(t) \cdot \frac{k_{yy}}{k_{xx}} \times 10^{-6}}) \\ A(t) = -603 \cdot t + 2082 \\ B(t) = 3847 \cdot t + 1.506 \times 10^4 \end{cases} \tag{4.15}$$

To verify the accuracy of the numerical formula, the curves in fig 4.31 are plotted by eq 4.14 and eq 4.15; and the dots are the GNLBA results. It is actuate enough to describe to nonlinear test results scatter with the numerical curve fitting equation.

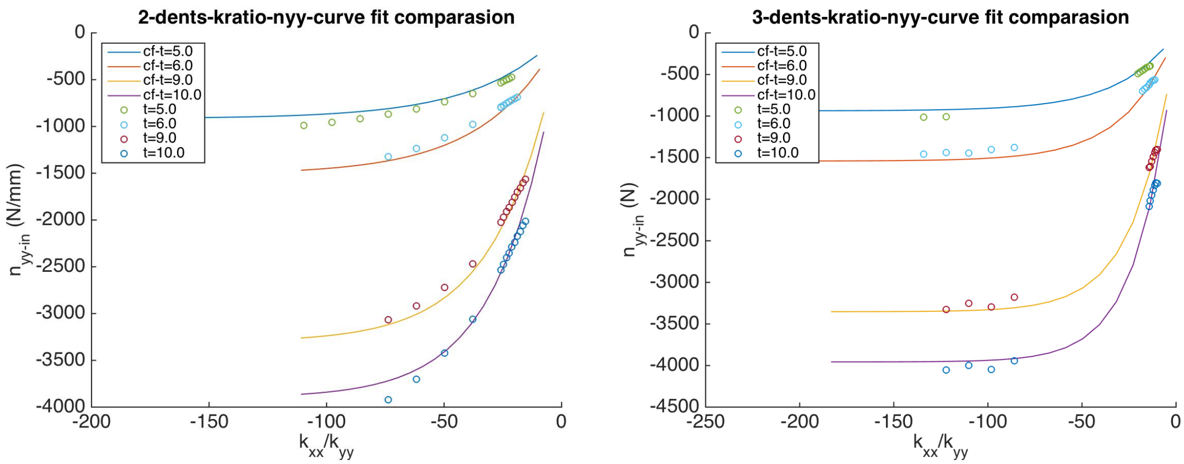

(a) 2 buckles (b) 3 buckles

Figure 4.31: Comparison between the curve fitting formula (lines) and the nonlinear results (dots) (curvature ratio with 2 buckles& 3 buckles)

Moreover, in fig half Young's modulus reduces the ultimate membrane stress state into half. Hence, the linear influence of the Young's modulus property has been checked.

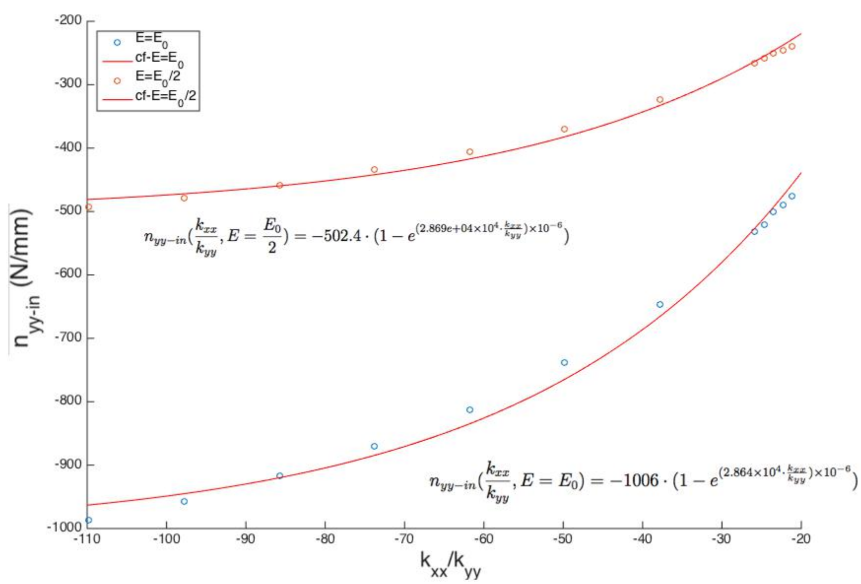

Figure 4.32: Half Young's modulus influence on ultimate state of n_{yy-in} (2-buckles) (Test No.1,13 : Hyperboloid, Rd=2500mm, Rk=8000mm-3,500,000mm, H=10000mm, t=5mm, E=210000MPa and 1050000MPa, ν=0.3, 1^{st}modal imperfection, $\delta_{imp} = 0.2t$)

In a practical view, it is supposed to merge the 2-buckles results and the 3-buckles together. The generalised formula is expressed in eq 4.16, and as the linear property, Young's modulus part is separated.

$$\begin{cases} n_{yy-in} = E \cdot A(t)(1 - e^{B(t) \cdot \frac{k_{yy}}{k_{xx}} \times 10^{-6}}) \quad A(t) = (-2.823 \cdot t + 9.767) \times 10^{-3} \\ B(t) = 2763 \cdot t - 1.751 \times 10^{4} \\ E = 210000 \dfrac{N}{mm^2} \end{cases} \tag{4.16}$$

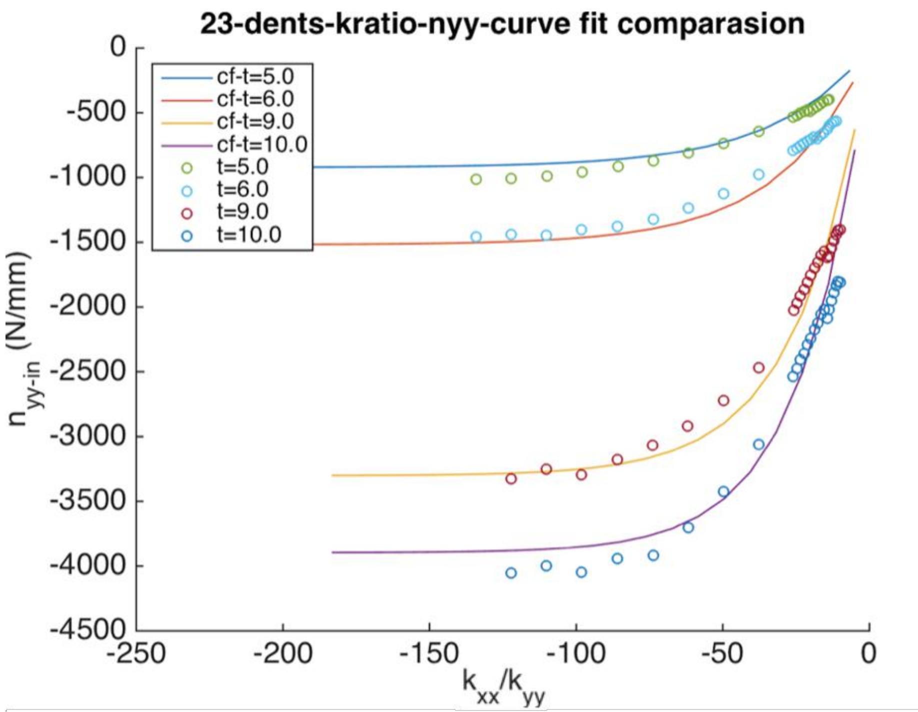

Figure 4.33: Plot of the numerical formula with curvature ratio (combination of 2 buckles and 3 buckles results)

Comparing the modified slenderness combination and the curvature ratio, they share the same trend, and the influence of the slenderness (λ) is limited with the constant model height.

At the ultimate state, the influence of the buckling dents dimension is limited with the same buckles distribution and the critical factor is caused by the curvature. With the numerical curve fitting method, the generalized formula by curvature ratio is accurate to describe the internal stress at the ultimate state.

It is also possible that it is restrained by the constant height of the specimen, the wave length of the buckling length is not able to develop freely, and it changes only caused by the surface distance influence. To investigate the influence of the buckling wave length, it is supposed to vary the height of the model as well. Let the height as a key variable to observe the influence.

4.6.3 Combination-3: Gaussian Curvature

Since the influence of the curvature has been released in the proceeding discussion, the Gaussian curvature as a critical geometric parameter in shell analysis is investigated in this section. As the definition, the Gaussian curvature is calculated by the multiple of the principal curvature, in eq 4.17. Considering the buckling dents happen in the middle of the specimens, to keep the geometric parameter, the principal curvatures are simplified to the correspondent the curvatures in vertical and the horizontal.

$$k_g = k_1 \cdot k_2 \approx k_{xx} \cdot k_{yy} \tag{4.17}$$

in the middle zone of the height.

Following the scatters of the results, the estimated formula is shaped in the exponential equation, eq 4.18.

$$n_{yy} = A(t) \cdot k_g^{B(t)} = A(t) \cdot (k_{xx} \cdot k_{yy})^{B(t)} \tag{4.18}$$

The scatters are plotted in the same way, in fig 4.34.

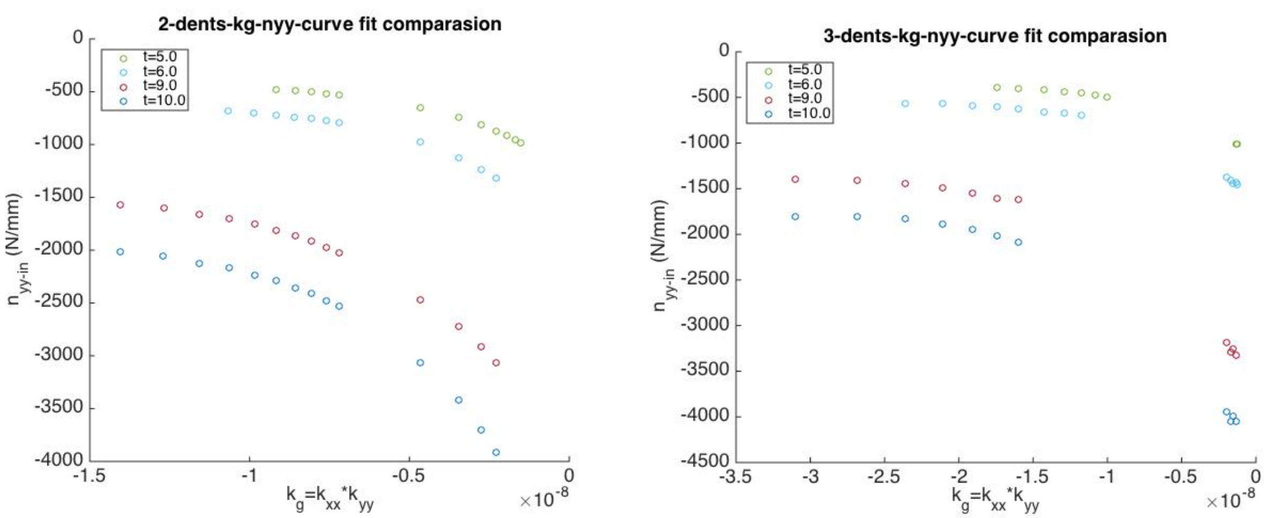

(a) 2 buckles (b) 3 buckles

Figure 4.34: Ultimate internal force n_{yy-in} vs k_g

The coefficients of A and B with varying thickness are plotted in fig 4.35. The linear curve fitting is not able to describe the relation. To generate the relation based on the gaussian curvature needs more samples to finish the curve fitting on the coefficients.

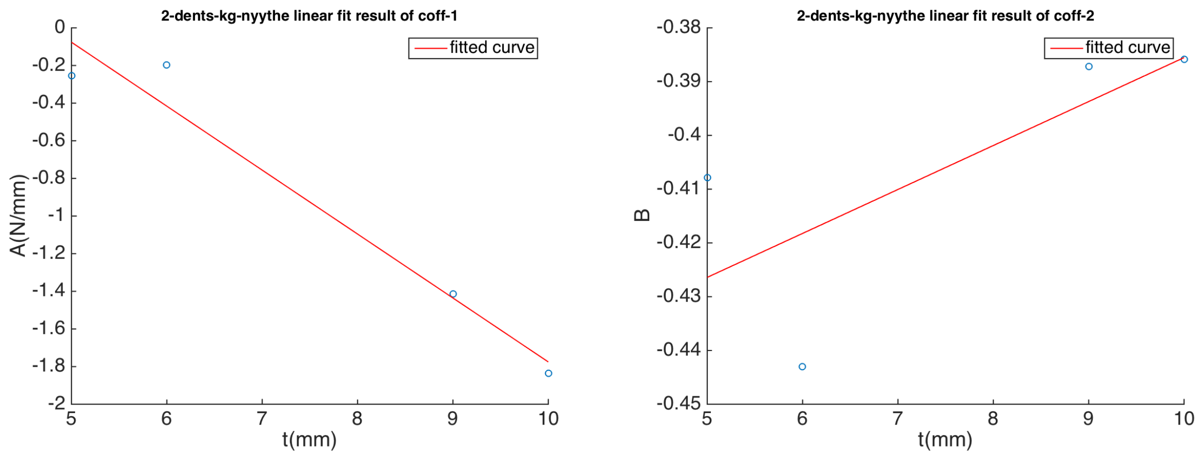

(a) Coefficient A(t) (b) Coefficient B(t)

Figure 4.35: Coefficients with varying thickness (Gaussian curvature with 2 buckles)

4.6.4 Summary and Conclusion

In this section, the numerical study is focused on the influence of the ultimate buckling membrane stress in vertical direction at the inward buckles n_{yy-in}. Based on the assumption to separate the influence of local geometric parameters, different geometric combinations are investigated as the independent variable, and the thickness influences the related coefficients separately.

It is concluded that with the constant buckle distribution, the buckle slenderness influence is limited and the most critical influence is the local curvature. The equation between the curvature ratio $\frac{k_{xx}}{k_{yy}}$ and the ultimate membrane stress n_{yy-in} is expressed (eq 4.16). Both of the coefficients are investigated in the linear relation with the varying thickness. With the trial on gaussian curvature, the scatters are successfully fitted by the exponential relation, but the there is not the linear relation with the varying thickness and the related coefficients. To generate an equation for the local Gaussian curvature, the more different thickness specimens are needed.

4.7 Local Ultimate Stress State

The previous mechanism has already revealed the relation between the geometric parameters with the buckling load or the internal force. In practical, when the designer concerns the buckling behaviour of a structure, the ultimate buckling stress is a handy tool to assess the structure behaviour. Based on the linear buckling analysis, the designer is able to get the buckling pattern of the model, including the dent dimensions and deformation ratio. However, the stress state is lacked.

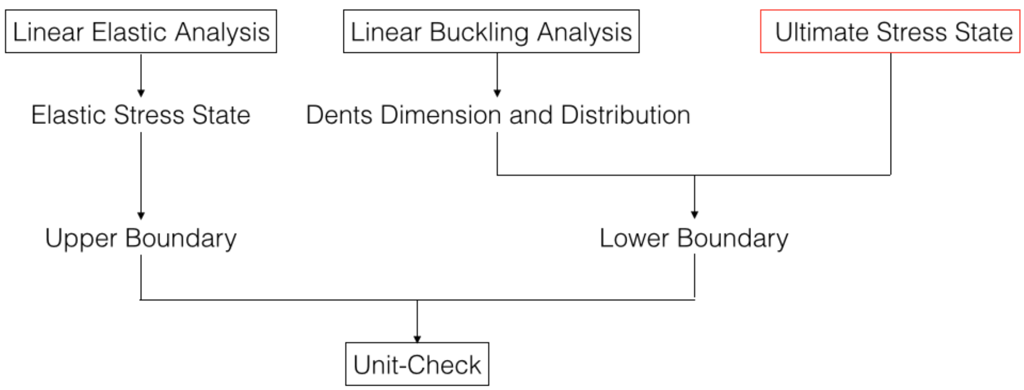

Figure 4.36: Ultimate Stress Design Workflow

Therefore, the author provides a series of the design curves on the ultimate stress state with the dents geometric information. The ultimate stress state as a lower boundary is used to estimates the structure behaviour. Based on the conclusion of the previous section, as the critical geometric parameter,the curvature ratio is used to describe the ultimate stress state, in fig 4.37. The designer just needs to run the linear elastic analysis to calculate the upper boundary of the stress state, and finishes the unit-check to ensure the structure is in the safe side.

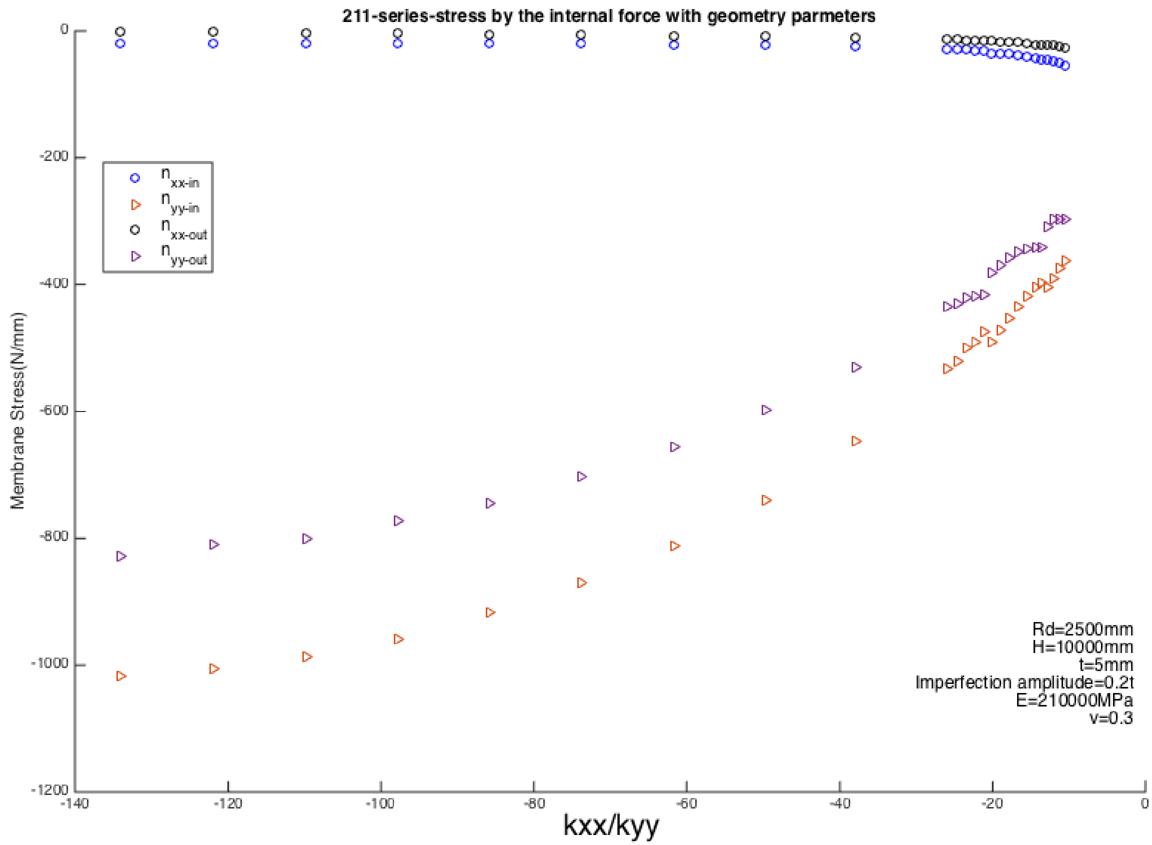

Figure 4.37: Ultimate Stress State

CHAPTER 5

Conclusions and Recommendations

5.1 Conclusions

- **A peak load occurs only for small imperfection.** For imperfection larger than $0.2t$, the load displacement curve increases continuously due to the assumption of linear elastic material behaviour. Therefore, a peak load does not occur. In this study, an imperfection of $0.2t$ has been used for which a peak load does occur.

- **A small non-modal imperfection causes buckling in the shape of the first buckling mode.** A large non-modal imperfection causes buckling in the shape of a summation of several buckling modes.

- **In negatively curved shells the load is carried in three ways.** These ways are the outward buckles, the inward buckles and the material in-between. For small negative curvatures the load is carried in two ways, in-between material does not contribute separately any more.

- **Buckling in negatively curved shells is preceded by an outward buckle.** Different from the inward buckles, the failure in outward buckles is always earlier than the global failure. Hence, if we would observe the outward buckle performance by strain gauges, it would provide a good predication of the global failure.

- **A nearly cylinder with a very small negative curvature is stronger than an exact cylinder.** Hyperboloid global buckling analysis is separated in two parts: the hyperboloid part and the nearly cylinder part. The transition point depends on height and the edge radius only, and is independent from the thickness. In the nearly cylinder behaviour the fundamental buckling modes are suppressed by hardly visible curvature. Hence, the models only show high order buckling shapes. For this reason, their capacities are higher than that of the exact cylinder geometry.

- **The ultimate buckling load can be expressed as a function of geometric parameters.** Through data processing of finite element results a formula has been obtained that describes the ultimate reaction force. The principal parameters are the vertical radius and the middle radius, and the secondary parameter is the thickness.

- **The peak membrane force in the inward buckles can be expressed as a function of the local curvature.** The curvature ratio $\frac{k_{xx}}{k_{yy}}$ is selected as the independent parameter. The numerical curve fitting results are merged in one general equation which covers the curvature ratio from -150$\sim$-10.

5.2 Recommendations

The following recommendations for further research can be given.

- **More analysis of large curvature ratios**

  The hyperboloid model in thesis has a physical restraint that the curvature ratio has only been varied in a specified range. To generate more generally applicable formulas, a larger range of the curvature is needed.

- **Free buckling form shape**

  The buckle shape and the distribution are confined by the boundary conditions. In this thesis, a stabilized middle zone buckling is aimed for avoid the boundary influence. But the buckling wave length cannot be changed freely. It will be very interesting to design a continuously changing curvature shell, which has unlimited boundary, likes spiral. This would not only solve the physical boundary restraints but also could have a freely changing curvature, to provide a free buckling form.

- **Spheroid edge buckling**

  The fundamental buckling modes in spheroid concentrate on the edge area. To suppress the edge buckling, the pressure perpendicular to the surface was applied. The results is limited, pressured zone was expanded but the edge buckling was not eliminated. However, it also provides an interesting phenomenon that the hoop stress seems has limited influence on the edge buckling. It is recommended to study edge buckling further.

- **Modal interaction**

  Modal interaction is always a difficult problem in the imperfection study. In this thesis, the first buckling mode is treated as the most critical imperfection and implemented on the specimens. But the modal displacement study also shows that the modal interaction emerges, when a large non-modal imperfection is implemented. Observing the imperfection influence in the modal displacement scope may bring some surprising results on modal interaction influence.

- **Imperfection description**

  The relative imperfection amplitude definition ($\delta_{imp} = 0.2t$) is used in this research to describe the imperfection influence. However, when the parametric controlled test sets are compared to thickness test sets the imperfection $\delta_{imp} = 0.2t$ was kept constant. It seems that the thickness is the only changing condition, actually the imperfection is changing as well. This obstructs the investigation of thickness. It is recommended to use the imperfection as an independent parameter. The description method of the imperfection is expected to finish in future.

- **3-D numerical surface fitting**

  Since the database has already been set up covering more than 700 models, people can perform data processing on the database results. The trial on 3-D numerical surface fitting is a powerful tools that could be developed. The 3-D surface fitting provides a more widely overview on more parameters influence. The further study must be very interesting.

List of Figures

List of Tables

Bibliography

[1] R. K. Annabattula, J. M. Veenstra, Y. F. Mei, O. G. Schmidt, and P. R. Onck. Self-organization of linear nanochannel networks. *Physical Review B - Condensed Matter and Materials Physics*, 81(22):1–9, 2010.

[2] Bernard Budiansky. A Survey of Some Buck. *AIAA Journal*, 4(9):1505–1510, 1966.

[3] David Bushnell. Buckling of Shells Pitfall for Designers. *AIAA Journal*, 19(9):1183–1226, 1981.

[4] Tian Chen. On Introducing Imperfection in the Non-Linear Analysis of Buckling of Thin Shell Structures. 2014.

[5] K.Miamis C.Maraveas. Shell buckling evaluation of thin-walled steel tanks filled at low liquid level according to current design codes. *Proceedings of the Annual Stability Conference Structural Stability Research Council*, pages 710–724, 2013.

[6] L.H. Donnell. A New Theory for the Buckling of Thin Cylinders Under Axial Com pression and Bending. *Transactions of the ASME, Aeronautical Engineering*, AER-56-12(473):795–806, 1935.

[7] Isaac Elishakoff. Probabilistic resolution of the twentieth century conundrum in elastic stability. *Thin-Walled Structures*, 59:35–57, 2012.

[8] West Germany. On Local Buckling of Thin Shells. 20(4):249–259, 1985.

[9] J W Hutchinson and W T Koiter. Postbuckling Theory. *Applied Mechanics Reviews*, 23(12):1353–1366, 1970.

[10] Ansys inc. ANSYS Mechanical APDL Command Reference. 15317(November):724–746, 2013.

[11] Ansys inc. ANSYS Mechanical APDL Theory Reference. 15317(November):724–746, 2013.

[12] Warner Tjardus Koiter. The Stability of Elastic Equilibrium, 1945.

[13] Eugene E Lundquist. Strength tests of thin-walled duralumin cylinders in compression. *Journal of the Franklin Institute*, 217(4):537, 1934.

[14] S. a. Ragon, Z. Gürdal, and L. T. Watson. A comparison of three algorithms for tracing nonlinear equilibrium paths of structural systems. *International Journal of Solids and Structures*, 39(3):689–698, 2002.

[15] Structural Shell. SHELL281 Element Description SHELL. In *Ansys Element*. 2014.

[16] Th Von Kármán, Louis G. Dunn, and Hsue Shen Tsien. The Influence of Curvature on the Buckling Characteristics of Structures. *Collected Works of Hsue-Shen Tsien (1938-1956)*, pages 122–145, 2012.

APPENDIX A

An example of the two-phased numerical curve fitting analysis

1. **Select Analysis Data**

   The database is generated by the NLBA tests with varying geometric parameters. After each NLBA test, the model result is exported, including the internal force, the ultimate reaction force and the buckles geometric information. In numerical analysis, the most important thing is to select the independent and dependent parameters based on the database. Because the research is aimed to find out the influence of both the local geometric parameters and the thickness, it needs to select the independent parameter with the combination of the geometric parameters at first.

   It means that every point in the following plot indicates a NLBA test.

   example: Select the radius ratio $\frac{R_m}{R_k}$ as the main independent parameter, and the thickness t as the secondary independent parameter. The ultimate total reaction force(Fu) at the buckling stage is set as dependent parameter. The data is classified with different thickness(t), and the entire data is appended at the end in table A.3.

2. **Estimate Formula Shape**

   Before the curve fitting process, the formula shape should be selected at first. It could be achieved by several way, the most direct is to derive the related formula, and it could also be estimated by the trend of the curve itself. We construct the general shape of the formula, and the coefficients are solved in the following curve fitting.

example: Based on the NLBA results scatters, it is observed that the linear relation between the $\frac{R_m}{R_k}$ and F_u is in logarithmic scale. The dots are classified with different thickness, and the varying thickness changes the slope and the intersection at same time. Therefore, we could formulate the shape as eq A.1.

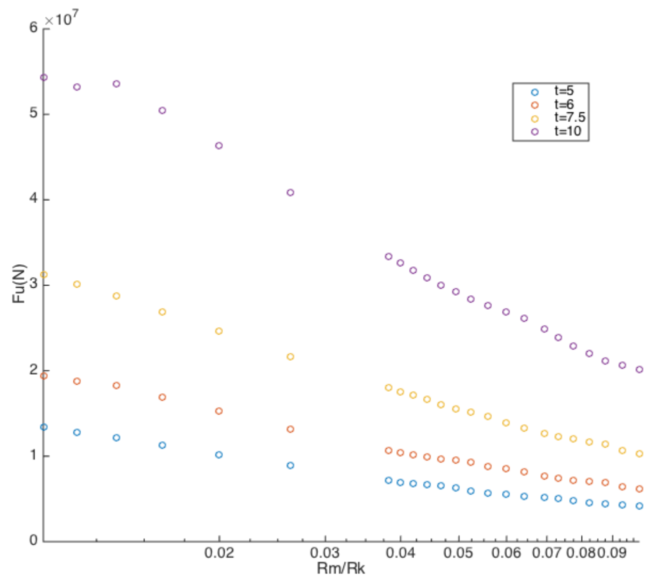

Figure A.1: example:radius ratio($\frac{R_m}{R_k}$) and ultimate reaction force (F_u)

$$F_u = A(t) \times log(\frac{R_m}{R_k}) + B(t) \tag{A.1}$$

3. **Apply Curve Fitting Trial (1^{st}) with specified thickness** The 1^{st} curve fitting trial is operated between the main independent parameter and the dependent parameter, keeping the secondary independent parameter in constant. For the a specified thickness value, the curve fitting process is done based on the estimated formula shape. The coefficients are solved.

   example: The specified thickness($t = 5$) is processed between the $\frac{R_m}{R_k}$ and F_u at first. After the curve fitting process, the result curve,based on the eq A.1, is accurate enough to describe the NLBA scatters. And the coefficients A($t = 5$) and B($t = 5$) are recorded.

Table A.1: example:coefficients table with thickness,$t = 5$

t	**A** $\times 10^6$N	(95% confidence bounds)	**B**$\times 10^6$N	(95% confidence bounds)
5	-4.154	(-4.347, -3.966)	-6.026	(-6.652, -5.401)

4. **Iterate 1^{st} Curve Fitting with Varying** t Iterate the similiar process in last step, with the different thickness, the correspondent coefficients are solved.

   example: The curve fitting is applied to $t = 6$, $t = 7.5$ and $t = 10$. The respective curve fitting result performs greatly with the NLBA results. The coefficients $A(t = 6), B(t = 6)$, $A(t = 7.5), B(t = 7.5)$ and $A(t = 10), B(t = 10)$ are recorded.

5. **Generate Coefficient Relation** According to the previous curve fitting results, the correspondent coefficients are collected.

   example: With varying thickness, the correspondent coefficients A and B are collected in table A.2.

Table A.2: example:coefficients table with thickness

t	**A** $\times 10^6$N	(95% confidence bounds)	**B**$\times 10^6$N	(95% confidence bounds)
5	-4.154	(-4.347, -3.966)	-6.026	(-6.652, -5.401)
6	-6.021	(-6.298, -5.743)	-8.369	(-9.265, -7.473)
7.5	-9.425	(-9.719, -9.131)	-12.33	(-13.281, -11.380)
10	-16.391	(-17.082, -15.701)	-19.212	(-21.424, -16.991)

6. **Apply Curve Fitting Trial (2^{nd})** In this step, the relation between the solved coefficients and the secondary independent parameter(t). Plot the coefficients A and B with thickness$t$ respectively, and the 2^{nd} curve fitting helps to solve the formula $A(t)$ and $B(t)$. It is noted that when it is a linear relation, only 4-5 groups of coefficients result are sufficient, but if the relation is quadratic or exponential, more groups are needed.

   example: The graph between A and B with t is plotted in fig A.2. It is evident that there is a linear relation, and the linear formula describes the A(t) and B(t) are solved in eq A.2.

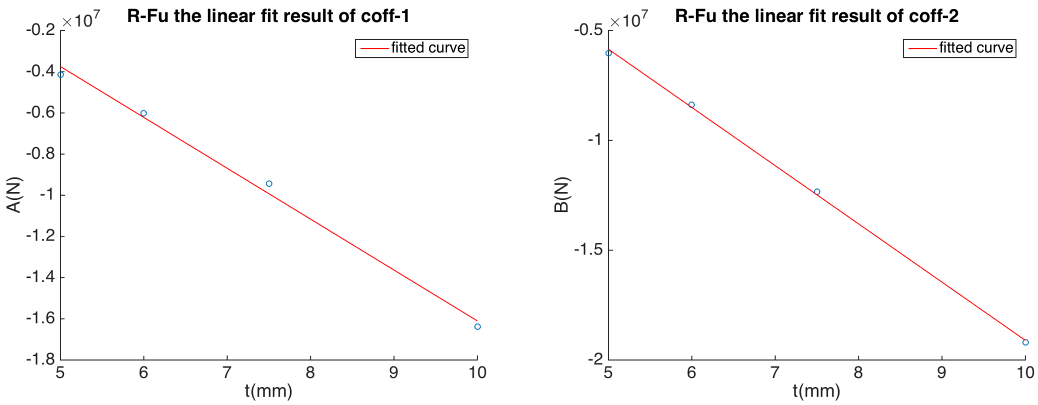

Figure A.2: example:curve fitting results on coefficients $A(t)$ and $B(t)$

$$\begin{cases} A(t) = (-2.471 \cdot t + 8.609) \times 10^6 \\ B(t) = (-2.652 \cdot t + 7.410) \times 10^6 \end{cases} \tag{A.2}$$

7. **Form General Formula** Combining the two phased of curve fitting results, it is able to form a general formula.

example: According to the coefficient formulas and the estimated formula shape, the general formula is formed in eq A.3.

$$\begin{aligned} F_u(t, \frac{R_m}{R_k}) &= A(t) \cdot \log(\frac{R_m}{R_k}) + B(t) \\ &= (-2.471 \cdot t + 8.609) \times 10^6 \cdot \log(\frac{R_m}{R_k}) + (-2.652 \cdot t + 7.410) \times 10^6 \end{aligned} \tag{A.3}$$

Table A.3: Data:radius ratio($\frac{R_m}{R_k}$) and ultimate reaction force (F_u)

	F_u			
$\frac{R_m}{R_k}$	$t = 5$	$t = 6$	$t = 7.5$	$t = 10$
0.099534248	4154721.037	6141547.854	10269279.82	20148843.89
0.093245837	4258562.237	6454869.377	10662025.83	20613553.45
0.087467513	4385407.876	6914232.524	11433819.21	21201250.23
0.08222455	4563871.192	7058383.779	11719116.37	21957582.33
0.077488525	4782224.916	7228606.651	11994327.22	22856246.51
0.073212665	5029263.288	7440854.338	12311108.21	23857874.06
0.069346631	5130823.303	7694051.754	12673653.51	24921831.38
0.064212511	5302785.119	8134034.536	13287686.3	33410096.51
0.059752415	5505562.739	8483666.671	13959452.05	40863533.65
0.055850236	5735345.959	8803723.95	14677158.36	46387948.36
0.052412355	5984666.131	9311392.535	15101576.85	50459623.32
0.049363546	6246175.651	9510834.888	15569507.35	53538302.03
0.046643189	6505890.816	9722150.939	16070001.5	53241066.7
0.04420216	6650215.059	9945966.916	16592779.66	54368886.95
0.042000375	6807997.403	10180825.11	17129714.32	26152880.47
0.040004882	6976632.671	10424719.9	17565082.36	26863603.54
0.038188395	7153501.822	10675250.97	17965706.68	27603976.36
0.038188395	7153539.263	10675124.45	17965706.63	28381800.59
0.026233375	8879022.917	13190904.27	21700961.87	29191675.6
0.019964901	10196515.06	15304786.71	24666379.47	30024100.04
0.016110957	11265049.59	16963908.4	26939289.66	30869740.08
0.013503012	12124048.28	18268797.28	28701902.02	31719327.42
0.011621275	12820261.2	18781249.09	30092396.38	32568953.73
0.010199629	13393109.97	19340190.15	31223530.4	33410096.5

APPENDIX B

An example of the modal displacement track (modal decomposition)

In Koiter theory, he supposed an idea to estimate the post-buckling performance with the model intrinsic information, as the modal shape and the load condition. And the modal displacement is purposed in his thesis. It is similar with the idea of the Modal Decomposition in dynamic analysis. Since the modal shape is orthogonal with each others, it is possible to decompose the model deformation as a serious of modal shapes. In this document, it is aimed to illustrate **how to decompose the deformation in each steps and track the model buckling process in the modal displacement system**. It is helpful to observe how the initial imperfection influence on the buckling development.

1. **Post-process and export the result** To observe the buckling process in modal displacement, it is based on two part: 1).decompose the deformation into modal displacement 2).track the modal interaction factor with the load steps. Therefore, in FEM software, the modal shapes information and the deformation at every step are exported. The deformation result of one step is stored as the vector component. There is n dofs in system, hence $\boldsymbol{d}$ is a $n \times 1$ vector.

$$\boldsymbol{d} = \begin{pmatrix} d_1 \\ d_2 \\ \vdots \\ d_n \end{pmatrix}_{n\times 1}$$

To decompose the deformation in first k orders of the buckling modal shapes, the radial deformation each mode is expressed in a vector $\boldsymbol{m_1}$,$\boldsymbol{m_2}$...$\boldsymbol{m_k}$. The modal vector $\boldsymbol{m_{i=1\cdots k}}$ are the $n \times 1$ vectors as well, n is the number of dofs, k is the number of the fundamental modal shapes.

$$\boldsymbol{M} = [\boldsymbol{m_1}, \boldsymbol{m_2}, \cdots \boldsymbol{m_k}]$$

$$\boldsymbol{m_1} = \begin{pmatrix} m_{11} \\ m_{21} \\ \vdots \\ m_{n1} \end{pmatrix}_{n\times 1} ,\boldsymbol{m_2} = \begin{pmatrix} m_{12} \\ m_{22} \\ \vdots \\ m_{n2} \end{pmatrix}_{n\times 1} \cdots \boldsymbol{m_k} = \begin{pmatrix} m_{1k} \\ m_{2k} \\ \vdots \\ m_{n5} \end{pmatrix}_{n\times 1}$$

example: The buckling process under GNLBA on hyperboloid model implemented with the 1^{st} buckling modal is monitored. It is aimed to track its deformation with first 10 modal shapes. To simplify the analysis, only the radial deformation is investigated. The first step of the radial deformation is exported to the vector d_1.

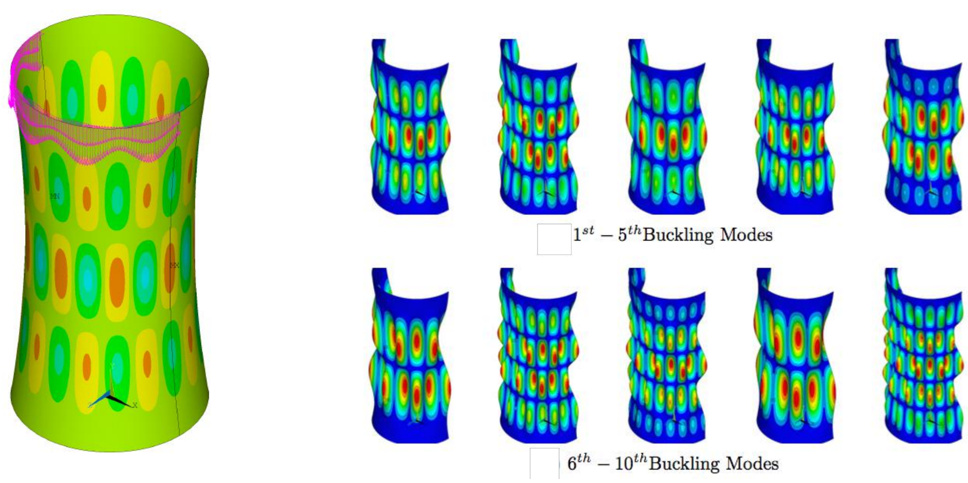

(a) deformed model (b) fundamental modal shapes

Figure B.1: Deformed model and fundamental modal shapes

2. **Decompose the Deformation Vector** In this step, the deformation vector is decomposed to a series of modal shapes by the components proportions(p_i). The proportion vector ($\boldsymbol{p}$) is composed by p_i. The relation between the modal decomposition is expressed by eq B.1. Since the modal shape has already been normalized without unit, the proportion factor p_i just expresses the extent of the modal activated into the specified deformation and in mm dimension.

$$\begin{aligned} \boldsymbol{d_1} = \sum_{i=1}^{k} p_i \cdot \boldsymbol{m_i} = p_1 \cdot \boldsymbol{m_1} + p_2 \cdot \boldsymbol{m_2} \cdots + p_k \cdot \boldsymbol{m_k} \\ \boldsymbol{p_1} = \begin{pmatrix} p_{11} \\ p_{21} \\ \vdots \\ p_{n1} \end{pmatrix}_{n \times 1} \end{aligned} \tag{B.1}$$

if the eq B.1 is written into the matrix calculation, it is like eq B.2.

$$\begin{aligned} \boldsymbol{d} = \boldsymbol{M} \cdot \boldsymbol{p} &= \begin{pmatrix} m_{11} & m_{12} & \cdots & m_{1k} \\ m_{21} & \ddots & \cdots & m_{2k} \\ \vdots & \vdots & \ddots & \vdots \\ m_{n1} & m_{n2} & \cdots & m_{nk} \end{pmatrix} \cdot \begin{pmatrix} p_1 \\ p_2 \\ \vdots \\ p_k \end{pmatrix} \\ &= \begin{pmatrix} p_1 \cdot m_{11} + p_2 \cdot m_{12} \cdots + p_k \cdot m_{1k} \\ p_1 \cdot m_{21} + p_2 \cdot m_{22} \cdots + p_k \cdot m_{2k} \\ \vdots \\ p_1 \cdot m_{n1} + p_2 \cdot m_{n2} \cdots + p_k \cdot m_{nk} \end{pmatrix} \end{aligned} \tag{B.2}$$

The possibility to decompose the deformation into modal matrix is based on the orthogonality between the modal vectors, which is verified by the eigenvalue problem, solved in linear buckling analysis. And about the method to solve the Overdetermined Linear Equations($n > k$) based on the Least Square is also beyond this thesis, the math package provided by matlab is applied directly.

It is noted that for the restraint dofs, it is the zero components in matrix, the correspondent arrow should be removed in both of the modal matrix and the deformation vector.

$$\boldsymbol{p} = \boldsymbol{M}/\boldsymbol{d} \tag{B.3}$$

After the $\boldsymbol{p}$ is solved, the proportions of each modal component are obtained.

example: In this step, the deformation is decomposed to first 10 fundamental modal shapes in eq B.4.

$$\boldsymbol{d_1} = \sum_{i=1}^{10} p_i \cdot \boldsymbol{m_i} = p_1 \cdot \boldsymbol{m_1} + p_2 \cdot \boldsymbol{m_2} \cdots + p_{10} \cdot \boldsymbol{m_{10}} \tag{B.4}$$

With the matrix calculation, the proportion factors of the modal shapes are solved. The first step deformation is successfully expressed by these modal shapes.

$$\boldsymbol{p} = \begin{pmatrix} 0.005 \\ 5.27 \times 10^{-10} \\ 5.88 \times 10^{-08} \\ -1.03 \times 10^{-06} \\ -9.64 \times 10^{-11} \\ 6.85 \times 10^{-10} \\ 1.87 \times 10^{-10} \\ 4.23 \times 10^{-09} \\ 1.77 \times 10^{-10} \\ -8.47 \times 10^{-07} \end{pmatrix} (mm) \tag{B.5}$$

3. **Track Load Steps**

The previous step explains the method to decompose only one load step deformation. To track the GNLBA results, it is necessary to calculate the proportion vector in every load step. The external loop is possible to solve the problem, but the more efficient way is to utilize the matrix calculation. The deformation vector and the proportion vector are expanded to correspondent matrix including all the load steps.

$$\begin{aligned} \boldsymbol{D} &= [\boldsymbol{d_1}, \boldsymbol{d_2}, \cdots \boldsymbol{d_l}] \\ &= \begin{pmatrix} d_{11} & d_{12} & \cdots & d_{1l} \\ d_{21} & \ddots & \cdots & d_{2l} \\ \vdots & \vdots & \ddots & \vdots \\ d_{n1} & d_{n2} & \cdots & d_{nl} \end{pmatrix} \end{aligned} \qquad \begin{aligned} \boldsymbol{P} &= [\boldsymbol{p_1}, \boldsymbol{p_2}, \cdots \boldsymbol{p_l}] \\ &= \begin{pmatrix} p_{11} & p_{12} & \cdots & p_{1l} \\ p_{21} & \ddots & \cdots & p_{2l} \\ \vdots & \vdots & \ddots & \vdots \\ p_{n1} & p_{n2} & \cdots & p_{nl} \end{pmatrix} \end{aligned}$$

,in which n means the number of the dofs and the l means the total load step

The matrix equation is expended to eq B.6 as well. The proportion matrix($\boldsymbol{P}$) is able to solved. Each proportion vector($\boldsymbol{p}_i$) in $\boldsymbol{P}$ indicates the modal proportion at that load step.

$$\boldsymbol{D} = \boldsymbol{M} \cdot \boldsymbol{P} \tag{B.6}$$

example: The successive load steps are decomposed by the matrix calculation in eq B.6. Since there are 44 steps in the nonlinear analysis decomposed into 10 fundamental modal shapes, the solved $\boldsymbol{P}$ is a 10×44 matrix.(Matrix $\boldsymbol{P}$ is placed at the end.)

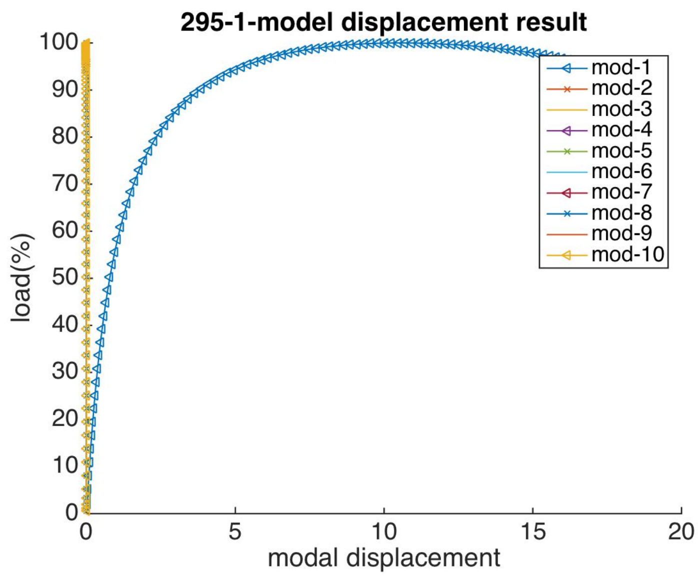

Figure B.2: Modal displacement for the modal implemented with the 1_{st} modal shape

Each arrow of the P means the activated extent of the one modal. In fig B.2, the first 10 fundamental modal displacements is plotted. It is evident that the model implemented with the 1^{st} buckling modal at $\delta_{imp} = 0.2t$, only the 1^{st} modal is activated and the others are silence.

Attachment: Matrix $\boldsymbol{P}^T$

Matrix $\boldsymbol{P}^T$ is written following table. In each arrow, it is the fundamental proportion factors in each load step. Each column contains a proportion factor of a fundamental modal shape, which is the modal displacement. Before the buckling happens, the absolute value in each column is increasing which indicates the deformation developing.

Mod-1	Mod-2	Mod-3	Mod-4	Mod-5	Mod-6	Mod-7	Mod-8	Mod-9	Mod-10
5.02E-03	5.27E-10	5.88E-08	-1.03E-06	-9.64E-11	6.86E-10	1.88E-10	4.24E-09	1.77E-10	-7.47E-07
1.01E-02	8.96E-11	1.14E-07	-2.07E-06	3.01E-11	4.87E-10	6.59E-11	8.36E-09	2.22E-10	-1.50E-06
1.78E-02	-1.37E-10	1.90E-07	-3.61E-06	2.72E-11	2.26E-11	-1.67E-10	1.55E-08	-4.56E-10	-2.64E-06
2.96E-02	1.17E-09	2.85E-07	-5.91E-06	1.43E-10	1.56E-09	-2.67E-10	2.80E-08	-1.14E-09	-4.36E-06
4.77E-02	1.46E-09	3.88E-07	-9.35E-06	1.17E-10	1.83E-09	-1.78E-10	4.74E-08	-9.12E-10	-6.98E-06
7.59E-02	1.56E-09	4.40E-07	-1.44E-05	-5.39E-11	2.31E-09	3.62E-10	8.02E-08	-1.91E-11	-1.10E-05
1.05E-01	1.32E-09	3.66E-07	-1.93E-05	-2.06E-11	2.32E-09	1.91E-10	1.21E-07	4.45E-10	-1.51E-05
1.37E-01	7.16E-10	1.49E-07	-2.42E-05	-6.80E-11	1.76E-09	-7.02E-11	1.71E-07	5.15E-10	-1.94E-05
1.70E-01	-3.04E-09	-2.34E-07	-2.90E-05	4.28E-09	-9.90E-09	-5.82E-09	2.24E-07	-1.53E-08	-2.39E-05
2.05E-01	9.54E-10	-7.84E-07	-3.36E-05	-7.03E-11	2.05E-09	3.37E-10	2.98E-07	8.80E-10	-2.85E-05
2.42E-01	1.45E-09	-1.54E-06	-3.82E-05	-2.02E-11	2.43E-09	-8.63E-11	3.82E-07	-7.99E-11	-3.33E-05
2.81E-01	2.05E-09	-2.52E-06	-4.26E-05	-2.55E-10	3.08E-09	-6.39E-10	4.86E-07	-7.81E-10	-3.84E-05
3.23E-01	1.85E-09	-3.75E-06	-4.69E-05	-3.64E-10	2.85E-09	-2.15E-10	6.07E-07	-1.42E-10	-4.38E-05
3.68E-01	1.76E-09	-5.27E-06	-5.10E-05	1.14E-09	9.08E-10	6.91E-10	7.51E-07	-5.54E-10	-4.95E-05
4.16E-01	1.40E-09	-7.12E-06	-5.49E-05	-3.32E-11	2.60E-09	-1.62E-10	9.28E-07	6.37E-10	-5.55E-05

4.67E-01	6.02E-10	-9.34E-06	-5.86E-05	-8.14E-11	1.96E-09	-8.52E-11	1.14E-06	5.83E-10	-6.19E-05
5.21E-01	1.20E-09	-1.20E-05	-6.21E-05	-8.16E-11	2.31E-09	-1.10E-10	1.40E-06	6.79E-10	-6.87E-05
5.80E-01	-9.20E-10	-1.51E-05	-6.52E-05	-2.64E-09	-2.81E-09	2.06E-09	1.70E-06	3.52E-09	-7.60E-05
6.42E-01	-5.65E-10	-1.88E-05	-6.81E-05	-2.89E-09	-2.79E-09	1.92E-09	2.08E-06	3.37E-09	-8.40E-05
7.10E-01	-8.72E-10	-2.31E-05	-7.05E-05	-3.26E-09	-3.33E-09	2.02E-09	2.54E-06	3.48E-09	-9.26E-05
7.83E-01	-8.11E-10	-2.81E-05	-7.26E-05	-3.82E-09	-4.20E-09	2.99E-09	3.10E-06	7.19E-09	-1.02E-04
8.61E-01	-1.49E-09	-3.40E-05	-7.41E-05	-3.94E-09	-4.86E-09	3.38E-09	3.78E-06	7.39E-09	-1.12E-04
9.46E-01	-1.11E-09	-4.09E-05	-7.50E-05	-4.28E-09	-4.49E-09	3.72E-09	4.62E-06	7.76E-09	-1.23E-04
1.04E+00	-1.01E-09	-4.89E-05	-7.53E-05	-4.40E-09	-4.66E-09	3.89E-09	5.65E-06	8.15E-09	-1.36E-04
1.14E+00	-1.26E-09	-5.82E-05	-7.49E-05	-4.62E-09	-5.08E-09	4.01E-09	6.93E-06	8.20E-09	-1.50E-04
1.24E+00	-7.01E-10	-6.90E-05	-7.35E-05	-5.04E-09	-4.77E-09	4.84E-09	8.50E-06	9.08E-09	-1.65E-04
1.36E+00	-1.67E-09	-8.14E-05	-7.12E-05	-5.13E-09	-5.92E-09	4.48E-09	1.04E-05	9.21E-09	-1.82E-04
1.49E+00	-1.91E-09	-9.58E-05	-6.77E-05	-5.41E-09	-6.26E-09	4.85E-09	1.28E-05	9.52E-09	-2.01E-04
1.62E+00	-1.87E-09	-1.12E-04	-6.29E-05	-5.86E-09	-6.69E-09	4.98E-09	1.58E-05	1.00E-08	-2.22E-04
1.76E+00	-2.22E-09	-1.31E-04	-5.67E-05	-6.06E-09	-6.98E-09	5.49E-09	1.94E-05	1.04E-08	-2.46E-04
1.92E+00	-2.34E-09	-1.53E-04	-4.90E-05	-6.14E-09	-7.47E-09	5.53E-09	2.38E-05	1.06E-08	-2.72E-04
2.08E+00	-2.44E-09	-1.77E-04	-3.95E-05	-6.50E-09	-7.90E-09	5.60E-09	2.92E-05	1.13E-08	-3.01E-04
2.25E+00	-2.54E-09	-2.05E-04	-2.83E-05	-6.87E-09	-8.45E-09	5.86E-09	3.57E-05	1.16E-08	-3.34E-04
2.43E+00	-2.80E-09	-2.35E-04	-1.53E-05	-7.07E-09	-8.46E-09	6.35E-09	4.35E-05	1.23E-08	-3.69E-04
2.62E+00	-2.97E-09	-2.69E-04	-2.60E-07	-7.60E-09	-9.04E-09	6.30E-09	5.27E-05	1.25E-08	-4.08E-04
2.82E+00	-3.21E-09	-3.06E-04	1.67E-05	-7.68E-09	-9.17E-09	6.67E-09	6.36E-05	1.29E-08	-4.50E-04
3.02E+00	-3.18E-09	-3.47E-04	3.56E-05	-8.33E-09	-9.35E-09	7.37E-09	7.62E-05	1.40E-08	-4.95E-04
3.22E+00	-3.27E-09	-3.90E-04	5.65E-05	-8.86E-09	-9.70E-09	7.62E-09	9.08E-05	1.43E-08	-5.44E-04
3.43E+00	-3.22E-09	-4.37E-04	7.93E-05	-9.10E-09	-9.62E-09	7.74E-09	1.08E-04	1.45E-08	-5.96E-04
3.65E+00	-3.33E-09	-4.88E-04	1.04E-04	-9.70E-09	-9.58E-09	7.86E-09	1.27E-04	1.45E-08	-6.52E-04
3.86E+00	-3.24E-09	-5.42E-04	1.31E-04	-1.00E-08	-1.03E-08	8.05E-09	1.48E-04	1.54E-08	-7.11E-04
4.08E+00	-3.74E-09	-5.99E-04	1.59E-04	-1.06E-08	-1.04E-08	8.92E-09	1.72E-04	1.56E-08	-7.73E-04
4.30E+00	-3.84E-09	-6.59E-04	1.90E-04	-1.03E-08	-1.10E-08	9.15E-09	1.99E-04	1.61E-08	-8.39E-04
4.53E+00	-3.79E-09	-7.23E-04	2.22E-04	-1.10E-08	-1.17E-08	8.72E-09	2.29E-04	1.68E-08	-9.07E-04
4.75E+00	-3.80E-09	-7.90E-04	2.56E-04	-1.10E-08	-1.10E-08	9.07E-09	2.62E-04	1.67E-08	-9.79E-04
4.98E+00	-4.15E-09	-8.60E-04	2.92E-04	-1.14E-08	-1.14E-08	9.70E-09	2.98E-04	1.70E-08	-1.05E-03
5.20E+00	-4.04E-09	-9.33E-04	3.29E-04	-1.16E-08	-1.18E-08	9.15E-09	3.37E-04	1.74E-08	-1.13E-03
5.43E+00	-4.04E-09	-1.01E-03	3.68E-04	-1.21E-08	-1.22E-08	9.33E-09	3.81E-04	1.76E-08	-1.21E-03
5.66E+00	-4.16E-09	-1.09E-03	4.10E-04	-1.24E-08	-1.21E-08	9.57E-09	4.27E-04	1.77E-08	-1.30E-03
5.89E+00	-3.98E-09	-1.17E-03	4.52E-04	-1.23E-08	-1.21E-08	9.82E-09	4.78E-04	1.79E-08	-1.39E-03
6.12E+00	-4.30E-09	-1.26E-03	4.97E-04	-1.24E-08	-1.23E-08	1.01E-08	5.33E-04	1.79E-08	-1.48E-03
6.35E+00	-3.81E-09	-1.35E-03	5.43E-04	-1.32E-08	-1.30E-08	1.03E-08	5.92E-04	1.82E-08	-1.57E-03
6.57E+00	-4.43E-09	-1.44E-03	5.92E-04	-1.31E-08	-1.28E-08	9.99E-09	6.56E-04	1.85E-08	-1.67E-03
6.80E+00	-3.96E-09	-1.54E-03	6.42E-04	-1.32E-08	-1.30E-08	1.04E-08	7.24E-04	1.85E-08	-1.77E-03
7.03E+00	-3.89E-09	-1.63E-03	6.93E-04	-1.40E-08	-1.29E-08	1.07E-08	7.97E-04	1.83E-08	-1.87E-03
7.26E+00	-3.76E-09	-1.74E-03	7.47E-04	-1.48E-08	-1.30E-08	1.05E-08	8.75E-04	1.90E-08	-1.98E-03
7.50E+00	-4.09E-09	-1.84E-03	8.02E-04	-1.48E-08	-1.42E-08	1.10E-08	9.57E-04	1.90E-08	-2.09E-03
7.73E+00	-4.71E-09	-1.95E-03	8.59E-04	-1.48E-08	-1.39E-08	1.11E-08	1.05E-03	1.93E-08	-2.20E-03
7.96E+00	-4.26E-09	-2.06E-03	9.18E-04	-1.54E-08	-1.38E-08	1.08E-08	1.14E-03	1.89E-08	-2.31E-03
8.19E+00	-4.94E-09	-2.18E-03	9.79E-04	-1.54E-08	-1.40E-08	1.09E-08	1.24E-03	1.89E-08	-2.43E-03
8.42E+00	-4.61E-09	-2.29E-03	1.04E-03	-1.58E-08	-1.50E-08	1.13E-08	1.34E-03	1.99E-08	-2.55E-03
8.65E+00	-4.19E-09	-2.42E-03	1.11E-03	-1.59E-08	-1.51E-08	1.11E-08	1.46E-03	1.94E-08	-2.68E-03
8.87E+00	-4.23E-09	-2.54E-03	1.17E-03	-1.63E-08	-1.44E-08	1.12E-08	1.57E-03	1.97E-08	-2.81E-03
9.10E+00	-3.75E-09	-2.67E-03	1.24E-03	-1.67E-08	-1.40E-08	1.05E-08	1.70E-03	1.95E-08	-2.94E-03
9.33E+00	-3.47E-09	-2.80E-03	1.31E-03	-1.70E-08	-1.44E-08	1.06E-08	1.83E-03	1.94E-08	-3.07E-03
9.56E+00	-4.23E-09	-2.94E-03	1.38E-03	-1.68E-08	-1.43E-08	1.15E-08	1.97E-03	2.00E-08	-3.20E-03
9.79E+00	-3.36E-09	-3.08E-03	1.46E-03	-1.71E-08	-1.44E-08	1.06E-08	2.11E-03	1.96E-08	-3.34E-03
1.00E+01	-3.14E-09	-3.22E-03	1.53E-03	-1.76E-08	-1.36E-08	1.08E-08	2.26E-03	1.95E-08	-3.48E-03
1.02E+01	-3.08E-09	-3.36E-03	1.61E-03	-1.75E-08	-1.35E-08	1.10E-08	2.42E-03	1.93E-08	-3.63E-03
1.05E+01	-2.39E-09	-3.51E-03	1.69E-03	-1.72E-08	-1.35E-08	1.04E-08	2.59E-03	1.94E-08	-3.78E-03
1.07E+01	-2.14E-09	-3.67E-03	1.78E-03	-1.81E-08	-1.34E-08	1.08E-08	2.77E-03	1.91E-08	-3.93E-03
1.09E+01	-2.34E-09	-3.82E-03	1.86E-03	-1.87E-08	-1.33E-08	1.00E-08	2.95E-03	1.92E-08	-4.08E-03

1.12E+01	-1.98E-09	-3.98E-03	1.95E-03	-1.85E-08	-1.33E-08	1.05E-08	3.14E-03	1.92E-08	-4.24E-03
1.14E+01	-2.13E-09	-4.15E-03	2.04E-03	-1.87E-08	-1.30E-08	1.04E-08	3.34E-03	1.89E-08	-4.40E-03
1.16E+01	-2.02E-09	-4.32E-03	2.13E-03	-1.88E-08	-1.29E-08	1.05E-08	3.56E-03	1.89E-08	-4.56E-03
1.18E+01	-2.26E-09	-4.49E-03	2.23E-03	-1.95E-08	-1.32E-08	1.08E-08	3.78E-03	1.89E-08	-4.73E-03
1.21E+01	-1.40E-09	-4.67E-03	2.32E-03	-1.90E-08	-1.27E-08	9.62E-09	4.01E-03	1.91E-08	-4.89E-03
1.23E+01	-1.28E-09	-4.85E-03	2.42E-03	-1.95E-08	-1.27E-08	1.04E-08	4.25E-03	1.89E-08	-5.07E-03
1.25E+01	-1.84E-09	-5.03E-03	2.53E-03	-1.97E-08	-1.26E-08	1.02E-08	4.50E-03	1.86E-08	-5.24E-03
1.27E+01	-1.46E-09	-5.22E-03	2.63E-03	-1.98E-08	-1.27E-08	9.92E-09	4.76E-03	1.83E-08	-5.42E-03
1.30E+01	-1.79E-09	-5.42E-03	2.74E-03	-2.03E-08	-1.20E-08	1.00E-08	5.03E-03	1.81E-08	-5.60E-03
1.32E+01	-1.29E-09	-5.62E-03	2.86E-03	-2.00E-08	-1.21E-08	9.74E-09	5.32E-03	1.83E-08	-5.79E-03
1.34E+01	-1.60E-09	-5.82E-03	2.97E-03	-2.05E-08	-1.21E-08	9.13E-09	5.62E-03	1.82E-08	-5.97E-03
1.36E+01	-9.73E-10	-6.04E-03	3.09E-03	-2.05E-08	-1.18E-08	9.70E-09	5.93E-03	1.78E-08	-6.17E-03
1.38E+01	-7.66E-11	-6.25E-03	3.22E-03	-2.04E-08	-1.24E-08	9.73E-09	6.25E-03	1.83E-08	-6.36E-03
1.41E+01	-1.32E-09	-6.47E-03	3.35E-03	-2.13E-08	-1.16E-08	1.00E-08	6.59E-03	1.77E-08	-6.56E-03
1.43E+01	-7.53E-10	-6.70E-03	3.48E-03	-2.17E-08	-1.15E-08	9.47E-09	6.95E-03	1.79E-08	-6.77E-03
1.45E+01	-5.62E-10	-6.94E-03	3.63E-03	-2.24E-08	-1.25E-08	9.92E-09	7.32E-03	1.88E-08	-6.98E-03
1.47E+01	-1.01E-09	-7.18E-03	3.77E-03	-2.22E-08	-1.14E-08	9.10E-09	7.71E-03	1.72E-08	-7.19E-03
1.49E+01	-6.49E-10	-7.43E-03	3.93E-03	-2.13E-08	-1.13E-08	8.85E-09	8.12E-03	1.68E-08	-7.41E-03
1.52E+01	-5.43E-10	-7.70E-03	4.09E-03	-2.18E-08	-1.19E-08	8.85E-09	8.54E-03	1.80E-08	-7.64E-03
1.54E+01	-4.14E-10	-7.97E-03	4.26E-03	-2.23E-08	-1.16E-08	8.55E-09	8.99E-03	1.69E-08	-7.87E-03
1.56E+01	-3.32E-12	-8.25E-03	4.44E-03	-2.20E-08	-1.11E-08	7.93E-09	9.47E-03	1.70E-08	-8.11E-03
1.58E+01	4.28E-10	-8.55E-03	4.64E-03	-2.25E-08	-1.12E-08	9.52E-09	9.98E-03	1.70E-08	-8.36E-03
1.60E+01	-8.34E-11	-8.86E-03	4.85E-03	-2.35E-08	-1.07E-08	9.71E-09	1.05E-02	1.69E-08	-8.63E-03
1.62E+01	1.36E-09	-9.19E-03	5.08E-03	-2.36E-08	-1.15E-08	8.90E-09	1.11E-02	1.68E-08	-8.90E-03
1.64E+01	1.06E-09	-9.55E-03	5.33E-03	-2.42E-08	-1.06E-08	8.81E-09	1.17E-02	1.61E-08	-9.20E-03
1.66E+01	2.69E-10	-9.93E-03	5.61E-03	-2.37E-08	-1.07E-08	8.06E-09	1.24E-02	1.61E-08	-9.51E-03

APPENDIX C

Research Flowchart

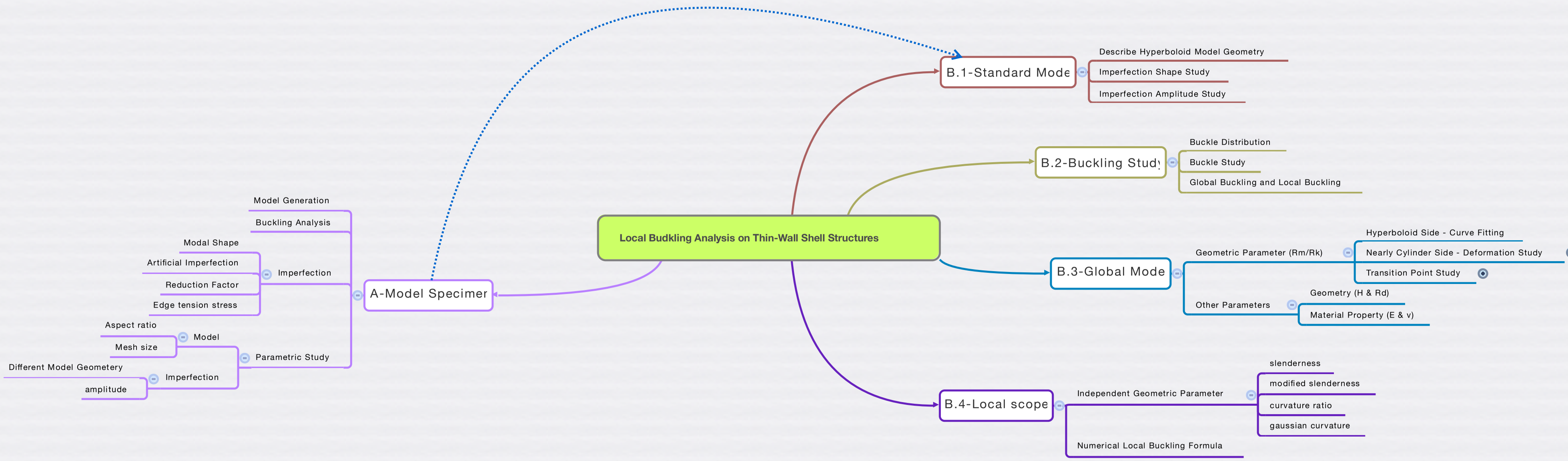
Local Budkling Analysis on Thin-Wall Shell Structures
A-Model Specimer
Model Generation
Buckling Analysis
Imperfection
Modal Shape
Artificial Imperfection
Reduction Factor
Edge tension stress
Parametric Study
Model
Aspect ratio
Mesh size
Imperfection
Different Model Geometery
amplitude
B.1-Standard Mode
Describe Hyperboloid Model Geometry
Imperfection Shape Study
Imperfection Amplitude Study
B.2-Buckling Stud
Buckle Distribution
Buckle Study
Global Buckling and Local Buckling
B.3-Global Mode
Geometric Parameter (Rm/Rk)
Hyperboloid Side - Curve Fitting
Nearly Cylinder Side - Deformation Study
Transition Point Study
Other Parameters
Geometry (H & Rd)
Material Property (E & v)
B.4-Local scope
Independent Geometric Parameter
slenderness
modified slenderness
curvature ratio
gaussian curvature
Numerical Local Buckling Formula

APPENDIX D

Test Model Input Table

In order to investigate the relation between ultimate reaction force Fu and vertical radius R_k, under different geometric parameters, the standard model set is established. In the standard model set, the R_k varies from $8000mm - 3,500,000mm$(50 models), and the detailed groups are listed in table D.1. The other parameters includes the different thickness, edge radius, height and material properties are changed from the standard test set.

Table D.1: A set of the test groups with respective R_k

Group 1	8,000mm-12,000mm
Group 2	12,000mm-33,000mm
Group 3	33,000mm-60,000mm
Group 4	60,000mm-330,000mm
Group 5	330,000mm-3,500,000mm
note:	each group 10 model samples, totally 50 models

To investigate the different geometric conditions, there are 14 test sets are designed in table D.2, each group contains 50 models. Hence, in total $14 \times 50 = 700$ specimens are tested with GNLBA. The results are collected into the database to proceed details numerical analysis.

Table D.2: Tested model plan

Test Set No.	R_k(mm)	t(mm)	Rd(mm)	H(mm)	E(MPa)	ν	δ_{imp}
1(standard set)	8000-3,500,000	5	2500	10000	210000	0.3	0.2t
2	8000-3,500,000	***5.5***	2500	10000	210000	0.3	0.2t
3	8000-3,500,000	***6***	2500	10000	210000	0.3	0.2t
4	8000-3,500,000	***7.5***	2500	10000	210000	0.3	0.2t
5	8000-3,500,000	***9***	2500	10000	210000	0.3	0.2t
6	8000-3,500,000	***10***	2500	10000	210000	0.3	0.2t
7	8000-3,500,000	5	***1500***	10000	210000	0.3	0.2t
8	8000-3,500,000	5	***3000***	10000	210000	0.3	0.2t
9	8000-3,500,000	5	***4000***	10000	210000	0.3	0.2t
10	8000-3,500,000	5	***5000***	10000	210000	0.3	0.2t
11	8000-3,500,000	5	2500	***7500***	210000	0.3	0.2t
12	8000-3,500,000	5	2500	***12000***	210000	0.3	0.2t
13	8000-3,500,000	5	2500	10000	***105000***	0.3	0.2t
14	8000-3,500,000	5	2500	10000	210000	***0.15***	0.2t

APPENDIX E

APDL script and input

The APDL script is described in this appendix, for detailed input parameters are introduced. The finite element model is generated in parametric method, people can adjust the model by their own requirements. All three kinds of the geometries are covered, four types of imperfection are implemented, and both the Newton-Raphson and Arc-length method are optioned. In script, it is possible to develop more imperfection type by user. And the standard results includes the graphs, deformation plots and the results in txt files. They are able to be imported by the numerical analysis software, including Excel, Matlab, Python and etc.

The other part contains all the input data of the nonlinear tests in this research. It will help people to check and reproduce the test results in this results. The test is operated in batch, each test group contains 10 test models, most of the input data could be set as a variable, and the test could terminate automatically. It is easy to perform more nonlinear test groups.

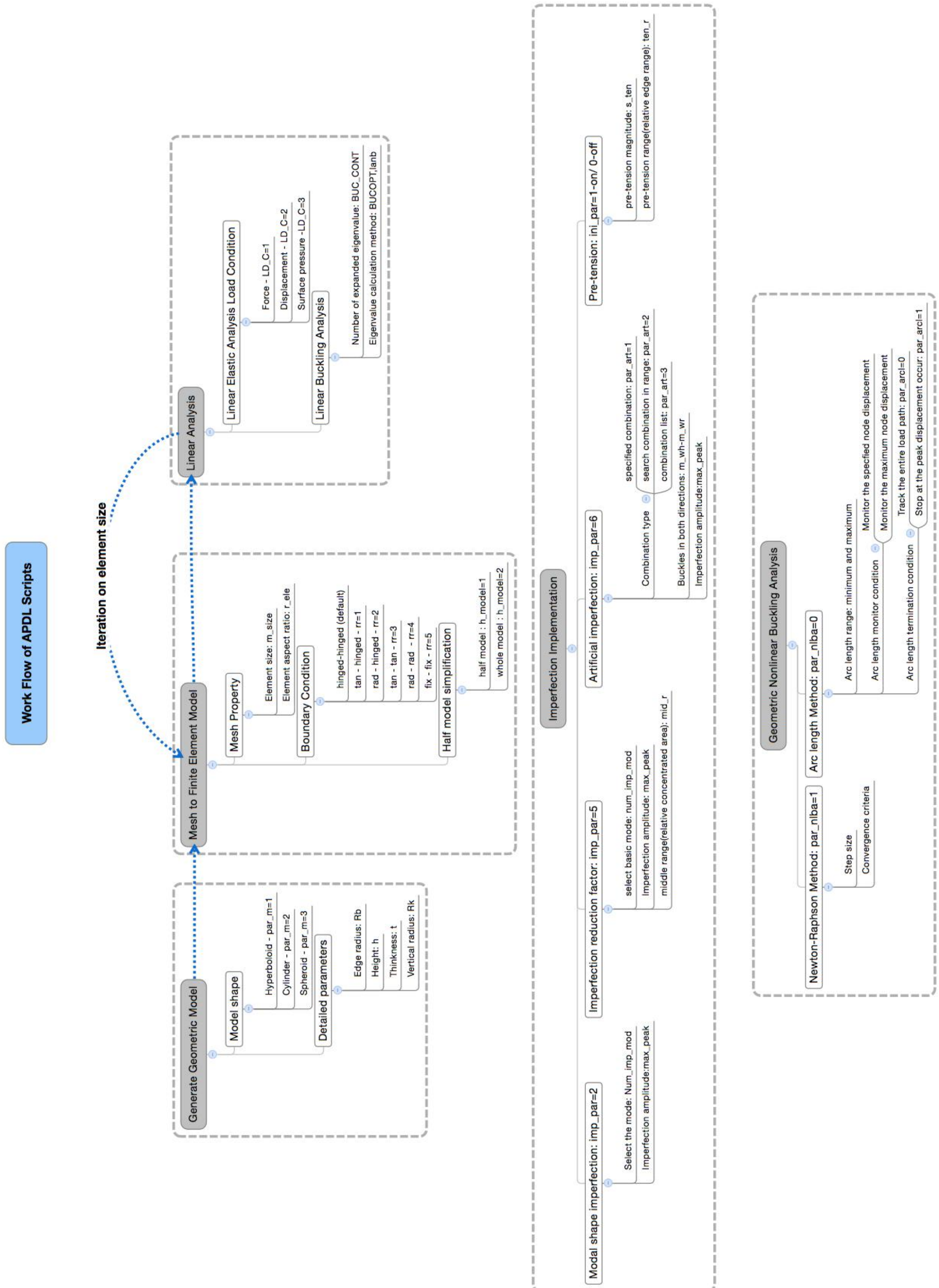
Work Flow of APDL Scripts
Iteration on element size
Generate Geometric Model
Model shape
Hyperboloid - par_m=1
Cylinder - par_m=2
Spheroid - par_m=3
Detailed parameters
Edge radius: Rb
Height: h
Thinkness: t
Vertical radius: Rk
Mesh to Finite Element Model
Mesh Property
Element size: m_size
Element aspect ratio: r_ele
Boundary Condition
hinged-hinged (default)
tan - hinged - rr=1
rad - hinged - rr=2
tan - tan - rr=3
rad - rad - rr=4
fix - fix - rr=5
Half model simplification
half model : h_model=1
whole model : h_model=2
Linear Analysis
Linear Elastic Analysis Load Condition
Force - LD_C=1
Displacement - LD_C=2
Surface pressure -LD_C=3
Linear Buckling Analysis
Number of expanded eigenvalue: BUC_CONT
Eigenvalue calculation method: BUCOPT,lanb
Imperfection Implementation
Modal shape imperfection: imp_par=2
Select the mode: Num_imp_mod
Imperfection amplitude:max_peak
Imperfection reduction factor: imp_par=5
select basic mode: num_imp_mod
Imperfection amplitude: max_peak
middle range(relative concentrated area): mid_r
Artificial imperfection: imp_par=6
Combination type
specified combination: par_art=1
search combination in range: par_art=2
combination list: par_art=3
Buckles in both directions: m_wh-m_wr
Imperfection amplitude:max_peak
Pre-tension: ini_par=1-on/ 0-off
pre-tension magnitude: s_ten
pre-tension range(relative edge range): ten_r
Geometric Nonlinear Buckling Analysis
Newton-Raphson Method: par_nlba=1
Step size
Convergence criteria
Arc length Method: par_nlba=0
Arc length range: minimum and maximum
Arc length monitor condition
Monitor the specfied node displacement
Monitor the maximum node displacement
Arc length termination condition
Track the entire load path: par_arcl=0
Stop at the peak displacement occur: par_arcl=1

Tag	Lp_test	Geometry Parameter						Mesh		Num_eigen	Geometry shape		Pre-tension			Load		NLBA	Imperfection Type	Imperfection(Modal shape)		Imperfection(Reduction Factor)			Imperfection(Artificial)				
		rr=2-imp; rr=3-model	Rb(hori)	H	t0	Rk(vert)	a0-1edge control; 2-mid conrol	msize	r_ele	BUC_CONT	Hyp-1,Cyl-2, Sph-3	half-0; whole-1	ini_par; 1-on;0-off	s_ten(MPa)	ten_r	F-1;Disp-2; Pressure-3	Boundary: rs-1 top-tan;rs-2 top-rad;rs-3 both tan;rs4-both rad ;rs-5 fix	par_arcl; 1-limit;0-entire	2—modal; 5—Reduce; 6—artificial	num_imp_mod	max_peak	num_imp_mod	max_peak	mid_r	max_peak	w_h-w_r	par_art; 1-fixed; 2-range; 3-specified	eh-er	r_pi
	117	2	2500	10000	5	20000	1	66	1.0	50	2-cylinder	0	0			2		0-entire	2-modal	M_1: 1-10	0.5t								
	118	2	2500	10000	10	20000	1	66	1.0	3	2-cylinder	0	0			2		1-entire	2-modal	1	M_1 0.1t-1.0t								
	119	2	2500	10000	5	20000	1	66	1.0	3	2-cylinder	0	0			2		0-entire	2-modal	1	M_1 0.1t-1.0t								
	120	2	2500	10000	10	20000	1	66	1.0	3	2-cylinder	0	0			2		0-entire	2-modal	1	M_1 0.1t-1.0t								
	121	2	2500	10000	10	20000	1	66	1.0	3	2-cylinder	0	0			2		0-entire	6-artificial						M_1: 0.1t-1.0t	0.8-0.2	1	20-20	
	122	2	2500	10000	10	20000	1	66	1.0	3	1-hyper	0	0			2		0-entire	2-modal	1	0.1t-0.5t								
	123	2	2500	10000	10	20000	1	66	1.0	3	2-cylinder	0	0			2		0-entire	2-modal	1	0.1t-0.5t								
	125	2	2500	10000	10	20000	1	66	1.0	20	2-cylinder	0	0			2		0-entire	2-modal	M_1: 1-10	0.5t								
	126	2	2500	10000	10	20000	1	66	1.0	20	3-sph	0	0			2		0-entire	2-modal	M_1: 1-10	0.5t								
rerun	127	2	2500	10000	10	20000	1	66	1.0	10	2-cylinder	0	1	M_1:50-500	0.3	2		0-entire	2-modal	1	0.5t								
rerun	128	2	2500	10000	10	20000	1	66	1.0	1	1-hyper	0	0			2		0-entire	6-artificial						0.5t	0.8-0.2	2	M_1: 5-7range	0.3
	129	2	2500	10000	10			66	1.0	100	2-cylinder	0	0			2		0-entire	2-modal	1	0.5t								
	130	2	2500	10000	10	20000	1	66	1.0	100	1-hyper	0	0			2		0-entire	2-modal	1	0.5t								
	131	2	2500	10000	10	20000	1	66	1.0	100	3-sph	0	0			2		0-entire	2-modal	1	0.5t								
	132	3	2500	M_1:11000-20000	10		1	66	1.0	1	2-cylinder	0	0			2		0-entire	6-artificial						0.5t	0.8-0.2	1	constant wave number in	
	133	3	2500	M_1:11000-20000	10		2	66	1.0	1	1-hyper	0	0			2		0-entire	2-modal	1	0.5t								
	134	2	2500	10000	10	20000	1	66	1.0	10	2-cylinder	0	1	M_1:5-50	0.3	2		0-entire	6-artificial						0.5t	0.8-0.2	1	20-40	
	136	2	2500	10000	10	20000	1	66	1.0	10	3-sph	1	0			2		1-limit	5-Reduce			1	0.5t	1/4					
	137	3	2500	M_1:9500-5000	10	20000	1	66	1.0	1	2-cylinder	0	0			2		2_entire	6-artificial						0.5t	0.8-0.2	1	h0/600-12	
rerun	138	2	2500	10000	10	20000	1	66	1.0	3	2-cylinder	0	1	50	0.3	2		0-entire	2-modal	1	M_1 0.1t-1.0t								
rerun	139	2	M_1:2100-3100	10000	10	20000	2	66	1.0	3	1-hyper	0	0			2		0-entire	2-modal	1	0.5*t								
	140	3	2500	10000	10	20000	2	66	1.0	3	M_1	1	0			2	1	0-entire	2-modal	1	0.5t								
	141	2	2500	10000	10	20000	1	66	1.0	3	3-sph	0	1	50	0.3	2		0-entire	2-modal	1	M_1 0.1t-1.0t								
	142	2	2500	10000	10	20000	1	66	1.0	3	3-sph	0	0			2		1-limit	6-modal						0.5t			20-20	
	143	2	2500	10000	10	20000	1	66	1.0	3	3-sph	0	0			2		1-limit	2-modal	M_1	0.5t								
	144	2	2500	10000	10	20000	1	66	1.0	1	2-cylinder	0	0			2		0-entire	6-artificial						0.5t	0.8-0.2	2	range 20-20	0.1
	145	2	2500	10000	10	20000	1	66	1.0	1	1-hyper	0	0			2		0-entire	6-artificial									range 05-07	0.1
	146																												
	147	2	2500	10000	10	20000	1	66	1.0	1	2-cylinder	0	0																
	148	2	2500	10000	10	20000	1	66	1.0	1	2-cylinder	0	0			2		0-entire	6-artificial						0.5t	0.8-0.2	1	13-28	0.1
	149	2	2500	M_1:5000 – 15000	10	20000	2	66	1.0	3	1-hyper	0	0			2		0-entire	2-modal	1	0.5*t								
	150	2	2500	10000	10	M_1:15000-25000	2	66	1.0	3	1-hyper	0	0			2		0-entire	2-modal	1	0.5*t								
	154																												
3	155	3	2500	10000	5	M_1:12000-30000	1	66	1.0	3	1	0	0			2		1-limit	2-modal	1	0.5t								
	156	2	2500	10000	5	20000	1	66	1.0	20	2-cylinder	0	0			2		0-entire	2-modal	M_1: 1-10	0.2t								
	157																												
6	159	3	2500	10000	5	M_1:60000-330000		66	1.0	3	1-hyper	0	0			2		1-limit	2-modal	1	0.5t								
7	160	3	2500	10000	5	M_1:250000-350000	1	66	1.0	3	1-hyper	0	0			2		1-limit	2-modal	1	0.5t								
4	161	3	2500	10000	5	M_1:33000-60000	1	66	1.0	3	1-hyper	0	0			2		1-limit	2-modal	1	0.5t								
5	162	3	2500	10000	5	M_1:62000-80000	1	66	1.0	3	1-hyper	0	0			2		1-limit	2-modal	1	0.5t								
1	163	3	2500	10000	5	M_1:7200-9000	1	66	1.0	3	1-hyper	0	0			2		1-limit	2-modal	1	0.5t								
2	164	3	2500	10000	5	M_1:10000-15000	1	66	1.0	3	1-hyper	0	0			2		1-limit	2-modal	1	0.5t								
9	165	3	2500	10000	5	M_1:700000-3800000	1	66	1.0	3	1-hyper	0	0			2		1-limit	2-modal	1	0.5t								
8	166	3	2500	10000	5	M_1:370000-500000	1	66	1.0	3	1-hyper	0	0			2		1-limit	2-modal	1	0.5t								
	170	2	2500	10000	5	20000	1	66	1.0		1-hyper	0	0			2		0-entire	2-modal	1	0.1t-0.5t								
	171	2	2500	10000	10	20000	1	66	20		1-hyper	0	0			2		0-entire	2-modal	M_1: 1-10	0.5t								
	172																												
1	173	3	2500	10000	7.5	M_1:9000-12000	1	66	1.0	3	1-hyper	0	0			2		1-limit	2-modal	1	0.5t								
5	174	3	2500	10000	7.5	M_1:700000-3500000	1	66	1.0	3	1-hyper	0	0			2		1-limit	2-modal	1	0.5t								
2	175	3	2500	10000	7.5	M_1:12000-33000	1	66	1.0	3	1-hyper	0	0			2		1-limit	2-modal	1	0.5t								
3	176	3	2500	10000	7.5	M_1:33000-60000	1	66	1.0	3	1-hyper	0	0			2		1-limit	2-modal	1	0.5t								
4	177	3	2500	10000	7.5	M_1:60000-300000	1	66	1.0	3	1-hyper	0	0			2		1-limit	2-modal	1	0.5t								
1	178	3	2500	10000	10	M_1:9000-12000	1	66	1.0	3	1-hyper	0	0			2		1-limit	2-modal	1	0.5t								
5	179	3	2500	10000	10	M_1:700000-3500000	1	66	1.0	3	1-hyper	0	0			2		1-limit	2-modal	1	0.5t								
2	180	3	2500	10000	10	M_1:12000-33000	1	66	1.0	3	1-hyper	0	0			2		1-limit	2-modal	1	0.5t								
3	181	3	2500	10000	10	M_1:33000-60000	1	66	1.0	3	1-hyper	0	0			2		1-limit	2-modal	1	0.5t								
4	182	3	2500	10000	10	M_1:60000-300000	1	66	1.0	3	1-hyper	0	0			2		1-limit	2-modal	1	0.5t								

Tag	Lp_test	Geometry Parameter						Mesh		Num_eigen	Geometry shape		Pre-tension				Load	NLBA	Imperfection Type	Imperfection(Modal shape)		Imperfection(Reduction Factor)			Imperfection(Artificial)				
		rr=2-imp; rr=3-model	Rb(hori)	H	t0	Rk(vert)	a0-1edge control; 2-mid conrol	msize	r_ele	BUC_CONT	Hyp-1,Cyl-2, Sph-3	half-0; whole-1	ini_par; 1-on;0-off	s_ten(MPa)	ten_r	F-1;Disp-2; Pressure-3	Boundary: rs-1 top-tan;rs-2 top-rad;rs-3 both tan;rs4-both rad ;rs-5 fix	par_arcl; 1-limit;0-entire	2—modal; 5—Reduce; 6—artificial	num_imp_mod	max_peak	num_imp_mod	max_peak	mid_r	max_peak	w_h-w_r	par_art; 1-fixed; 2-range; 3-specified	eh-er	r_pi
	185		2500	10000	10	20000	1	66	1.0	3	2-cylinder	0	0			2		0-entire	5-Reduce			7	0.5t	0.4					
1	190	3	2500	10000	7.5	M_1:9000-12000	1	66	1.0	3	1-hyper	0	0			2		1-limit	2-modal	1	0.1t								
5	191	3	2500	10000	7.5	M_1:700000-3500000	1	66	1.0	3	1-hyper	0	0			2		1-limit	2-modal	1	0.1t								
2	192	3	2500	10000	7.5	M_1:12000-33000	1	66	1.0	3	1-hyper	0	0			2		1-limit	2-modal	1	0.1t								
3	193	3	2500	10000	7.5	M_1:33000-60000	1	66	1.0	3	1-hyper	0	0			2		1-limit	2-modal	1	0.1t								
4	194	3	2500	10000	7.5	M_1:60000-300000	1	66	1.0	3	1-hyper	0	0			2		1-limit	2-modal	1	0.1t								
1	195	3	2500	10000	7.5	M_1:9000-12000	1	66	1.0	3	1-hyper	0	0			2		1-limit	2-modal	1	0.2t								
5	196	3	2500	10000	7.5	M_1:700000-3500000	1	66	1.0	3	1-hyper	0	0			2		1-limit	2-modal	1	0.2t								
2	197	3	2500	10000	7.5	M_1:12000-33000	1	66	1.0	3	1-hyper	0	0			2		1-limit	2-modal	1	0.2t								
3	198	3	2500	10000	7.5	M_1:33000-60000	1	66	1.0	3	1-hyper	0	0			2		1-limit	2-modal	1	0.2t								
4	199	3	2500	10000	7.5	M_1:60000-300000	1	66	1.0	3	1-hyper	0	0			2		1-limit	2-modal	1	0.2t								
	200	3	2500	10000	5	20000	1	66	1.0	3	1-hyper	0	0			2	M_1:1-7	0-entire	2-modal	1	0.5t								
	201	3	2500	10000	5	20000	1	66	1.0	3	2-cylinder	0	0			2	M_1:1-7	0-entire	2-modal	1	0.5t								
	202	3	2500	10000	5	20000	1	66	1.0	3	3-sph	0	0			2	M_1:1-7	0-entire	2-modal	1	0.5t								
1	205	3	2500	10000	5	M_1:9000-12000	1	66	1.0	3	1-hyper	0	0			2		1-limit	2-modal	1	0.1t								
5	206	3	2500	10000	5	M_1:700000-3500000	1	66	1.0	3	1-hyper	0	0			2		1-limit	2-modal	1	0.1t								
2	207	3	2500	10000	5	M_1:12000-33000	1	66	1.0	3	1-hyper	0	0			2		1-limit	2-modal	1	0.1t								
3	208	3	2500	10000	5	M_1:33000-60000	1	66	1.0	3	1-hyper	0	0			2		1-limit	2-modal	1	0.1t								
4	209	3	2500	10000	5	M_1:60000-300000	1	66	1.0	3	1-hyper	0	0			2		1-limit	2-modal	1	0.1t								
	210	2	2500	10000	10	20000	1	66	1.0	3	2-cylinder	1	0			2		0-entire	2-modal	1	M_1 0.1t-1.0t								
1	211	3	2500	10000	5	M_1:9000-12000	1	66	1.0	3	1-hyper	0	0			2		1-limit	2-modal	1	0.2t								
5	212	3	2500	10000	5	M_1:700000-3500000	1	66	1.0	3	1-hyper	0	0			2		1-limit	2-modal	1	0.2t								
2	213	3	2500	10000	5	M_1:12000-33000	1	66	1.0	3	1-hyper	0	0			2		1-limit	2-modal	1	0.2t								
3	214	3	2500	10000	5	M_1:33000-60000	1	66	1.0	3	1-hyper	0	0			2		1-limit	2-modal	1	0.2t								
4	215	3	2500	10000	5	M_1:60000-300000	1	66	1.0	3	1-hyper	0	0			2		1-limit	2-modal	1	0.2t								
1	216	3	5000	10000	5	M_1:6000-10000	1	90	1.0	3	1-hyper	0	0			2		1-limit	2-modal	1	0.1t								
5	217	3	5000	10000	5	M_1:700000-3500000	1	90	1.0	3	1-hyper	0	0			2		1-limit	2-modal	1	0.1t								
2	218	3	5000	10000	5	M_1:12000-33000	1	90	1.0	3	1-hyper	0	0			2		1-limit	2-modal	1	0.1t								
3	219	3	5000	10000	5	M_1:33000-60000	1	90	1.0	3	1-hyper	0	0			2		1-limit	2-modal	1	0.1t								
4	220	3	5000	10000	5	M_1:60000-300000	1	90	1.0	3	1-hyper	0	0			2		1-limit	2-modal	1	0.1t								
5	221	3	1500	10000	7.5	M_1:700000-3500000	1	66	1.0	3	1-hyper	0	0			2		1-limit	2-modal	1	0.1t								
3	222	3	1500	10000	7.5	M_1:33000-60000	1	66	1.0	3	1-hyper	0	0			2		1-limit	2-modal	1	0.1t								
4	223	3	1500	10000	7.5	M_1:60000-300000	1	66	1.0	3	1-hyper	0	0			2		1-limit	2-modal	1	0.1t								
	224	2	2500	10000	10	20000	1	66	1.0	3	2-cylinder	0	0			2		0-entire+plus	2-modal	1	M_1 0.1t-1.0t								
1	225	3	3000	10000	5	M_1:6000-10000	1	90	1.0	3	1-hyper	0	0			2		1-limit	2-modal	1	0.1t								
5	226	3	3000	10000	5	M_1:700000-3500000	1	90	1.0	3	1-hyper	0	0			2		1-limit	2-modal	1	0.1t								
2	227	3	3000	10000	5	M_1:12000-33000	1	90	1.0	3	1-hyper	0	0			2		1-limit	2-modal	1	0.1t								
3	228	3	3000	10000	5	M_1:33000-60000	1	90	1.0	3	1-hyper	0	0			2		1-limit	2-modal	1	0.1t								
4	229	3	3000	10000	5	M_1:60000-300000	1	90	1.0	3	1-hyper	0	0			2		1-limit	2-modal	1	0.1t								
1	230	3	4000	10000	5	M_1:6000-10000	1	90	1.0	3	1-hyper	0	0			2		1-limit	2-modal	1	0.1t								
5	231	3	4000	10000	5	M_1:700000-3500000	1	90	1.0	3	1-hyper	0	0			2		1-limit	2-modal	1	0.1t								
2	232	3	4000	10000	5	M_1:12000-33000	1	90	1.0	3	1-hyper	0	0			2		1-limit	2-modal	1	0.1t								
3	233	3	4000	10000	5	M_1:33000-60000	1	90	1.0	3	1-hyper	0	0			2		1-limit	2-modal	1	0.1t								
4	234	3	40000	10000	5	M_1:60000-300000	1	90	1.0	3	1-hyper	0	0			2		1-limit	2-modal	1	0.1t								
	235	3	2500	10000	7.5	M_1:12000-33000	1	66	1.0	3	1-hyper	0	0			2		1-limit	2-modal	191-3	0.1t								
	236	3	2500	10000	7.5	M_1:12000-33000	1	66	1.0	3	1-hyper	0	0			2		1-limit	2-modal	191-7	0.1t								
2	237	3	2500	10000	6	M_1:12000-33000	1	66	1.0	3	1-hyper	0	0			2		1-limit	2-modal	1	0.1t								
3	238	3	2500	10000	6	M_1:33000-60000	1	66	1.0	3	1-hyper	0	0			2		1-limit	2-modal	1	0.1t								
4	239	3	2500	10000	6	M_1:60000-300000	1	66	1.0	3	1-hyper	0	0			2		1-limit	2-modal	1	0.1t								
2	240	3	2500	10000	6	M_1:12000-33000	1	66	1.0	3	1-hyper	0	0			2		1-limit	2-modal	1	0.1t								
3	241	3	2500	10000	6	M_1:33000-60000	1	66	1.0	3	1-hyper	0	0			2		1-limit	2-modal	1	0.1t								
4	242	3	2500	10000	6	M_1:60000-300000	1	66	1.0	3	1-hyper	0	0			2		1-limit	2-modal	1	0.1t								
1	246	3	2500	10000	10	M_1:9000-12000	1	66	1.0	3	1-hyper	0	0			2		1-limit	2-modal	1	0.1t								
5	247	3	2500	10000	10	M_1:700000-3500000	1	66	1.0	3	1-hyper	0	0			2		1-limit	2-modal	1	0.1t								
2	248	3	2500	10000	10	M_1:12000-33000	1	66	1.0	3	1-hyper	0	0			2		1-limit	2-modal	1	0.1t								
3	249	3	2500	10000	10	M_1:33000-60000	1	66	1.0	3	1-hyper	0	0			2		1-limit	2-modal	1	0.1t								
4	250	3	2500	10000	10	M_1:60000-300000	1	66	1.0	3	1-hyper	0	0			2		1-limit	2-modal	1	0.1t								
1	251	3	2500	10000	10	M_1:9000-12000	1	66	1.0	3	1-hyper	0	0			2		1-limit	2-modal	1	0.2t								
5	252	3	2500	10000	10	M_1:700000-3500000	1	66	1.0	3	1-hyper	0	0			2		1-limit	2-modal	1	0.2t								
2	253	3	2500	10000	10	M_1:12000-33000	1	66	1.0	3	1-hyper	0	0			2		1-limit	2-modal	1	0.2t								
3	254	3	2500	10000	10	M_1:33000-60000	1	66	1.0	3	1-hyper	0	0			2		1-limit	2-modal	1	0.2t								
4	255	3	2500	10000	10	M_1:60000-300000	1	66	1.0	3	1-hyper	0	0			2		1-limit	2-modal	1	0.2t								

Tag	Lp_test	Geometry Parameter						Mesh		Num_eigen	Geometry shape		Pre-tension			Load		NLBA	Imperfection Type	Imperfection(Modal shape)		Imperfection(Reduction Factor)			Imperfection(Artificial)				
		rr=2-imp; rr=3-model	Rb(hori)	H	t0	Rk(vert)	a0-1edge control; 2-mid conrol	msize	r_ele	BUC_CONT	Hyp-1,Cyl-2, Sph-3	half-0; whole-1	ini_par; 1-on;0-off	s_ten(MPa)	ten_r	F-1;Disp-2; Pressure-3	Boundary: rs-1 top-tan;rs-2 top-rad;rs-3 both tan;rs4-both rad ;rs-5 fix	par_arcl; 1-limit;0-entire	2—modal; 5—Reduce; 6—artificial	num_imp_mod	max_peak	num_imp_mod	max_peak	mid_r	max_peak	w_h-w_r	par_art; 1-fixed; 2-range; 3-specified	eh-er	r_pi
1	256	3	2500	10000	5	M_1:9000-12000	1	66	1.0	3	1-hyper	0	0			2		1-limit	2-modal	1	0.1t								
5	257	3	2500	10000	5	M_1:700000-3500000	1	66	1.0	3	1-hyper	0	0			2		1-limit	2-modal	1	0.1t								
2	258	3	2500	10000	5	M_1:12000-33000	1	66	1.0	3	1-hyper	0	0			2		1-limit	2-modal	1	0.1t								
3	259	3	2500	10000	5	M_1:33000-60000	1	66	1.0	3	1-hyper	0	0			2		1-limit	2-modal	1	0.1t								
4	260	3	2500	10000	5	M_1:60000-300000	1	66	1.0	3	1-hyper	0	0			2		1-limit	2-modal	1	0.1t								
1	261	3	2500	10000	5	M_1:9000-12000	1	66	1.0	3	1-hyper	0	0			2		1-limit	2-modal	1	0.1t								
5	262	3	2500	10000	5	M_1:700000-3500000	1	66	1.0	3	1-hyper	0	0			2		1-limit	2-modal	1	0.1t								
2	263	3	2500	10000	5	M_1:12000-33000	1	66	1.0	3	1-hyper	0	0			2		1-limit	2-modal	1	0.1t								
3	264	3	2500	10000	5	M_1:33000-60000	1	66	1.0	3	1-hyper	0	0			2		1-limit	2-modal	1	0.1t								
4	265	3	2500	10000	5	M_1:60000-300000	1	66	1.0	3	1-hyper	0	0			2		1-limit	2-modal	1	0.1t								
2	266	3	2500	10000	5.5	M_1:12000-33000	1	66	1.0	3	1-hyper	0	0			2		1-limit	2-modal	1	0.1t								
3	267	3	2500	10000	5.5	M_1:33000-60000	1	66	1.0	3	1-hyper	0	0			2		1-limit	2-modal	1	0.1t								
4	268	3	2500	10000	5.5	M_1:60000-300000	1	66	1.0	3	1-hyper	0	0			2		1-limit	2-modal	1	0.1t								
2	269	3	2500	10000	4	M_1:12000-33000	1	66	1.0	3	1-hyper	0	0			2		1-limit	2-modal	1	0.1t								
3	270	3	2500	10000	4	M_1:33000-60000	1	66	1.0	3	1-hyper	0	0			2		1-limit	2-modal	1	0.1t								
4	271	3	2500	10000	4	M_1:60000-300000	1	66	1.0	3	1-hyper	0	0			2		1-limit	2-modal	1	0.1t								
2	272	3	2500	10000	12	M_1:12000-33000	1	66	1.0	3	1-hyper	0	0			2		1-limit	2-modal	1	0.1t								
3	273	3	2500	10000	12	M_1:33000-60000	1	66	1.0	3	1-hyper	0	0			2		1-limit	2-modal	1	0.1t								
4	274	3	2500	10000	12	M_1:60000-300000	1	66	1.0	3	1-hyper	0	0			2		1-limit	2-modal	1	0.1t								
	275	3	2500	10000	5	M_1:350000-700000infinite	1	66	1.0	3	1-hyper	0	0			2		1-limit	2-modal	1	0.1t								
5	276	3	2500	5000	5	M_1:700000-3500000	1	66	1.0	3	1-hyper	0	0			2		1-limit	2-modal	1	0.1t								
3	277	3	2500	7500	5	M_1:33000-60000	1	66	1.0	3	1-hyper	0	0			2		1-limit	2-modal	1	0.1t								
4	278	3	2500	12000	5	M_1:60000-300000	1	66	1.0	3	1-hyper	0	0			2		1-limit	2-modal	1	0.1t								
5	279	3	2500	5000	7.5	M_1:700000-3500000	1	66	1.0	3	1-hyper	0	0			2		1-limit	2-modal	1	0.1t								
3	280	3	2500	7500	7.5	M_1:33000-60000	1	66	1.0	3	1-hyper	0	0			2		1-limit	2-modal	1	0.1t								
4	281	3	2500	12000	7.5	M_1:60000-300000	1	66	1.0	3	1-hyper	0	0			2		1-limit	2-modal	1	0.1t								
5	282	3	2500	5000	10	M_1:700000-3500000	1	66	1.0	3	1-hyper	0	0			2		1-limit	2-modal	1	0.1t								
3	283	3	2500	7500	10	M_1:33000-60000	1	66	1.0	3	1-hyper	0	0			2		1-limit	2-modal	1	0.1t								
4	284	3	2500	12000	10	M_1:60000-300000	1	66	1.0	3	1-hyper	0	0			2		1-limit	2-modal	1	0.1t								
	285	2	2500	10000	5	20000	1	66	1.0	20	2-cylinder	0	0			2		0-entire	2-modal	M_1: 1-10	0.1t								
3	287	3	2500	7500+500*M_1	5	35000	1	66	1.0	3	1-hyper	0	0			2		1-limit	2-modal	1	0.1t								
3	288	3	2500	7500+500*M_1	7.5	35000	1	66	1.0	3	1-hyper	0	0			2		1-limit	2-modal	1	0.1t								
3	289	3	2500	7500+500*M_1	10	35000	1	66	1.0	3	1-hyper	0	0			2		1-limit	2-modal	1	0.1t								
	290	2	2500	10000	10	35000	1	66	1.0	1	1-hyper	0	0			2		1-limit	6-artificial						(0.1+0.05*M_1)*t	20-4(1st modal= -)	1		
	291	2	2500	10000	10	35000	1	66	1.0	1	1-hyper	0	0			2		1-limit	2-modal	1	(0.1+0.05*M_1)*t								
	292	2	2500	10000	10	35000	1	66	1.0	1	1-hyper	0	0			2		1-limit	2-modal	2	(0.1+0.05*M_1)*t								
	293	2	2500	10000	10	35000	1	66	1.0	1	1-hyper	0	0			2		1-limit	6-artificial						(0.1+0.05*M_1)*t	14- – 20			
	294	2	2500	10000	10	35000	1	120	1.0	1	1-hyper	0	0			2		1-limit	6-artificial						(0.1+0.05*M_1)*t	7- – 20			
	295	2	2500	10000	10	35000	1	66	1.0	1	1-hyper	0	0			2		1-limit	2-modal	M_1	0.2								